INFORMATION TO USERS

This manuscript has been reproduced from the microfilm master. UMI films the text directly from the original or copy submitted. Thus, some thesis and dissertation copies are in typewriter face, while others may be from any type of computer printer.

The quality of this reproduction is dependent upon the quality of the copy submitted. Broken or indistinct print, colored or poor quality illustrations and photographs, print bleedthrough, substandard margins, and improper alignment can adversely affect reproduction.

In the unlikely event that the author did not send UMI a complete manuscript and there are missing pages, these will be noted. Also, if unauthorized copyright material had to be removed, a note will indicate the deletion.

Oversize materials (e.g., maps, drawings, charts) are reproduced by sectioning the original, beginning at the upper left-hand corner and continuing from left to right in equal sections with small overlaps. Each original is also photographed in one exposure and is included in reduced form at the back of the book.

Photographs included in the original manuscript have been reproduced xerographically in this copy. Higher quality 6" x 9" black and white photographic prints are available for any photographs or illustrations appearing in this copy for an additional charge. Contact UMI directly to order.

UMI

A Bell & Howell Information Company
300 North Zeeb Road, Ann Arbor, MI 48106-1346 USA

NOTE TO USERS

The original manuscript received by UMI contains pages with slanted print. Pages were microfilmed as received.

This reproduction is the best copy available

UMI

Université d'Ottawa · University of Ottawa

ZERO-DIMENSIONAL PROPERTIES OF SELF-ASSEMBLED ISLANDS

© Par Sylvain Raymond

Thèse soumise à l'école des études supérieures
et de la recherche en vue de l'obtention du
diplôme de doctorat en physique.

Département de physique
Faculté des sciences
Université d'Ottawa
Ottawa, Canada
Juin 1997

National Library of Canada

Acquisitions and Bibliographic Services

395 Wellington Street
Ottawa ON K1A 0N4
Canada

Bibliothèque nationale du Canada

Acquisitions et services bibliographiques

395, rue Wellington
Ottawa ON K1A 0N4
Canada

Your file Votre référence

Our file Notre référence

The author has granted a non-exclusive licence allowing the National Library of Canada to reproduce, loan, distribute or sell copies of this thesis in microform, paper or electronic formats.

L'auteur a accordé une licence non exclusive permettant à la Bibliothèque nationale du Canada de reproduire, prêter, distribuer ou vendre des copies de cette thèse sous la forme de microfiche/film, de reproduction sur papier ou sur format électronique.

The author retains ownership of the copyright in this thesis. Neither the thesis nor substantial extracts from it may be printed or otherwise reproduced without the author's permission.

L'auteur conserve la propriété du droit d'auteur qui protège cette thèse. Ni la thèse ni des extraits substantiels de celle-ci ne doivent être imprimés ou autrement reproduits sans son autorisation.

0-612-28370-4

À Claudine, ma soeur, qui avance courageusement dans la vie.

J'espère que tu vas arriver à bon port.

Abstract

The steady state and dynamic properties of semiconductor self-assembled island structures made from III-V materials are studied by photoluminescence and time-resolved photoluminescence. The islands layer contains a number of hemispherical caps with a low-gap material inside the cap and a high-gap material outside. The experiments performed are aimed at probing the nature of the bound states inside the islands, looking specifically at the dimensionality of these islands through the mapping of the density of states.

First, a system consisting of an $Al_{0.45}In_{0.55}As$ layer imbedded in an $Al_{0.35}Ga_{0.65}As$ matrix emitting in the visible (red) is used to directly probe the properties of "individual" islands and compare them with different systems: two-dimensional (quantum well), one-dimensional (quantum wire) and zero-dimensional (quantum dot). The observed temperature independent linewidth and lifetimes are attributed to quantum dot properties. Next, the strong emission obtained under resonant excitation conditions in this system is used to study the influence of phonons on the relaxation processes in zero-dimensional semiconductor heterostructure systems.

The other material system studied consists of a single $In_{0.5}Ga_{0.5}As$ self-assembled layer imbedded in GaAs emitting in the infra-red. A model based on a quantum well with in-plane parabolic confinement is developed and compared with experimental results. Magneto-photoluminescence measurements reveal the symmetry of the electronic shell structure which is found to be consistent with the model developed, thus confirming the

zero-dimensional nature of the carrier confinement. The presence of excited states is then exploited by studying the inter-sublevel dynamics of carriers in quantum dots. Despite the discreteness of the density of states, fast inter-sublevel dynamics is observed and all experimental observations are found to be consistent with state-filling dynamics for which the inter-sublevel relaxation is impeded only when lower energy levels are filled.

Sommaire

Des îlots semiconducteurs fabriqués à partir de matériaux de la famille des III-V sont étudiés à l'aide de mesures de photoluminescence et de photoluminescence résolue dans le temps. La couche d'îlots contient des d'hémisphères tronqués composés d'un matériel de faible gap à l'intérieur entouré d'un matériel à haut gap à l'extérieur. Les expériences visent à sonder la nature des états liés dans les îlots et en particulier à mettre en évidence la dimensionalité de leur densité d'états.

Dans un premier temps, un échantillon composé d'une couche d' $Al_{0.45}In_{0.55}As$ inscrite dans une barrière d'$Al_{0.35}Ga_{0.65}As$ est utilisé afin d'avoir accès aux propriétés d'îlots "individuels". Les largeurs de raie et les temps de vie indépendants de la température sont associés à des systèmes de boîtes quantiques. La forte luminescence obtenue lorsqu'on excite l'échantillon de façon résonante nous permet d'étudier l'influence des phonons sur la dynamique des porteurs pour des hétérostructures semiconductrices en zéro dimensions.

Dans un deuxième temps, un système composé d'une couche d' $In_{0.5}Ga_{0.5}As$ incorporée dans une matrice de GaAs émettant dans l'infra-rouge est étudiée. Un modèle simple basé sur un puits quantique avec un potentiel parabolique dans le plan est élaboré et les prédictions de ce modèle sont comparées avec les résultats expérimentaux. Notamment, des mesures de magnéto-photoluminescence mettent en évidence la symétrie des états électroniques, et les prédictions du modèle sont vérifiées ce qui confirme la

nature zéro-dimensionnelle des états liés. La présence d'états excités est aussi exploitée pour discuter de la dynamique des porteurs en zéro dimensions. On observe une relaxation très efficace des porteurs des niveaux supérieurs vers les niveaux inférieurs. De plus, l'ensemble des résultats expérimentaux s'explique facilement en terme d'une dynamique dominée par le remplissage des états, avec des temps de transfert inter-niveaux restreints seulement par le principe d'exclusion de Pauli.

Statement of Originality

The experimental results presented in this thesis were obtained by the author himself, alone or through his collaborations during the period of his Ph. D. research project, except when otherwise stated. For example, the TEM micrographs of the samples studied in this thesis were produced by Dr. Rosa Leon, and the photoluminescence spectra of fig. IV-5a and fig. IV-1 were measured by Dr. Simon Fafard. The samples were grown at the University of California at Santa-Barbara by Dr. Rosa Leon and Dr. Devin Leonard. All other experimental results are original. This includes in particular:

1. The micro-photoluminescence of self-assembled dots as a function of temperature and excitation intensity.
2. The temperature-dependent lifetime obtained from a single ultra-narrow line in the micro-photoluminescence spectrum of self-asssembled dots.
3. Time resolved measurements obtained on the phonon resonances in the macro-photoluminescence spectrum of self-assembled dots.
4. Excitation dependent macro-photoluminescence spectrum of InGaAs/GaAs self-assembled dots.
5. Lifetime of carriers trapped in self-assembled excited bound states.
6. Photoluminescence of self-assembled islands as a function of increasing magnetic field.

The theoretical calculation representing a prediction of the different emission intensities for the bound states in a quantum dot (section V.2.3) is also an original contribution of the author. All other calculations are based on very similar work previously published by other authors.

Finally, publications 2, 5, 6, 7 and 8 in the list presented on page ix were written by the author of this thesis.

Publications

The following articles were published during the course of this work.

I Directly Related to thesis

I) Articles

1) S. Raymond, P. Hawrylak, C. Gould, S. Fafard, A. Sachrajda, M. Potemski, A. Wojs, S. Charbonneau, D. Leonard, P.M. Petroff and J.L. Merz "Exciton droplets in zero dimensional system in a magnetic field". Solid State Comm., vol. 101, p. 883 (1997).

2) S. Raymond, P. J. Poole, S. Fafard, A. Wojs, Pawel Hawrylak, S. Charbonneau, D. Leonard, P.M. Petroff and J.L. Merz "State filling and time-resolved photoluminescence of excited states in InGaAs/GaAs self-assembled quantum dots. Phys. Rev. B. **54**, 11548 (1996).

3) S. Raymond, S. Fafard, P. J. Poole, C. Gould, A. Wojs, Pawel Hawrylak, M. Potemski, A. Sachrajda, S. Charbonneau, D. Leonard, P.M. Petroff and J.L. Merz "State-filling and magneto-photoluminescence of excited states in InGaAs/GaAs self-assembled quantum dots", Superlatt. Microstruct. vol. 21, No 4, p. 541 (1997).

4) S. Fafard, S. Raymond, P. J. Poole, Y. Feng, J. McCaffrey and S. Charbonneau, "Optical studies of III-V self-assembled semiconductor quantum dots", Physics in Canada Vol. 52 No. 5 267-274 (september-october 1996).

5) S. Raymond, S. Fafard, S. Charbonneau, D. Leonard, P.M. Petroff and J.L. Merz "Photocarrier recombination in AlInAs/AlGaAs self-assembled quantum dots", Phys. Rev. B 52,17238 (1995).

6) S. Raymond, S. Fafard and S. Charbonneau "Temperature dependence of ultra-sharp luminescence lines in AlInAs/AlGaAs self-assembled Quantum dots", Can. J. of Phys. vol. 74, No 1, p. s216 (1996).

7) S. Raymond, S. Fafard, Y. Feng and S. Charbonneau "Luminescence of biased AlInAs/AlGaAs self-assembled quantum dots", published in the proceedings of the XXIIIrd

international conference on the physics of semiconductors. (ICPS XXIII, Berlin, Germany).

II) Other contributions

8) S. Raymond, P. J. Poole, S. Fafard, A. Wojs, P. Hawrylak, S. Charbonneau, D. Leonard, P.M. Petroff and J.L. Merz "Time resolved photoluminescence of excited states in InGaAs/GaAs self-assembled quantum dots", Ninth international conference on Superlattices, Microstructures and Microdevices", ICSMM-9, (14-19 july 1996, Liège, Belgium).

9) S. Raymond, P. J. Poole, S. Fafard, A. Wojs, P. Hawrylak, S. Charbonneau, D. Leonard, P.M. Petroff and J.L. Merz "State-filling and time-resolved photoluminescence of excited states in InGaAs/GaAs self-assembled dots", annual meeting of the Canadian association of physicists 1996, (16-19 juin 1996), Ottawa University.

10) S. Raymond, P. J. Poole, S. Fafard, A. Wojs, P. Hawrylak, S. Charbonneau, D. Leonard, P.M. Petroff and J.L. Merz "Time-resolved photoluminescence of excited states in InGaAs/GaAs self-assembled dots", ECAMI Workshop, june12-14 1996, National Reaserch council of Canada, Ottawa, Canada.

II Contributions not directly related to thesis

11) S. Fafard, S. Raymond, S. Charbonneau, R. Leon, D. Leonard, P.M. Petroff and J.L. Merz "Temperature effects on the radiative recombination in self-assembled quantum dots", Surface Science 361/362 778-782 (1996).

12) S. Fafard, K. Hinzer, S. Raymond, M. Dion, Y. Feng, and S. Charbonneau"Red-emitting semiconductor quantum dot lasers", Science Vol. 274, pp 1350-1353.

13) S. Fafard, Z. Wazilewski, J. Mcaffrey, S. Raymond and S. Charbonneau "InAs self-assembled quantum dots grown by molecular beam epitaxy", Appl. Phys. Lett. 68 (7), 991 (1996).

REMERCIEMENTS
ACKNOWLEDGEMENTS

Apprendre est avant tout une expérience humaine. Dans une période où l'atmosphère dans les départements de physique est souvent morose, tout spécialement pour les étudiants qui se demandent constamment si leurs efforts et leurs nuits blanches vont leur permettre de se trouver du travail en bout de ligne, j'ai eu deux chances extraordinaires: Dr. Sylvain Charbonneau, mon superviseur, et Dr. Simon Fafard, notre proche collaborateur et pratiquement mon "assistant" superviseur. L'héritage le plus important qu'un superviseur laisse à ses étudiants, c'est l'enthousiasme. Sans cet aspect, le superviseur le plus connaissant est un poids mort. Sylvain, merci mille fois pour l'énergie débordante, la disponibilité, les échanges, le leaderdship et surtout, surtout ton extraordinaire partialité, si rare chez un scientifique de haut niveau, toujours en faveur de tes étudiants et prêt à monter aux barricades pour eux. Pour moi, mon stage avec toi a été extraordinaire. Si je pars pour un ailleurs, c'est dans l'esprit d'un jeune qui quitte la maison à regret parce qu'il doit trouver sa propre voie.

Simon, merci à toi aussi pour ton extraordinaire enthousiasme qui n'a rien à envier à celui de Sylvain. Il est rare qu'un étudiants puisse se retrouver dans un laboratoire dépassé minuit avec un de ses "superviseurs". Mais le plus extraordinaire pour un étudiant qui veut apprendre, c'est cette patience à s'asseoir et à discuter des heures durant des problèmes

les plus compliqués. Cependant, à bien y penser ce que j'ai apprécié le plus c'est cette faculté de rire quand un étudiant arrive avec une question sur un sujet qu'il devrait déjà bien connaître. Le droit à l'ignorance, c'est extraordinaire!

I would like to say special thanks to Dr. Rosa Leon and Dr. Devin Leonard for the growth of good samples. Thanks also to Pr. James L. Merz and Pr. Pierre Petroff for their kind collaboration with our group.

I would also like to thank Dr. Philip Poole for contributing greatly to my experimental education. Thanks for always being ready to put your hands in my problems!

Merci à Paul Piva, pour qui j'ai développé au fil du temps un profond respect tant du point de vue professionnel que du point de vue humain. Nos échanges on certainement contribué à rendre la science plus humaine, plus intéressante et plus enrichissante.

Thanks to Dr. Pawel Hawrylak and to Dr. Arkadiusz Wojs for putting this strong Polish spirit at work and provide the theoretical support necessary for this study. My conception of self-assembled dots has been greatly influenced, and improved, by our collaboration.

The support of Dr. Yan Feng for sample processing was greatly appreciated as the timescales were often short.

I would also like to thank Peter Zawadzki, Don Brown, Piet Van Der Meer and Mike Shahine for their outstanding technical support. Is there any technical problem you guys could not solve?

A wealth of other scientists at NRC have contributed to my education: Dr. Andy Sachrajda, Dr. Peter Coleridge and all the others with whom I had discussions. Thank you.

Finalement, merci aux secrétaires du département de physique, Madeleine, Jacinthe, Lorraine et Hélène qui ont toujours jeté un rayon de soleil sur mes visites irrégulières à l'Université d'Ottawa.

Table of Contents

Abstract		iii
Sommaire		v
Statement of Originality		vii
List of Publications		ix
Acknowledgements/remerciements		xi
Table of contents		xiv
List of Figures		xvi
List of Tables		xix
List of Abbreviations		xx
Chapter I	Introduction	1
Chapter II	Theory	13
	II.1 Density of states for idealized structures	14
	II.2 Energy Levels of a Lens Shaped Quantum Dot	24
	II.3 Spectrum of a Parabolic Dot in a Strong Magnetic Field	33
	II.4 Selection Rules for Electron Transitions	35
	II.4.1 Band-to-band Transitions	36
	II.4.2 Excitonic Transitions	41
	II.5 Finite Potential Barriers and Related Effects	44
	II.6 Concluding remarks	47
Chapter III	Experimental Methods	50
	III.1 Photoluminescence	50
	III.2 Imaging tube set-up and Time-Correlated Single Photon Counting	55
	III.3 Up-Conversion	58
	III.4 Rate Equation Model	63
	III.5 Summary	65
Chapter IV	Properties of AlInAs/AlGaAs self-assembled Islands	67
	IV.1 Intrinsic Linewidth and Related Properties	67
	IV.2 Carrier Dynamics: influence of phonons	76

Chapter V Excited State Dynamics: Properties of InGaAs/GaAs self-assembled Islands 88
V.1 Single Dot modeling 89
V.1.1 Conduction Band 92
V.1.2 Valence Band 97
V.2 Steady State Photoluminescence 102
V.2.1 CW Excitation 102
V.2.2 Pulsed Excitation 113
V.2.3 Modeling of the PL results: State-Filling 118
V.3 Time-Resolved Photoluminescence 130
V.4 Magneto-Photoluminescence 137
V.5 Concluding remarks 145

Chapter VI Conclusion 146

References 152

List of Figures

Figure | Page

Figure		Page
I-1	Epitaxial growth modes	4
I-2	Dark field TEM picture of sample VI (AlInAs/AlGaAs) system	7
I-3	Ta mask technique for InGaAs island growth	9
I-4	Dark field TEM picture of sample IR (InGaAs/GaAs) system	10
I-5	Layer structure of sample VI and IR	12
II-1	Evolution of the allowed states in k-space as the dimensions of a structure is changed.	16
II-2	Planes of allowed states in k-space for a quantum well	20
II-3	Density of states for different dimensionalities	21
II-4	Comparison of conduction band DOS for a 0D and a 2D layer	23
II-5	Cross section of a hemispherical lens showing the relationship between the relevant quantities for theoretical modeling	25
II-6	Change in confinement energy as the interstitial layer changes from a thin uniform layer to a lens-shaped dot	27
II-7	Phonon dispersion relationship in a periodic one-dimensional lattice	39
II-8	Illustration of electron transitions in a) a two-dimensional structure and b) a zero-dimensional structure	41
II-9	Dispersion relationship for excitonic states	42
II-10	Band profile for a well with finite barriers	45
III-1	Standard modern photoluminescence set-up. a) representation of all the components b) and c) show the sample reaction to laser excitation for a "bulk" and a quantum dot structure respectively	51
III-2	Example of photoluminescence spectrum from a self-assembled island sample	54

III-3 Set-up for time-correlated single photon counting (time-resolved PL) and steady state photoluminescence with an imaging tube 57

III-4 Set-up for up-conversion experiments and steady state photoluminescence with the CCD array and the Germanium detector 60

III-5 Example of up-converted spectrum for a given time delay 62

III-6 Example of carrier dynamics for a quantum well 64

IV-1 Macro-PL spectrum of sample VI 68

IV-2 Micro-PL spectra of sample VI showing the evolution of "single dot" linewidths as a function of temperature 70

IV-3 Comparison of "single dot" linewidths obtained for self-assembled islands with predictions for quantum well states 73

IV-4 Evolution of the radiative lifetime of a "single dot" as a function of temperature 75

IV-5 Comparison of time-decay spectrum obtained for the case of resonant excitation exactly one phonon above the detection energy, with the time-decay spectrum obtained for non-resonant excitation 77

IV-6 Representation of relaxation processes in self-assembled quantum dots 80

IV-7 Summary of the rise times and decay times obtained for the different excitation conditions 82

IV-8 Evolution of the ultranarrow emission line spectrum as a function of excitation intensity 84

V-1 Three dimensional representation of the typical semiconductor island modeled using the adiabatic approximation for sample IR. 90

V-2 Cross section of the idealized quantum dot as defined by Figure V-2 94

V-3 Evolution of the lateral effective confining potential for the conduction band states of sample IR 95

V-4 Evolution of the lateral effective confining potential for the valence band states of sample IR 99

V-5 Evolution of the emission spectrum as a function of excitation power density for a CW laser source 103

V-6 Illustration of the different types of layers that could give rise to higher energy emission lines in sample IR 105

V-7 Integrated radiated output intensity as a function of excitation intensity under CW excitation 109

V-8 Evolution of the emission spectrum of sample IR as a function of temperature 112

V-9 Evolution of the emission spectrum as a function of excitation power density for a pulsed laser source 115

V-10 Integrated radiated output intensity as a function of excitation intensity under pulsed excitation 116

V-11 Schematics of an InGaAs quantum dot filled with 9 electron-hole and related dynamics 120

V-12 Calculated emission intensities for the transition lines observed in sample IR as a function of average carrier population for a) steady state excitation and b) pulsed excitation 127

V-13 Measured emission intensities for the transition lines observed in sample IR as a function of average carrier population for a) steady state excitation and b) pulsed excitation 128

V-14 Time decay spectrum of the various transition lines in sample IR 131

V-15 Summary of the decay times obtained as a function of excitation power density for different transition index 132

V-16 Evolution of the bound state energies in the Faraday configuration as a function of magnetic field in sample IR 138

V-17 Evolution of the energy of the lowest radiative transitions as a function of magnetic field 140

V-18 Set-up for magneto-photoluminescence measurements 142

V-19 Evolution of the emission spectrum of sample IR as a function of magnetic field 143

List of Tables

Table	Page

II-1 Extension of the wavefunction away from the center of the lens-shape dot for the lower energy levels 30

V-1 Parameters used for modeling the conduction band states of sample IR 92
V-2 Parameters used for modeling the valence band states of sample IR 98

V-3 Transition energies in sample IR obtained from luminescence peak positions 104

V-4 Evolution of the carrier population created in the strained InGaAs layer as a function of excitation power density for CW excitation; comparison with the number of available states in a quantum well and a quantum dot layer 107

V-5 Optical parameters used to evaluate the absorption in sample IR under CW excitation 108

V-6 Optical parameters used to evaluate the absorption in sample IR under pulsed excitation 114

V-7 Evolution of the carrier population created in the strained InGaAs layer as a function of excitation power density for pulsed excitation; comparison with the number of available states in a quantum well and a quantum dot layer 117

List of Abbreviations

APD	Avalanche photodiode
CW	Continuous wave (steady state)
CWPL	Steady state photoluminescence
DOS	Density of states
FWHM	Full width at half maximum
IPMT	Imaging photomultiplier tube
LA	Longitudinal acoustic (phonon)
LO	Longitudinal optical (phonon)
MBE	Molecular beam epitaxy
PL	Photoluminescence
QD	Quantum Dot
QW	Quantum Well
QWR	Quantum Wire
TA	Transverse acoustic (phonon)
TAC	Time-to-amplitude converter
TO	Transverse optical (phonon)
TRPL	Time-resolved photoluminescence
WL	Wetting layer
0D	Zero dimensional
1D	One dimensional
2D	Two dimensional
3D	Three dimensional

I INTRODUCTION

The concept of quantum confined heterostructures, based on semiconductor materials, was introduced in the early 70's and was triggered primarily by the rapid improvement of growth techniques. The last three decades have seen a large amount of effort spent in understanding the fundamental properties of these lower dimensional systems and in predicting their use in active components.

The first such structures fabricated and studied were the quantum well and the superlattice, the former made of a single layer of low gap semiconductor sandwiched by a higher bandgap material while the latter is composed of a succession of such layers in which carriers in one layer could interact with the ones in adjacent layers. One of the first predictions related to quantum confinement, made by Esaki and Tsu[1], was the tunneling of carriers through thin barriers, producing negative differential regions in the I-V characteristics of these structures. This phenomenon was experimentally confirmed by Chang[2] in GaAs/AlGaAs double-barrier resonant tunneling structures, and by several other groups for a wide variety of material systems[3].

To this day however, the most important industrial application of semiconductor heterostructures remains the semiconductor quantum well laser. At first made of a simple p-n junction[4], it was found that the characteristics of the lasers could be improved by inserting a quantum well in the center of the p-n junction[5]. Expected improvements in the threshold current[6] and temperature stability[7] brought further motivation to study structures

having even lower dimensionality such as quantum wires (QWR), where carriers are confined in one-dimensional states, and quantum dots (QD) where carriers are confined in zero-dimensional states. On a practical level, the fabrication of such structures remain an interesting challenge.

Over the last decade, a number of techniques have been developed and tested for the production of QWRs and QDs. For example, quantum wires have been fabricated using wet or dry etching of quantum well samples[8], intermixing[9], growth over patterned substrates[10], transverse overgrowth of a cleaved Multiple Quantum Well sample[11] and field induced carrier concentration modulation[12]. Similarly, quantum dots have been fabricated using wet/dry etching[13], intermixing[14], gate modulation[15], glass matrix[16] and overgrowth on vicinal surfaces[17]. The main criteria in assessing the quality of these structures include: the number of defects, such as dislocations and vacancies which act as non-radiative recombination centers, the good uniformity of the wires/dots across the sample and the amount of confinement for the carriers. Techniques involving etching often create structures with a large number of defects, while intermixing and gate modulation structures provide low confinements. Growth on patterned substrates involves complex fabrication. Finally, small semiconductor drops imbedded in a glass matrix are not well suited for applications (i.e. electrical injection of carriers in the dots is difficult to achieve). Although some of the systems described above show very interesting characteristics, they all possess some drawbacks from a practical and technical point of view.

It is certainly possible to improve the above systems, but the approach adopted for this study involves a recently implemented fabrication technique, namely Stranski-

Krastanow growth, used to produce a new type of layer referred to as self-assembled islands. The different possible regimes of epitaxial growth were identified a long time ago[18,19,20] by several groups, but it was not until recently that technology allowed their implementation. Numbering three in total, these growth modes have been named Volmer-Weber, Stranski-Krastanow and Frank-Van Der Merve respectively and the corresponding types of layer obtained are shown in Figure I-1. For a given high bandgap/low bandgap material system used, the growth mode can be predicted if one knows the interface energy between the two materials, as well as the strain and surface energy of the low gap material layer. The interface energy represents the cost to form an interface between two given materials, the strain energy is important if the system is lattice mismatched, and the surface energy represents the cost to form a surface of a specific shape for a given layer. The first case considered is Volmer-Weber growth; in this case, the interface energy cost is very high and during the growth, the adatoms will have a tendency to form islands on the surface to minimize the interface area, as shown in Figure I-1a. If the interfacial energy is not important, the atoms "wet" the entire surface for at least a few monolayers. At this point, if the materials are lattice-matched such that there is no strain in the system, this process goes on and one obtains the usual layer by layer (or Frank-Van Der Merve) growth, as shown in Figure I-1c. If the system is lattice-mismatched, the strain energy can be minimized by forming coherent islands on top of the "wetting layer" (WL); this occurs spontaneously, hence the terminology "self-assembled islands". This epitaxial regime is referred to as Stranski-Krastanow growth (Figure I-1b) and is observed if the strain energy reduction offsets the cost of forming a non-planar surface[21]. If the growth is

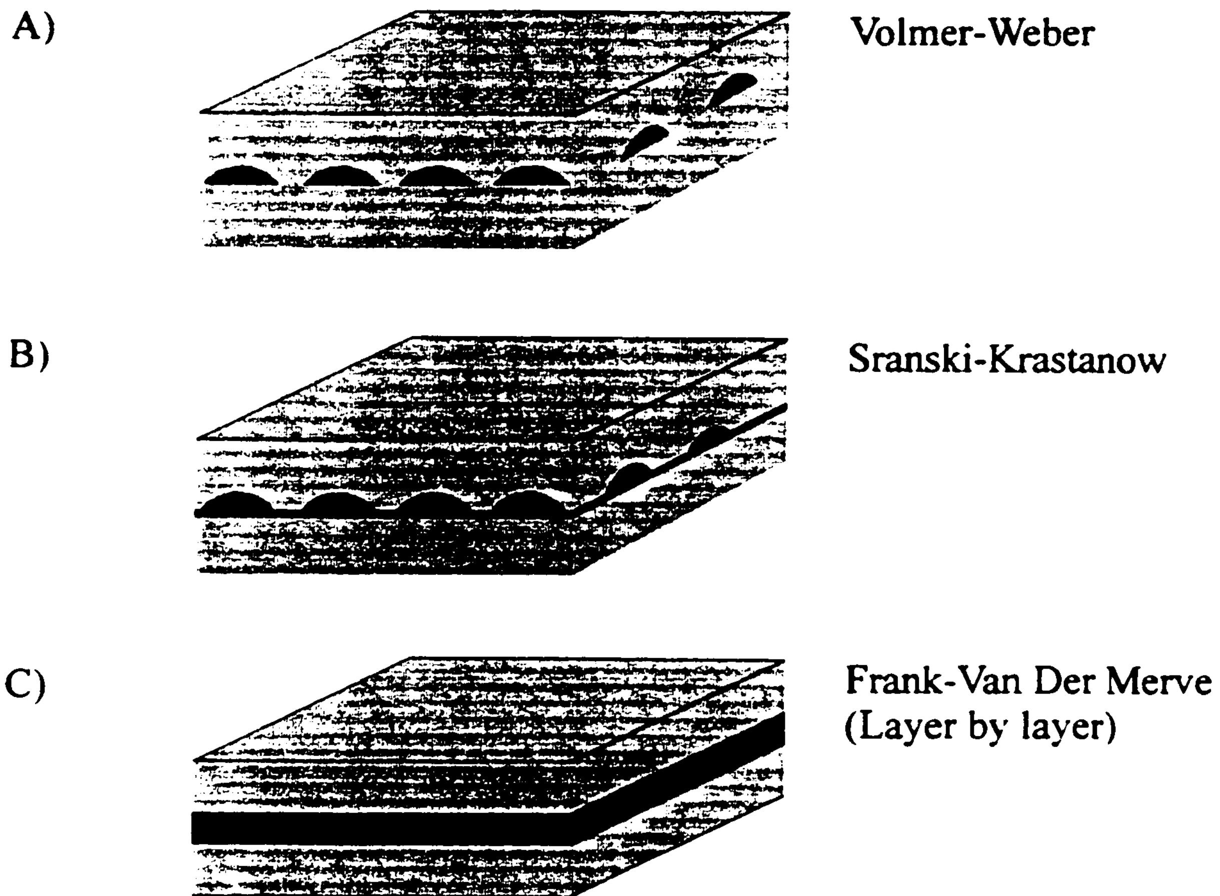

Figure I-1
Illustration of the different epitaxial growth modes.

allowed to proceed beyond the initial island formation, misfits and dislocations start forming which is undesirable for the optical quality of the sample.

Early studies involving self-assembled islands were actually done in the perspective of growing high-quality quantum wells, in order to avoid island and dislocation formation[22]. One of the first clear proofs of defect free island formation in the Stranski-Krastanow growth mode was reported by Eaglesham and Cerullo[23] for SiGe islands on Si. Shortly after, island formation was observed in III-V materials by several groups[24,25,26] and

strong luminescence was unambiguously shown to originate from the islands themselves[27]. At the onset of this work, it was hoped that this growth method would provide a reliable in-situ fabrication technique for a class of systems combining the advantages of zero-dimensional properties with the strong luminescence of III-V materials. However, it remains to be proven that the islands have good zero-dimensional properties.

In the present work, two complementary types of self-assembled systems are studied. The first system is composed of a lower bandgap AlInAs island layer imbedded in AlGaAs barrier material. The optically active layer emits in the visible (red) and for this reason this sample will be referred to as sample VI. The fabrication was performed using MBE growth on a semi-insulating GaAs substrate[27]. Temperatures were determined with a calibrated pyrometer. An As_4 partial pressure of 9×10^{-6} torr was maintained throughout the growth. After oxide desorption, a GaAs undoped buffer layer of 0.5 μm was grown at 600°C. The 200 nm $Al_{0.35}Ga_{0.65}As$ cladding layer was then grown at 650°C. The sample was then cooled to 530°C, and In and Al molecular beams were pulsed in short cycles at low growth rates, resulting in the deposition of small amounts of $Al_{0.45}In_{0.55}As$ (<<0,1 monolayers per cycle). This was done until the transition from 2D growth to 3D growth was observed in the reflected high-energy electron diffraction (RHEED) pattern. The Al and Ga shutters were then opened, and growth was continued in order to cover the strained islands with a 30 nm $Al_{0.35}Ga_{0.65}As$ barrier layer, while the temperature was ramped back to 650°C. A 10 nm GaAs cap layer was finally grown to protect the $Al_{0.35}Ga_{0.65}As$ barrier from oxidation.

Structural characterization of this sample was obtained via plan view and cross-

section TEM pictures presented in Figure I-2 a) and c) respectively. Both pictures clearly show that a self-assembled layer has been obtained with islands of similar sizes randomly distributed on the surface. The cross-section reveals the existence of a thin (2.1nm) quantum well layer (the wetting layer), connecting an array of thicker (3.2 nm) lens-shaped discs. From a careful inspection of the plan view TEM, one can obtain statistics on the size distribution of the island base diameter, and the results are summarized in Figure I-2b. the average base diameter of the islands is found to be 18±2 nm with an areal density of 200 μm^{-2}. It is very important to note that both TEM pictures reveal no dislocations or defects of any kind in the island layer thus indicating that high quality structures have been obtained.

The second system studied is composed of a lower bandgap InGaAs island layer imbedded in GaAs barrier material, and the active layer emits in the infra-red so that this sample will be referred to as sample IR. The growth was performed by molecular beam epitaxy in the Stranski-Krastanow growth mode on a nominally undoped GaAs substrate[28]. The sample has been grown to obtain a range of InGaAs coverage across the sample surface using a shadow mask technique described as follows[29]. A bondless 2 in. full wafer holder was equipped with a Ta mask capable of covering the entire wafer. This shadow mask was 4 mm from the wafer surface and pivoted from a point near the wafer edge. The GaAs buffer layer, the $In_{0.17}Ga_{0.83}As$ quantum well and the GaAs barrier were grown while the wafer was unmasked. Then, the strained $In_{0.5}Ga_{0.5}As$ layer deposition was performed in 4 different segments. During each segment, the InGaAs material was grown using cycles of 0.05 nm deposition followed by a 5 sec As_2 pause. During the first segment

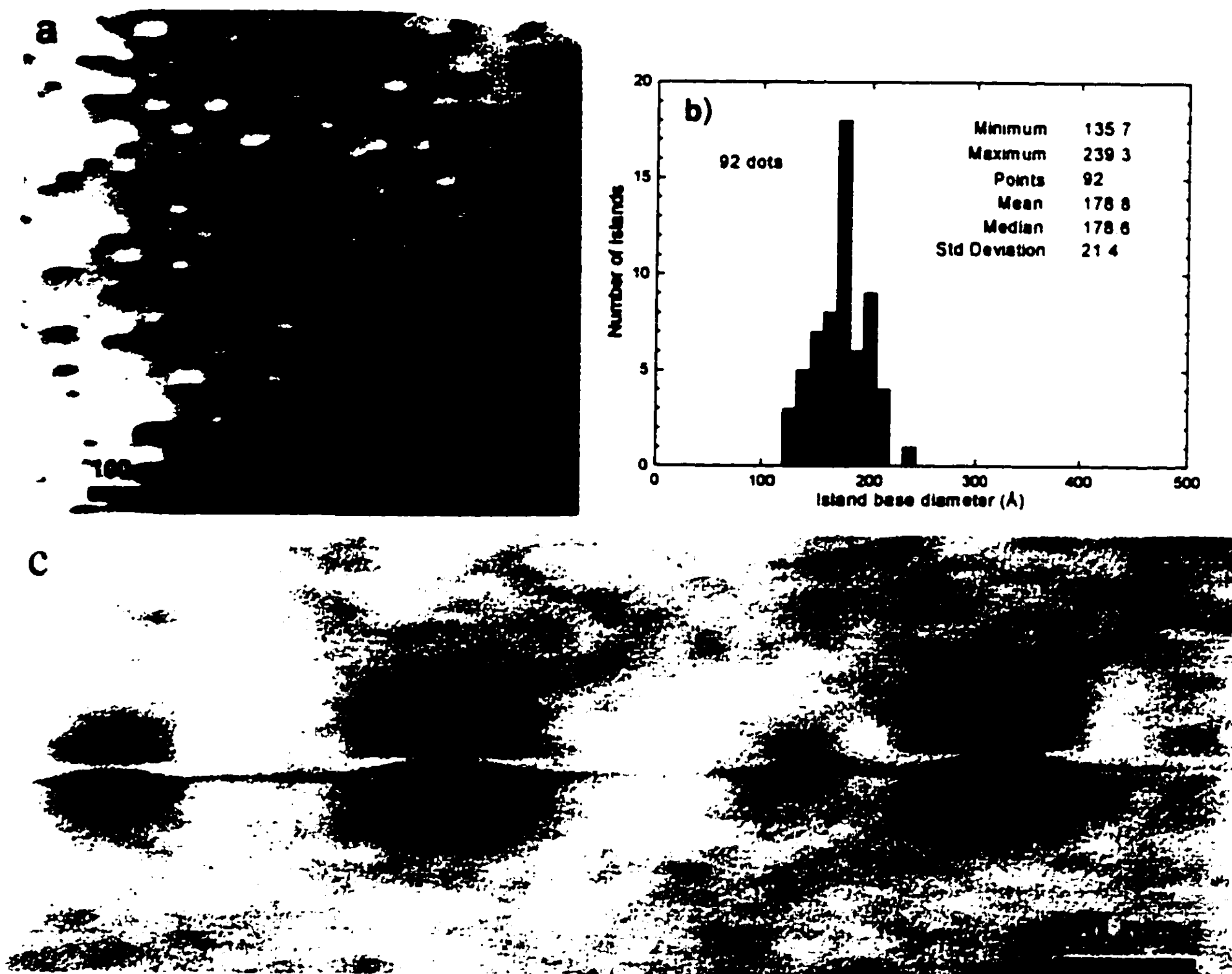

Figure I-2

Dark field TEM pictures of sample VI revealing strain contrast around the island layer. a) Plan view TEM showing the position and lateral size of the islands in the plane of the wetting layer. b) Statistics on size and areal density that can be extracted from the plan-view TEM. c) Cross-section TEM of the same sample clearly showing the thin wetting layer connecting lens-shaped islands[27]. Courtesy of Dr. Rosa Leon.

the wafer was unmasked and a total of 3.5 monolayers of InGaAs material was deposited on its entire surface. The flat edge of the mask was then rotated 60° to cover part of the wafer and an additional monolayer was grown. The mask was rotated an additional 25° and one extra monolayer of material was grown. Finally, the mask was again rotated by 20° before a final monolayer of InGaAs was grown. As a result, four different regions with InGaAs coverage ranging from 3.5 to 6.5 monolayers are obtained as shown in Figure I-3. After the island layer growth, the mask was removed from the surface and the cap layer was grown. In more detail, the growth parameters are described as follows: The As_2 pressure was kept at $9x10^{-6}$ torr throughout the growth procedure. After initial desorption of the oxide on the GaAs(100) substrate, the first 100 nm of the GaAs buffer layer was grown at a substrate temperature of 520°C; at this point the temperature was ramped up to 560 °C while the last 400 nm of the buffer layer was grown. The deposition was then stopped for 30s while the temperature was decreased to 525°C. A 6.0 nm $In_{0.17}Ga_{0.83}As$ quantum well layer was then grown. A 80 nm GaAs barrier layer was then grown at 525°C, at which point the sample temperature was ramped to 590°C to grow the last 20 nm of the GaAs barrier. The growth was again paused for 60 sec and the temperature of the substrate was reduced to 525°C. The island layer was then grown according to the procedure described above. The deposition was stopped and the mask took a period of 20 sec to remove from the surface. Finally, a 30 nm GaAs cap layer was grown at the same temperature as the dots were grown.

The sample studied here consisted of a 2x3 mm rectangular segment cut out of the

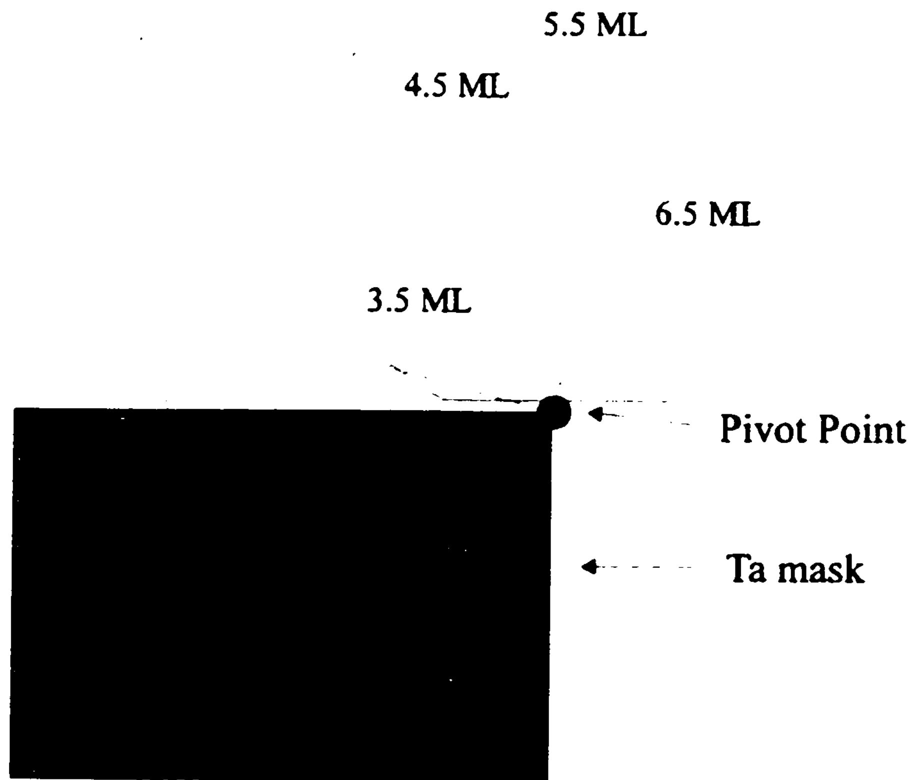

Figure I-3

Illustration of the Ta mask position for the four different phases of the strained InGaAs layer growth. Different amount of material deposited are obtained in each of the regions defined[29].

region of the wafer where 6.5 monolayers of $In_{0.5}Ga_{0.5}As$ were deposited. This sample was cleaved into two approximately equal size pieces, one of which was used for optical experiments presented in chapter V. The second piece was used to obtain structural characterization via a plan view TEM of the island layer as shown in Figure I-4. As can be determined from the TEM picture in Figure I-4, the island areal density is 115 μm^{-2} and their average diameter is 36±3 nm, which yields an areal coverage of 10%. Note that the

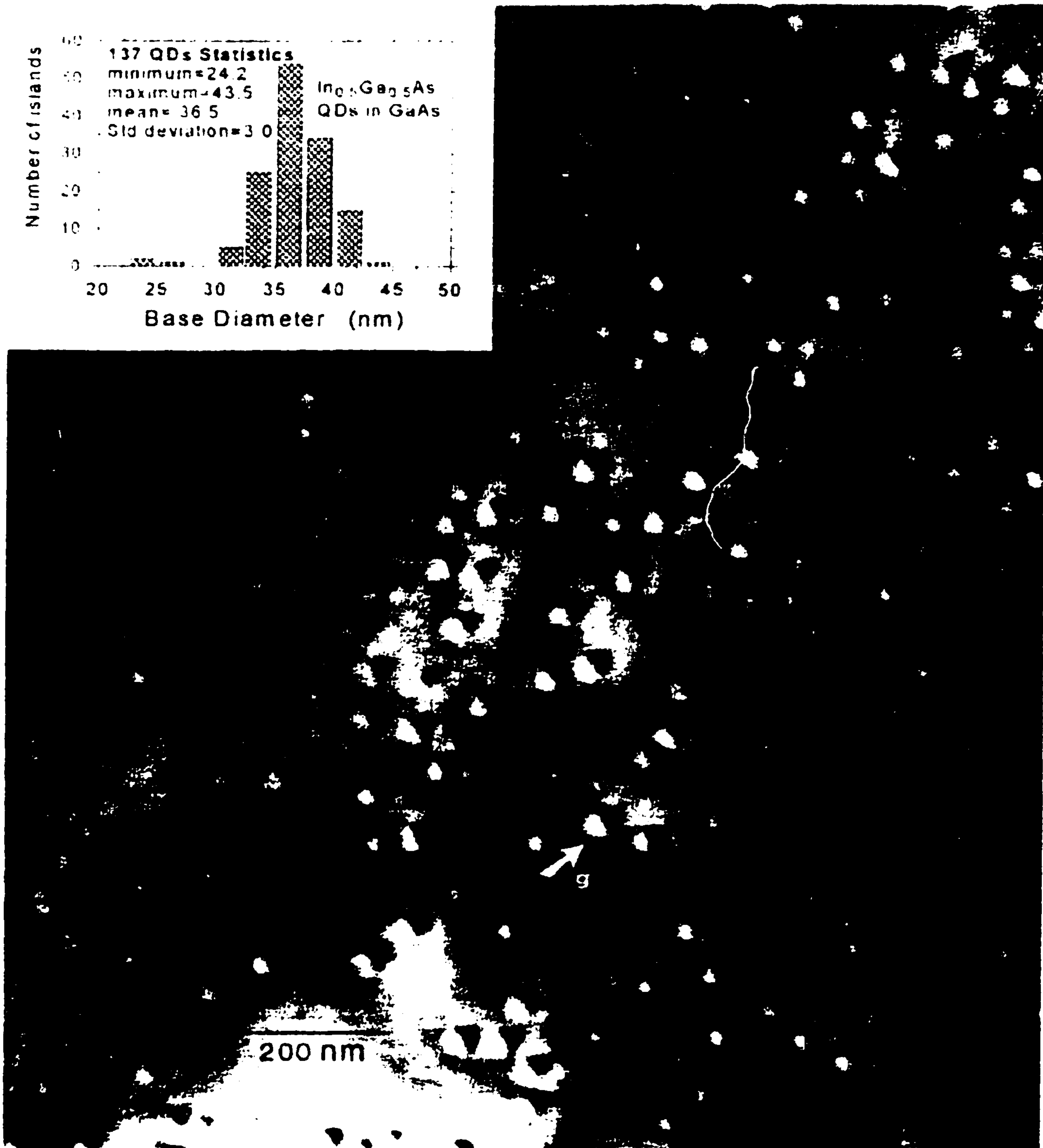

Figure I-4

Dark filed plan view TEM picture of sample IR. Careful inspection of the figure allows us to determine statistics on the base radius presented in the inset of the figure. The areal island density is found to be 115±7 μm^{-2}. Courtesy of Dr. Rosa Leon.

statistics for both samples show a size distribution of about 10% around the mean which is not the ideal situation, particularly for applications. Structural properties of strained InGaAs/GaAs layers have been systematically studied separately[28].

Figure I-5 summarizes the main structural properties of sample VI and IR. At the onset of this study, the electronic shell structure of carriers confined in a strained island layer such as those presented in Figure I-2 and I-4 was not so well known. This explains why, up to this point in the present work, these layers were not referred to as "quantum wells", "quantum wires" or "quantum dots". The terminology used will evolve throughout this thesis as the properties of the electronic states are unveiled by experiments.

Since one of the important goals of this work is to investigate the dimensionality of the bound states in self-assembled layers, the next chapter presents general background information about the different properties of carriers confined in three, two, one or zero dimensions.

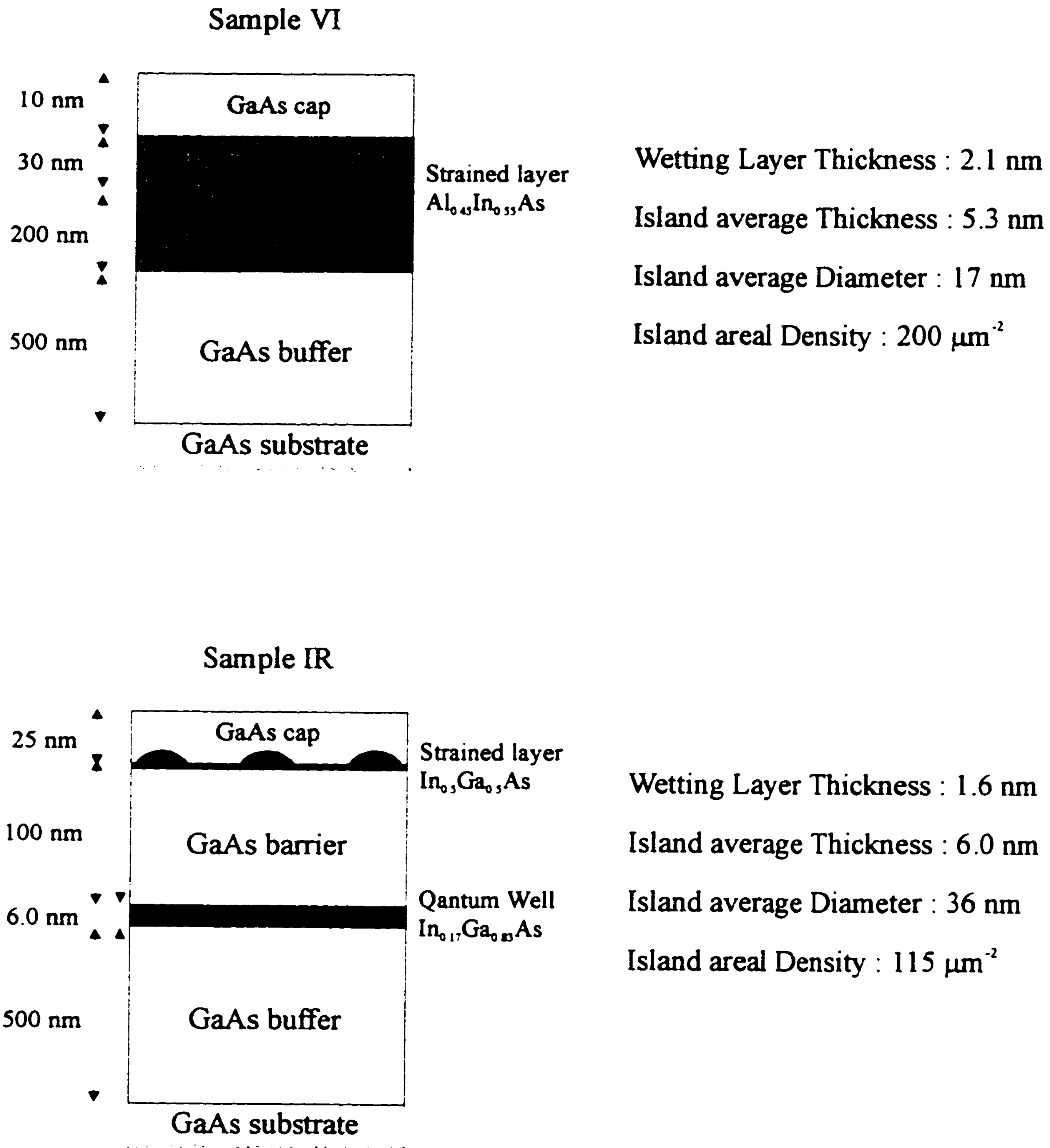

Figure I-5

Layer structure of sample VI and sample IR. On the right hand side, structural parameters of the corresponding sample as obtained from the TEM pictures. The island thickness and wetting layer thickness of sample IR are estimated from the island size, areal density and amount of material deposited.

II THEORY

In this chapter, the basic ideas and concepts used to discuss the experimental results are introduced. First, the concept of dimensionality is presented by calculating the density of states for a few idealized structures. The dimensionality of the electronic states in the self-assembled islands will be established by comparison with these idealized situations in the following chapters. Next, as the TEM pictures revealed the lens-shaped form of the self-assembled islands, the energy levels for carriers confined in a lens-shaped structure are calculated for two different limits: strong and weak lateral confinement. In the strong confinement limit, it is shown that the lower energy levels are well approximated by in-plane harmonic oscillator states. This result is used to calculate the spectrum of a lens-shaped quantum dot in a strong perpendicular magnetic field, which reveals the symmetry of the electronic shells. Also, the selection rules for inter-band and inter-sublevel transitions in semiconductor quantum dots are obtained. Finally, the problem of a quantum well with finite barriers is considered and related phenomenon are introduced.

The envelope function approximation[30] will be used throughout this chapter with φ denoting the total Bloch wavefunction of the carriers, Ψ the slowly varying envelope function and μ the rapidly varying atomic-like function. The relation between these different functions is given by $\varphi(\bar{r}) = \mu(\bar{r})\Psi(\bar{r})$. In direct gap III-V compounds the conduction band shell is an s-like shell and the valence band is a p-like shell[31]. Thus, a natural basis for the rapidly varying part of the Bloch functions is obtained from atomic s

and p wavefunctions, numbering 8 in total. In principle other shells should be included in the basis as well, but their effect is often small in III-V semiconductors. The atomic-like part of the wavefunction is fairly similar for all III-V materials, so that this part of the wavefunction is structure independent, provided only III-V compounds are present in the structure.

On the other hand the envelope function is strongly structure dependent in the sense that its form varies considerably depending on the types of layers present in the sample. The remainder of the chapter therefore focuses on calculating the envelope functions for the different structures considered.

II.1 Density of states for idealized structures

The advantages of structures with reduced dimensionality were briefly discussed from an applied point of view in the introduction. From a fundamental point of view, the question is now: how is it possible to distinguish between these different structures in the laboratory? A key concept to answer this question is the density of states (DOS) which gives us information about the number of carrier states available per unit energy. This function provides a convenient way of summarizing the effect of the structural parameters of a particular sample on its carrier states and it provides very useful information for both calculation and experimental guidance.

To illustrate its use, the DOS is calculated for a few idealized structures as shown on the left hand side in Figure II-1a, b,c and d. Depending on the length scales involved (L_x ,

L_y and L_z), the symmetrically cubic structure will be called bulk, quantum well, quantum wire or quantum dot. The first step in calculating the DOS is to find the spectrum of eigenenergies associated with each structure. If one considers the potential to be zero inside the structure and infinite outside (hard wall approximation), the Schrödinger equation can be written in a way common to all cases:

$$-\frac{\hbar^2}{2m^*}\nabla^2\Psi + V\Psi = E\Psi; \qquad V = \begin{cases} 0\, for\, 0 < x_\nu < L_\nu \\ \infty \quad otherwise \end{cases} \qquad \text{II-1}$$

where m^* is the effective mass of the particles in the material of the cube ; x_ν can stand for x,y or z and L_ν can stand for L_x , L_y or L_z. For a potential with a cubic symmetry, Cartesian coordinates are used and the problem is solve using separation of variables. Inside the cube, equation II-1 can be rearranged as

$$\Psi = \Pi_\nu \Psi_\nu \; ; \; -\frac{\hbar^2}{2m^*}\frac{\partial^2 \Psi_\nu}{\partial x_\nu^2} = E_\nu \Psi_\nu \; ; \; E = \sum_\nu E_\nu \qquad \text{II-2}$$

and one simply has to solve three one-dimensional problems. The boundary conditions applied to find a final solution are given by

$$\Psi(x_\nu = 0) = \Psi(x_\nu = L_\nu) = 0 \qquad \text{II-3a}$$

or

$$\Psi(x_\nu = 0) = \Psi(x_\nu = L_\nu) \qquad \text{II-3b}$$

where the first condition applies to a side of the cube with "microscopic" dimension and the second condition is expressing cyclic boundary conditions used for a side with "macroscopic" length. In order to write the boundary conditions II-3 the origin was

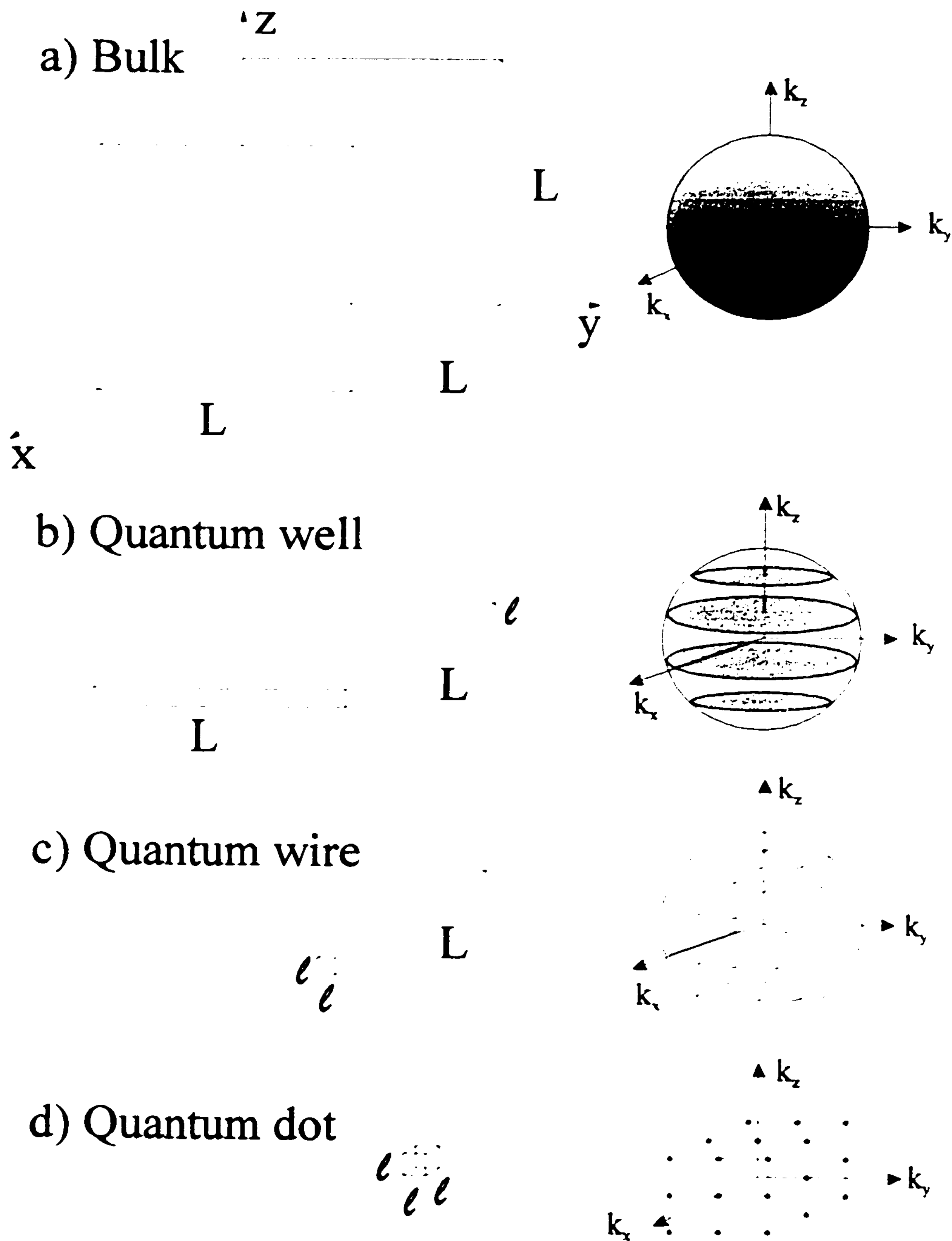

Figure II-1

Evolution of allowed states in k-space as the dimensions of the structure are successively shrunk in each directions. Each time a new dimension becomes microscopic, the corresponding direction of k-space shows discrete increments of allowed states.

taken at one of the corners of the cube as shown in Figure II-1a. Setting all microscopic lengths equal to l and all macroscopic lengths equal to L, the wavefunctions which are solutions to II-2 are respectively given by

$$\Psi_v = \sqrt{\frac{2}{l}} sin(k_v x_v) \quad ; k_v = \frac{\pi n_v}{l} \quad ; n_v = 1,2,... \qquad \text{II-4a}$$

$$\Psi_v = e^{ik_v x_v} \quad ; k_v = \frac{2\pi n_v}{L} \quad ; n_v = \pm 1, \pm 2,... \qquad \text{II-4b}$$

where the former applies to a side of microscopic dimension and the latter applies to a side of macroscopic dimension. The total energy is given by

$$E = \frac{\hbar^2}{2m^*}\left(k_x^2 + k_y^2 + k_z^2\right) \qquad \text{II-5.}$$

The solution $n_v = 0$ has not been included since it would mean we have a solution with $E = 0$ in equation II-1. Applying boundary conditions of the type II-3 would mean that the solution is $\Psi = 0$ which is trivial and unphysical. From the above, one can see that the spectrum of allowed values depends on the dimensions L_x , L_y and L_z so that the interpretation of results II-4 and II-5 will be different for each case presented in Figure II-1.

In the case of bulk material we have $L_v = L \to \infty$ so that solution II-4b is valid in all directions and the complete solution is written

$$\Psi = \sqrt{\frac{1}{L^3}} e^{ik_x x} e^{ik_y y} e^{ik_z z} \qquad \text{II-6a}$$

$$E = \frac{\hbar^2}{2m^*}\left(k_x^2 + k_y^2 + k_z^2\right) \qquad \text{II-6b}$$

where the k_v can be considered as a continuous index which can take any real value as can

be inferred from equation II-4b. To obtain N(k), the number of allowed states up to wavevector k, one should formally perform an integration over the Fermi sphere of radius k. A less rigorous approach which gives the same result is to divide the volume of the Fermi sphere by the differential volume occupied by one state which yields $N(k) = 2\frac{{}^4/_3\pi k^3}{({}^{2\pi}/_L)^3}$ where a factor of two has been introduced to account for spin degeneracy. We use the dispersion relationship of relation II-6b to obtain $N(E) = \frac{L^3}{3\pi^2\hbar^3}(2m^* E)^{3/2}$, and differentiation with respect to E yields the three-dimensional density of states

$$D_{3D}(E) = \frac{m^* L^3}{\pi^2\hbar^3}(2m^* E)^{1/2} \qquad \text{II-7.}$$

This function is continuous and increases monotonously so that more states are available at higher energies.

The cube is now shrunk in the z-direction so that L_z becomes equal to l, a microscopic dimension, and see how it affects the density of states. The complete solution for this quantum well case is

$$\Psi = \sqrt{\frac{2}{lL^2}} e^{ik_x x} e^{ik_y y} \sin\left(\frac{\pi n_z}{l} z\right) \qquad \text{II-8a}$$

$$E = \frac{\hbar^2}{2m^*}\left(k_x^2 + k_y^2\right) + \frac{\hbar^2\pi^2}{2m^*}\frac{n_z^2}{l^2} \qquad \text{II-8b}$$

where equation II-8b is exactly the same as equation II-6b except that we have replaced k_z by its expression $\pi n_z/l$ to stress that it has become a discontinuous index. The Fermi

sphere then contains a finite number of planes of allowed states, each associated with a quantum number n_z as shown on the right hand side of Figure II-1b. To calculate N(k) one has to compute the number of states in a plane and sum over all planes contained in the sphere. From Figure II-2 one can easily see that the total surface of the plane is given by $\pi^2\left(k^2 - k_{nz}^2\right)$ and from the inset the area occupied by one state is given by $\left(\frac{2\pi}{L}\right)^2$. Using a similar reasoning as for the 3-dimensional case the total number of states up to energy E can be shown to be given by

$$N(E) = 2\sum_{k_{nz}^2 < k^2} \frac{\pi(k^2 - k_{nz}^2)}{({}^{2\pi}/_{L})^2} = \frac{L^2}{\pi}\frac{m^*}{\hbar^2}\sum_{k_{nz}^2 < k^2} \frac{\hbar^2}{2m^*}(k^2 - k_{nz}^2) = \frac{m^* L^2}{\pi\hbar^2}\sum_{E_{nz} < E}(E - E_{nz}) \quad \text{II-9}$$

and upon derivation with respect to E

$$\begin{aligned} D_{2D}(E) &= \frac{m^* L^2}{\pi\hbar^2}\sum_{nz}\Theta(E - E_{nz}) \\ E_{nz} &= \frac{\hbar^2\pi^2}{2m^* l}n_z^2 \end{aligned} \quad \text{II-10}$$

where Θ(E) is the heavyside function[32]. Equation II-10 is very different in nature than equation II-7 since we now have a discontinuous function that exhibits a series of plateaus. Moreover, the energy spacing between the plateaus can be tuned by changing the thickness of the microscopic side of the slab.

Next, to obtain the quantum wire DOS, both L_y and L_z are shrunk to microscopic dimensions so that there remains only one direction of macroscopic length. A similar reasoning as for the 2D case yields

$$D_{1D}(E) = \frac{L}{\pi}\left(\frac{2m^*}{\hbar^2}\right)^{\frac{1}{2}}\sum_{ny,nz}(E - E_{ny,nz})^{-\frac{1}{2}}\Theta(E - E_{ny,nz}) \qquad \text{II-11a}$$

$$E_{ny,nz} = \frac{\hbar^2\pi^2}{2m^* l^2}(n_y^2 + n_z^2) \qquad \text{II-11b.}$$

Again, this function is completely different than the 2D or 3D cases. The heavyside function is still present, but the DOS decreases as $E^{-\frac{1}{2}}$ instead of being constant between each energy step. Finally, for the case where all dimensions are microscopic the density of states becomes completely discrete and one can write

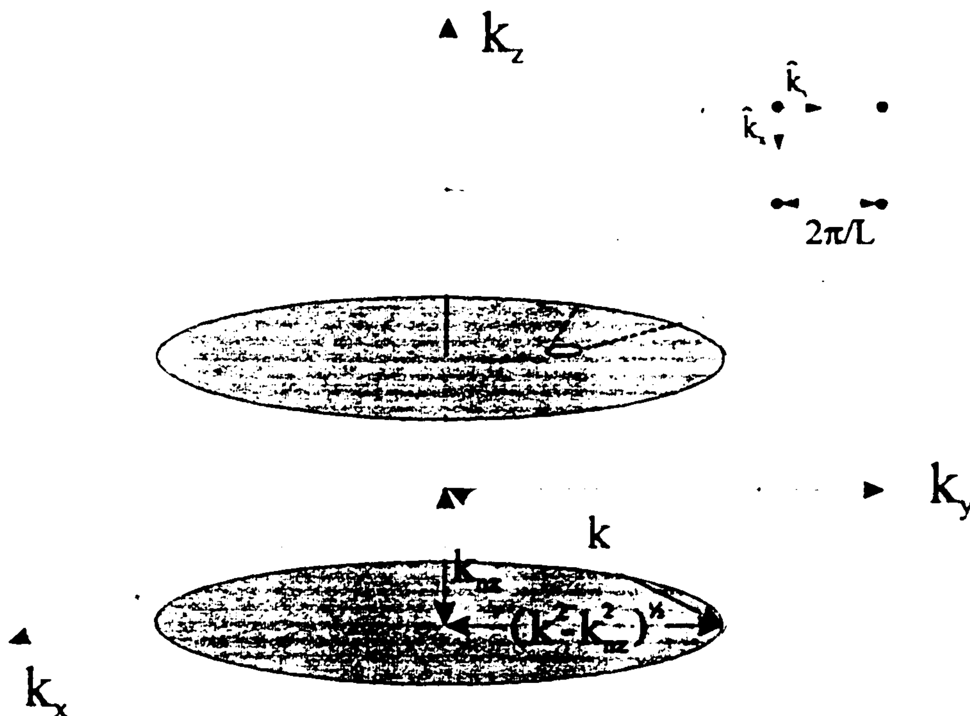

Figure II-2

Planes of allowed states for the case of a quantum well. The radius of plane n_z is given by $\left(k^2 - k_{nz}^2\right)^{\frac{1}{2}}$ and the differential area occupied by each state is shown to be $\left(\frac{2\pi}{L}\right)^2$ in the inset.

$$D_{0D}(E) = 2\delta(E - E_{nx,ny,nz})$$
$$E_{nx,ny,nz} = \frac{\hbar^2\pi^2}{2m^* l^2}(n_x^2 + n_y^2 + n_z^2) \qquad \text{II-12.}$$

From the above discussion, it is clear that the density of states becomes more and more discontinuous as the dimensionality of the structure decreases. Indeed, the DOS in three dimensions proved to be a continuous function whereas in the zero-dimensional case it becomes a discrete δ-like function. This conclusion is in fact independent of the shape of the structure studied, as long as we compare a structure of macroscopic dimensions with a structure of microscopic dimensions. Figure II-3 shows the density of states for the different dimensionalities according to the above results.

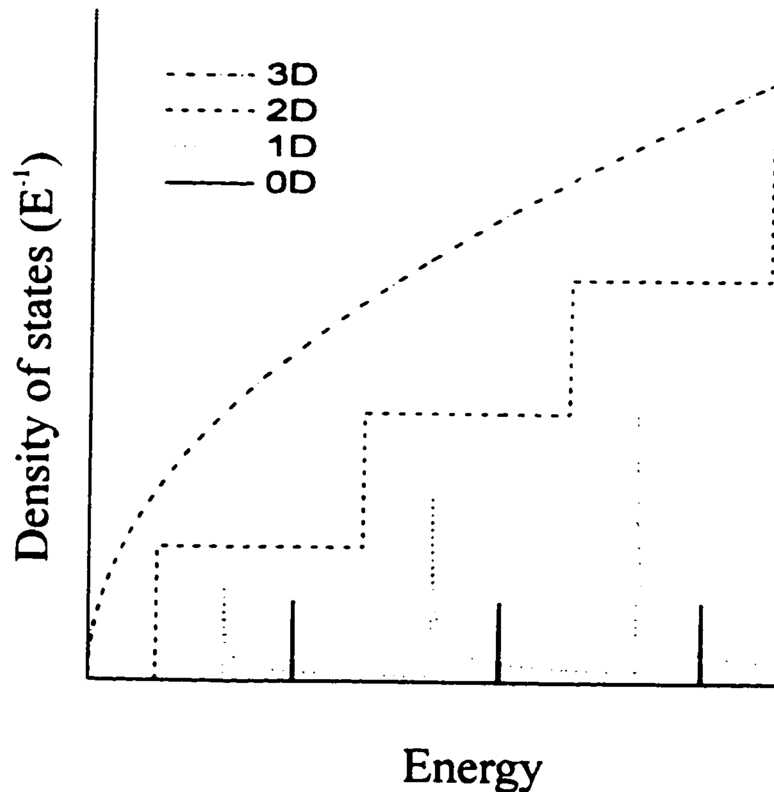

Figure II-3

Density of states for structures of different dimensionalities

To obtain a more concrete example, the density of states for the 6.0 nm QW of sample IR is calculated and compared to the density of states obtained when considering the islands of the strained layer as quantum dots. Considering the case of the conduction band, using equation II-10 with $l = 6.0nm$ and $m^* = 0.0665$, one obtains the step-like function shown in Figure II-4 for the QW DOS. The factor L^2 has been factored out to obtain the density of states per unit area in the plane. The DOS for the strained island is calculated from discrete states with level spacing of 100 meV and degeneracy of 2,4,6... for the ground state, first excited state etc. The degeneracy level is multiplied by the dot areal density and a broadening of 35 meV is included to account for the size/composition inhomogeneity of the island population. Comparing the two curves, one can see that the total number of available states is much higher in the QW layer than in the "QD" layer. Thus, saturation effects should occur for lower carrier populations in the 0D case than in the 2D case. Furthermore, the "real" dot layer does not show the discrete density of states typical of a single dot DOS, since a total of $\sim 10^6$ dots is probed in a typical optical experiment. This problem can be solved by probing a small number of dots.

So far in this chapter the problem of defining the boundary between "macroscopic" and "microscopic" has been avoided. From our discussion it becomes apparent that the transition between those two length scales is a smooth one, and in fact this issue has been addressed by many authors and some have shown, at least in principle, how this transition occurs[33] in real structures. The transition criteria involves the ratio of the length scale of the structure side denoted l, to a length scale related to the barrier height $b = \left\{\hbar^2/2m^*V\right\}^{1/2}$. One starts to see quantum effects when the side of the structure is no

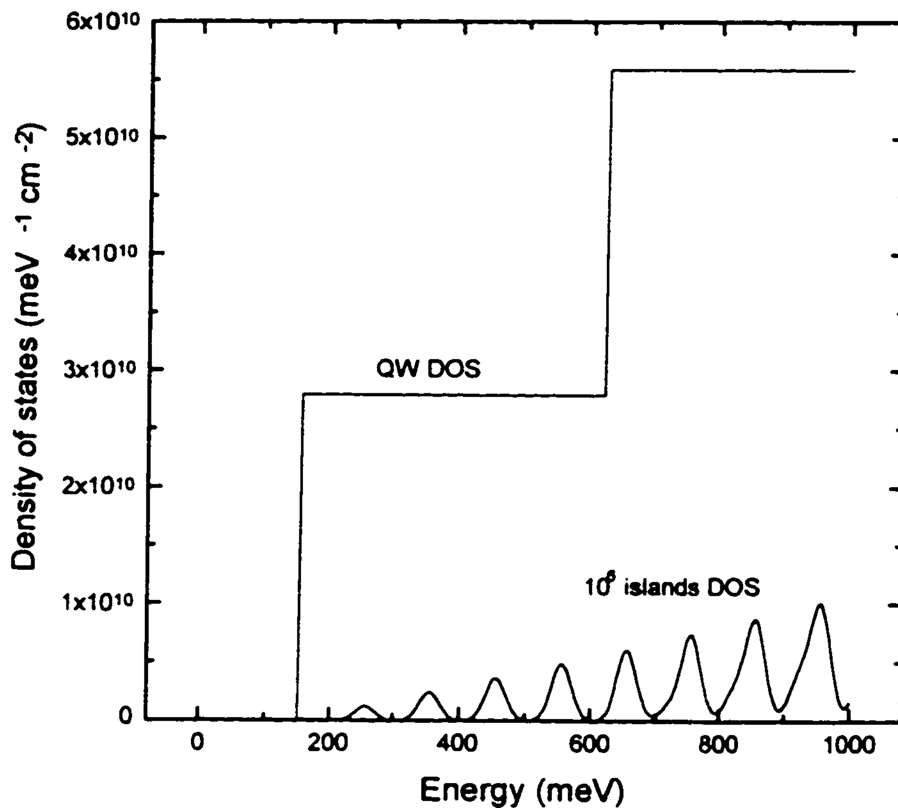

Figure II-4

Comparison of the conduction band density of states for the 2D and strained layer of sample IR.

more than two order of magnitude longer than the "barrier" length scale ($l \approx 100b$). An almost complete crossover from one dimensionality to another is obtained when the two length scales become of the same order of magnitude $l \approx b$. For example, in GaAs the low-temperature gap is given by 1.54 eV compared to 2.0 eV for a typical AlGaAs barrier, and taking the effective mass of the conduction band carriers of GaAs, $m^* = 0.067m_0$ one can estimate the transition length ($l \approx 100b$) to within a factor of two as 110 nm. Other authors, adopting a different point of view, have taken the mean free path of carriers as the critical length scale[34]. Indeed, the reasoning presented in this chapter assumes that the

carrier wavefunction remains coherent throughout the whole length of the structure. This is not true for real structures since carriers experience scattering processes that destroy the phase coherence after traveling an average distance given by the mean free path. This would mean that quantized effects could not be observed unless at least one dimension of the structure is shorter than the mean free path.

To summarize this section, probing the density of states of a given sample allows for the determination of the dimensionality of the confined states. For example, imagine a photoluminescence experiment performed for two different structures, one with a quantum well and the other with a quantum-dot active layer. The electron-hole pairs created in the quantum well are distributed over a continuum of allowed energy states according to a statistical Fermi distribution and the emission line is therefore expected to have a finite linewidth which is dependent on both the excitation intensity and the lattice temperature. On the other hand, the δ-like DOS of a single dot means that its emission spectrum is given by a series of infinitely sharp lines which could not show any broadening owing to excitation power or temperature.

II.2 Energy Levels of a Lens Shaped Quantum Dot

The discussion presented in the opening chapter introduced the concept of self-assembled islands without giving any details as to why this system is expected to show zero-dimensional properties. As was seen on the cross-sectional TEM picture of sample VI these structures are in fact a plane of lens-shaped discs on top of a thin quantum well

layer. Since the island is thicker than the underlying wetting layer, carriers are expected to localize in these regions because of the lower energy of the z-bound state. Also, these discs have a base diameter in the nanometer range and the lateral confinement is expected to play a role. To investigate this, the problem of an electron-hole pair trapped in an ideal lens-shape island is considered. The specific structure considered is made of a hemispherical cap of material A enclosed in a material B, as shown in Figure II-5. The

$$\vec{B} = B\,z$$

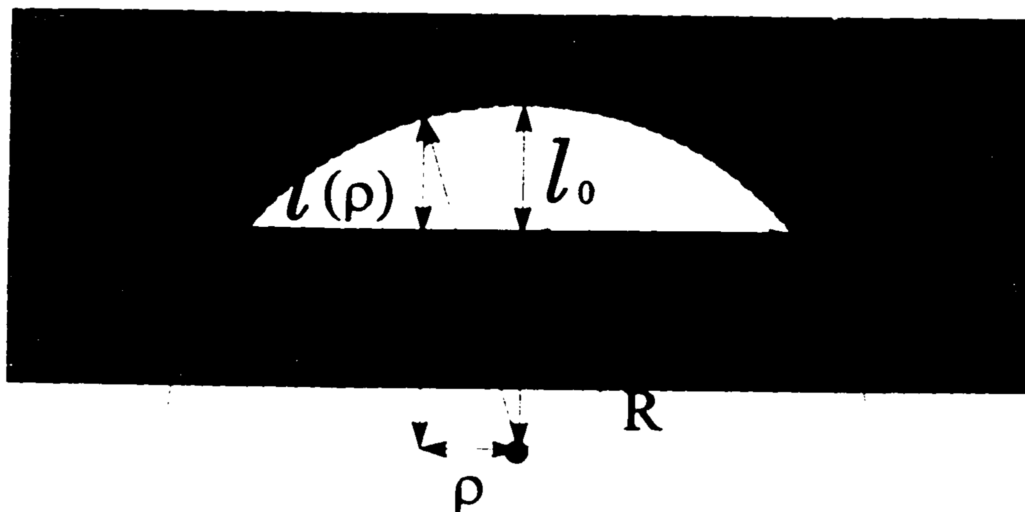

$$l(\rho) = (R^2 - \rho^2)^{1/2} - h$$

Figure II-5

Cross section view of the ideal lens-shaped dot considered as the top of a hemispherical cap. The relationship between the different variables used to calculate the structural part of the potential are shown. The magnetic field line indicates the geometry of the problem considered in section II-3.

effective mass Hamiltonian of this system is given by

$$H = \frac{P_e^2}{2m_e^*} + \frac{P_h^2}{2m_h^*} + V(\bar{r}_e) + V(\bar{r}_h) - \frac{e^2}{\varepsilon|\bar{r}_e - \bar{r}_h|} \qquad \text{II-13}$$

where ε is the zero-frequency dielectric constant of the semiconductor, and $V(\bar{r}_{e(h)})$ is the potential due to the shape of the island and will be referred to as the structural term. The aim of this calculation is to build an expression of the eigenenergies for this structure in two different limits, the limit of strong confinement and the limit of weak confinement. For strong confinement, the structural term dominates the Coulomb interaction and we therefore neglect correlation between the particles. The problem reduces to a one-particle effective-mass Schrödinger equation

$$-\frac{\hbar^2}{2m_{e(h)}^*}\nabla^2\Psi_{e(h)} + V_{e(h)}(\bar{r}_{e(h)})\Psi_{e(h)} = E_{e(h)}\Psi_{e(h)} \qquad \text{II-14}$$

for both electrons and holes. The results can be used to build a non-interacting basis set for the electron-hole pair trapped in the dot. In what follows, the e(h) subscripts is dropped for simplicity, knowing that the results can be applied to electrons or holes alike by simply using the appropriate effective mass and band parameters.

Next, a mathematical expression for $V(\bar{r})$ consistent with the physical shape of the lens-shaped island must be found. Consider, as represented in Figure II-6, a quantum well of thickness l_0 which is transformed into a lens shaped dot of similar thickness at the center with radius at the base ρ_0. The difference in confinement energy (respectively given by E_z and E_z+$E_{lat.}$) comes from an extra lateral confinement which suggests that the potential $V(\bar{r})$ can be separated in

$$V(\vec{r}) = V(z) + V(\rho) \qquad \text{II-15}$$

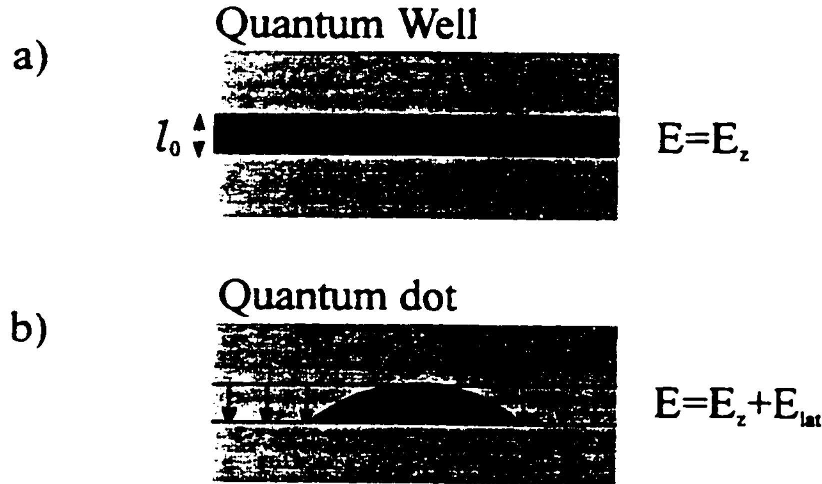

Figure II-6

Change in confinement energy as the structure goes from a quantum well to a quantum dot shape. The difference between the two cases comes from extra lateral confinement.

where $V(z)$ is simply the potential profile of a quantum well of thickness l_0. To obtain an explicit form for V(ρ), the so-called adiabatic approximation[35] is used. This method states that the potential a particle feels when moving in the x-y plane is given at each point by the ground state energy of a quantum well of equivalent thickness $l(\rho)$. Such an approximation was also used in solving quantum wire problems[36] with non-planar geometry. For simplicity, the hard wall approximation is used to calculate the explicit form of V(ρ), such that expression II-10 for E_z can be used, replacing l by $l(\rho)$. The potential then is

$$V(\rho) = E_{QW}(l(\rho)) - E_{QW}(l_0) = \frac{\hbar^2\pi^2}{2m^* l^2(\rho)} - \frac{\hbar^2\pi^2}{2m^* l_0^2} \qquad \text{II-16}$$

and upon replacement of $l(\rho)$ by the expression obtained from Figure II-5, one obtains

$$V(\rho) = \frac{\hbar^2\pi^2}{2m^*}\left\{\frac{1}{\left[\left(R^2-\rho^2\right)^{1/2}-h\right]^2}-\frac{1}{l_0^2}\right\} \qquad \text{II-17.}$$

Solving equation II-14 with a potential of the form given by equations II-15 and II-17 could be done numerically with very little intuitive insight. Instead, a harmonic approximation can be obtained from a Taylor series expansion of $V(\rho)$:

$$V(\rho) \cong \frac{\hbar^2\pi^2}{2m^*R^2}\left\{\frac{1}{\left(1-{h \over R}\right)^3}\left(\frac{\rho}{R}\right)^2+\frac{1}{4}\frac{4-{h \over R}}{\left(1-{h \over R}\right)^4}\left(\frac{\rho}{R}\right)^4+O(\rho^6)\right\} \qquad \text{II-18.}$$

One very important parameter in self-assembled islands is the aspect ratio $A=\frac{l_0}{\rho_0}$. Since this parameter is known to be fairly small (~0.2) for most material systems studied here[29], equation II-18 can be re-written as :

$$V(\rho) = \frac{\hbar^2\pi^2}{2m^*l_0^2}\left\{\frac{2}{\left(1+A^2\right)}\frac{\rho^2}{\rho_0^2}\left(1+\frac{A^2\left(3+5A^2\right)}{2\left(1+A^2\right)^2}\frac{\rho^2}{l_0^2}\right)\right\} \qquad \text{II-19}$$

and the quadratic term is therefore dominant if

$$\frac{A^2\left(3+5A^2\right)}{2\left(1+A^2\right)^2}\frac{\rho^2}{l_0^2} \ll 1 \text{ or } \frac{\rho}{\rho_0} \ll 0.8 \text{ for A=0.2} \qquad \text{II-20.}$$

and in this case equation II-14 reduces to

$$-\frac{\hbar^2}{2m^*_{e(h)}}\nabla^2\Psi_{e(h)}+\left\{V_{e(h)}(z)+\tfrac{1}{2}m^*_{e(h)}\omega^2_{e(h)}\left(x^2+y^2\right)\right\}\Psi_{e(h)} = E_{e(h)}\Psi_{e(h)} \qquad \text{II-21a}$$

where $$\omega_{e(h)}^2 = \frac{4A^2}{\left(1+A^2\right)} \frac{\pi^2\hbar^2}{\left(m_{e(h)}^*\right)^2 l_0^4} \qquad \text{II-21b}$$

This eigenvalue equation is now entirely separable into a square well in the z-direction and a harmonic oscillators in each of the x and y directions. The solutions for the quantum well bound state energies are given in equation II-10 while the solution of the harmonic oscillator can be found in the literature[37]:

$$E_z = \frac{\hbar^2\pi^2}{2m^* l_0^2}$$

$$E_x + E_y = \left(n_x + n_y + 1\right)\hbar\omega = \left(n_x + n_y + 1\right)\frac{2}{\pi}\sqrt{\frac{2A^2}{\left(1+A^2\right)} \frac{\hbar^2\pi^2}{2m^* l_0^2}} \qquad \text{II-22.}$$

$$n_x, n_y = 1, 2, \ldots$$

where the subscripts e(h) have been dropped for simplicity. The result applies for both band with the appropriate effective mass and frequency (ω). Equation II-22 includes only the z ground state energy as this proves to be sufficient for most self-assembled island systems (i.e. the islands are thin due to the fact that the growth has to be stopped early in order to avoid dislocations). Result II-22 implies that there is no more energy continuum associated with the x and y directions since all the parameters included in II-22 are now finite. A zero-dimensional energy spectrum has been obtained and this conclusion holds even for structures with finite potential barriers. In this case expression II-8b cannot be used to link the energy levels of a square well with its width and a more complicated expression has to be used. However, it remains true that the bound state energy increases smoothly with decreasing well width, and the lateral confinement is still strong enough to produce zero-dimensional states. In this case quantitative results are obtained by fitting the

obtained form of V(ρ) to the closest harmonic function, or simply by solving the radial potential numerically[35].

A quantitative criteria of the validity of the harmonic approximation can be obtained. The leakage of the wavefunction is expected to be more important where the effective thickness of the well is smaller, near the edge of the dot. The hard wall approximation is therefore not accurate for higher excited states since the presence probability near the edge of the dot increases with n. For a harmonic oscillator the spatial uncertainty in any direction is given by $\Delta X = \sqrt{\left(n+\frac{1}{2}\right)\frac{1}{\beta}}$ where $\beta = \sqrt{\frac{m^* \omega}{\hbar}}$ is the well-known inverse length scale used to describe the harmonic oscillator wavefunction. Using result II-22, the spatial extension of the wavefunction can be estimated as a function of n. From the results presented in Table II-1 it can be seen that the harmonic approximation produces acceptable results for the lowest lying states since condition II-20 is then respected.

Level	ΔX
n=0	$0.076\rho_0$
n=1	$0.131\rho_0$
n=2	$0.169\rho_0$
n=3	$0.200\rho_0$
n=4	$0.227\rho_0$

Table II-1

Extension of the wavefunction away from the center of the dot as given by the uncertainty on the particle position for different energy levels.

At the other end of the spectrum, the weak confinement limit is reached if the base radius is large enough for the structural terms of the potential in Hamiltonian II-13 to be negligible, so that one is left with the well known excitonic problem for which the eigenvalue equation can be written in terms of the electron and hole position and momentum

$$\left(\frac{P_e^2}{2m_e^*}+\frac{P_h^2}{2m_h^*}-\frac{e^2}{\varepsilon|\vec{r}_e-\vec{r}_h|}\right)\Psi = E\Psi \qquad \text{II-23}$$

The center of mass and relative positions and momenta can be used to simplify this equation

$$\vec{r}_{CM}=\frac{m_e^*\vec{r}_e+m_h^*\vec{r}_h}{m_e^*+m_h^*}; \qquad \vec{r}=\vec{r}_e-\vec{r}_h$$

$$\vec{P}_{CM}=\vec{P}_e+\vec{P}_h; \quad \vec{P}=\frac{m_h^*\vec{P}_e-m_e^*\vec{P}_h}{m_e^*+m_h^*}$$

so that one can write

$$\left(\frac{P_{CM}^2}{2M^*}+\frac{P^2}{2\mu^*}-\frac{e^2}{\varepsilon|\vec{r}|}\right)\Psi = E\Psi \qquad \text{II-24}$$

where M^* and μ^* are the total and reduced mass of the electron-hole pair respectively. This equation can be separated in a free particle Hamiltonian for the center of mass coordinates and a Hydrogen-like Hamiltonian for the relative coordinates so that the solutions for E are given by

$$E_n^{exc} = \frac{\hbar^2 K_{CM}^2}{2M^*} - \frac{R^*}{n^2}; \quad n = 1,2,... \qquad \text{II-25a}$$

$$R^* = \frac{\mu^* e^4}{2\varepsilon_r^2 \hbar^2} \qquad \text{II-25b}$$

where the first term in II-25a reflects the center-of-mass motion of the electron-hole pair, and the second term is a hydrogen-like spectrum due to the internal degrees of freedom of the electron-hole pair. The "atom" composed of an electron and a hole interacting via the Coulomb interaction with a spectrum given by II-25a is referred to as an exciton (thus the "exc" superscript used in the left hand side of II-25a). The binding energy of the n=1 exciton relative to a free electron-hole pair at the band edge is often called the exciton Rydberg and its expression is given in II-25b.

The weak confinement limit really brings to light the effect of Coulomb interactions in semiconductor structures. However, coulombic interactions are also present in the strong confinement, but represent only a perturbation with respect to the structural term, and the spectrum of eigenstates will simply be somewhat shifted by the Coulomb energies involved in the problem. Thus, the concept of exciton is clearly defined in bulk structures when one obtains a Hydrogen-like spectrum[38], but this definition fades in zero-dimensional structures since the excited states observed can be ascribed to a structural origin rather than the Coulomb interaction. Moreover, excitons cannot be considered as being isolated and non-interacting when present in the same dot. In this case it is more accurate to think in terms of a "droplet" of interacting electrons and holes.

II.3 Spectrum of a Parabolic Dot in a Strong Magnetic Field

It was already pointed out in section II-1 how a structure with zero-dimensional properties can be identified by probing the density of states for various temperatures and excitation powers through the photoluminescence emission spectrum. An alternate method to ascertain the zero dimensional nature of a structure is to look at its properties in a magnetic field. Unlike a quantum well the emission line of a two-dimensional parabolic quantum dot subject to a magnetic field perpendicular to the plane of the quantum dot (see Figure II-5) should show a Zeeman splitting much like that of atomic "p" orbitals. This problem was first discussed by Fock[39] and Darwin[40] for the single-particle case and later extended to more complex situations by several authors[41,42,43,44]. Following the discussion of the previous section, the in-plane potential can be approximated by a parabolic form for the case of lens-shaped dots and applying a magnetic field in the z-direction the in-plane single-particle Hamiltonian can be expressed as[38]

$$H = \frac{1}{2m^*}\left(P_x + q\frac{By}{2}\right)^2 + \frac{1}{2m^*}\left(P_y - q\frac{Bx}{2}\right)^2 + \frac{1}{2}m^*\omega^2\left(x^2 + y^2\right) \qquad \text{II-26}$$

where q and m^* are the charge and effective mass corresponding to the particle studied, B is the magnitude of the magnetic field and ω^2 is given by II-21b. The first two terms have been obtained with a vector potential of the form $\vec{A} = -\frac{1}{2}By\hat{x} + \frac{1}{2}Bx\hat{y}$ for a magnetic field in the z direction. Expanding the squares in the first two terms and rearranging yields

$$H = \frac{1}{2m^*}\left(P_x^2 + P_y^2\right) + \frac{1}{2}m^*\Omega^2\left(x^2 + y^2\right) + \frac{1}{2}\omega_c\left(XP_y - YP_x\right) \qquad \text{II-27}$$

with $\omega_c = qB/m^*$ the cyclotron frequency and a new oscillator frequency given by

$$\Omega^2 = \left(\omega^2 + \left(\frac{\omega_c}{2}\right)^2\right) \qquad \text{II-28}$$

The first two terms of equation II-27 are just the harmonic oscillator equation of frequency Ω while the last term contains the z-component of the angular momentum and is in fact a Zeeman interaction term. This suggests writing the Hamiltonian in terms of the circularly polarized creation-annihilation operators

$$a_+ = \frac{1}{2}\left(\beta(X - iY) + \frac{i}{\beta\hbar}\left(P_x - iP_y\right)\right) \qquad \text{II-29a}$$

$$a_- = \frac{1}{2}\left(\beta(X + iY) + \frac{i}{\beta\hbar}\left(P_x + iP_y\right)\right) \qquad \text{II-29b}$$

where $\beta = \sqrt{m^*\omega / \hbar}$ has been introduced for clarity. The Hamiltonian then takes on the form

$$H = \hbar\Omega_+\left(a_+^\dagger a_+ + \tfrac{1}{2}\right) + \hbar\Omega_-\left(a_-^\dagger a_- + \tfrac{1}{2}\right) \qquad \text{II-30a}$$

$$\Omega_\pm = \Omega \pm \omega_c = \left\{\omega^2 + \left(\frac{\omega_c}{2}\right)^2\right\}^{\frac{1}{2}} \pm \left|\frac{\omega_c}{2}\right| \qquad \text{II-30b}$$

from which one can immediately write the energy spectrum of the eigenstates

$$\begin{aligned} E_{n+,n-} &= \left(n_+ + \tfrac{1}{2}\right)\hbar\Omega_+ + \left(n_- + \tfrac{1}{2}\right)\hbar\Omega_- \\ n_+ &= 0,1,2,\ldots;\, n_- = 0,1,2,\ldots \end{aligned} \qquad \text{II-31}$$

The result II-31 can be compared to II-22 where the energy quanta of different

polarization were degenerate. This degeneracy is lifted by the magnetic field which tunes the energies of the quanta with different circular polarization and one should note that the energy will be raised for one of the polarizations while it will be lowered for the other. This Zeeman type of interaction obtained in the case of harmonic oscillators is in contrast with the case of an electron-hole pair trapped in a quantum well for which the energy is increased by the application of a perpendicular magnetic field[45]. For the special case of an in-plane parabolic confinement, this provides an alternative way to determine if the shell structure of the energy levels is consistent with zero-dimensional states.

II.4 Selection rules for electron transitions

Selection rules for radiative transitions are readily accessible in the literature for bulk and QW semiconductor structures[46]. Such is not generally the case for quantum wire and quantum dot structures. Given their importance for the interpretation of experimental results, selection rules are obtained here in the context of free electron-hole pairs (band-to-band transitions) for the cubic structures of Figure II-1 for all dimensionalities. Then, following that example the more relevant case of a lens-shape dot is considered. Phonon-assisted transitions will also be considered as phonon emission/absorption plays an important role in carrier dynamics for semiconductor structures. Also, similar selection rules for phonon and photon-assisted transitions are discussed in the case of excitons.

II.4.1 Band-to-band transitions

The photon-assisted transition rate between a given initial and final state can be derived in quantum mechanics from Fermi's golden rule[47] when considering the effect of a time-varying electric field of frequency ω on the system. The transition rate between an occupied non-degenerate initial state $|i\rangle$ and an empty non-degenerate final state $|f\rangle$ is given by:

$$w_{i\to f} = \frac{2\pi}{\hbar}\left|\langle f|V|i\rangle\right|^2 \delta\left(E_i - (E_f + \hbar\omega)\right) \qquad \text{II-32}$$

where stimulated emission has been considered ($E_i > E_f$) and $\hbar\omega$ is the energy of the emitted photons. V is the spatial amplitude of the Hamiltonian perturbation due to the time-varying electric field. In the electric dipole approximation V reduces to[48]

$$V = \frac{ieF}{2m_0\omega}\vec{\varepsilon}\bullet\vec{p} \qquad \text{II-33}$$

where F is the amplitude of the electric field, m_0 is the free electron mass, $\vec{\varepsilon}$ the incident electric field polarization and $\vec{p}$ is the electron momentum. In equation II-32 the argument of the δ-function expresses the condition of energy conservation. Other conditions for allowed interband transitions are obtained from the matrix element of V between the final and initial states. Writing $|i\rangle$ and $|f\rangle$ in terms of atomic-like and envelope function yields[49]

$$\langle f|\vec{\varepsilon}\bullet\vec{p}|i\rangle = \vec{\varepsilon}\bullet\langle \mu_f|\vec{p}|\mu_i\rangle\langle \Psi_f|\Psi_i\rangle \qquad \text{II-34}$$

where $|\mu_i\rangle$ ($|\mu_f\rangle$) is the atomic Bloch function for the electron in the initial state (final

state) and $|\Psi_i\rangle$ ($|\Psi_f\rangle$) is the electron envelope function in the initial (final) state. The first term on the right hand side of equation II-34 gives the selection rules related with the light polarization while the second term is the overlap integral between the initial and final states. As mentioned in the introduction of this chapter, the atomic-like part of the Bloch function is similar for all III-V materials and the polarization selection rules are structure (i.e. dimensionality) independent. On the other hand, the envelope functions are structure dependent and selection rules have to be build for each case.

For carriers confined in cubic structures, the envelope functions are given by equations II-4

$$\Psi_v^e = \sqrt{\frac{1}{L}}e^{ik_v^e x_v} \quad or \quad \sqrt{\frac{2}{l}}\sin\left(\frac{\pi n_v^e}{l}z\right) \qquad \text{II-35a}$$

$$\Psi_v^h = \sqrt{\frac{1}{L}}e^{-ik_v^h x_v} \quad or \quad \sqrt{\frac{2}{l}}\sin\left(\frac{\pi n_v^h}{l}z\right) \qquad \text{II-35b}$$

where the functions on the right apply to a side of macroscopic dimension and the functions on the left side apply to a side of microscopic dimension. Note that in II-35, the hole wavevector is taken as the opposite of that of the electron absent from the valence band. Upon integration one obtains the following selection rules

$$k_v^e = -k_v^h \qquad \text{II-36a}$$

$$n_v^e = n_v^h \qquad \text{II-36b.}$$

where the first condition applies for macroscopic side directions for which a smooth dispersion relationship is obtained, and the second condition applies to strongly confined directions. Note that in selection rule II-36a the photon wavevector is neglected. Equation

II-36a means that electronic radiative transitions have to be vertical in k-space, while II-36b restricts those transitions to states with same sub-band index.

In the case of lens-shaped islands, quantum dot wavefunctions have to be used, which for the first few levels can be approximated by in-plane harmonic functions. The length scale of these eigenfunctions are given by $\left(\hbar / m^{*}_{e(h)}\omega\right)^{\frac{1}{2}}$ and using equations II-21b this length scale is found to be $\left(\frac{1+A^2}{A^2}\right)^{\frac{1}{4}} \frac{l_0}{\sqrt{2\pi}}$ which is the same for both electrons and holes. This means that the set of envelope functions describing carriers in both bands is exactly the same. Taking into account only one bound state in the z direction, the selection rules are given by the overlap integrals

$$\left\langle \Psi^{e}_{nx,ny}(x,y) \middle| \Psi^{h}_{nx,ny}(x,y) \right\rangle = \left\langle \Psi^{h}_{nx} \middle| \Psi^{e}_{nx} \right\rangle \left\langle \Psi^{h}_{ny} \middle| \Psi^{e}_{ny} \right\rangle \qquad \text{II-37}$$

and since these functions form a basis set, they are orthogonal and the selection rules are

$$n^{e}_{x} = n^{h}_{x} \qquad ; \qquad n^{e}_{y} = n^{h}_{y} \qquad \text{II-38}$$

A similar argument could be made concerning selection rules for phonon-assisted transitions. In this case the atomic displacement of the ions in the crystal create a local electric dipole field vibrating at the same frequency as the involved phonon. The main difference is that the phonon itself now carries a momentum $\vec{q}$ that has to be considered. Considering only the case of phonon emission, one can write the selection rules as

$$E_f = E_i - \hbar\omega_q \qquad \text{II-39a}$$

$$\vec{k}^{e}_{f} = \vec{k}^{e}_{i} - \vec{q} \qquad \text{II-39b}$$

To illustrate the difference between photon- and phonon-induced transitions, we first

look at an example of phonon dispersion relationship for a one-dimensional semiconductor crystal with two atoms in the primitive cell, as shown in Figure II-7. The acoustic branch corresponds to atomic displacement waves for which the atoms of a given primitive cell move in phase, whereas for the optical branch their phase is opposite, as shown in the insets of the figure. One of the important features suggested by the graph is the weak dependence of the energy of optical phonons on their momentum. This feature holds true for materials for which the interaction between ions of a same primitive cell is much stronger than that for ions of different primitive cells. In three dimensional lattices each branch accepts several polarization for the displacement field and we obtain several curves for each branch, but the qualitative form of the dispersion relationships remain the same within a given branch. Figure II-8 summarizes the possible phonon- and photon-assisted

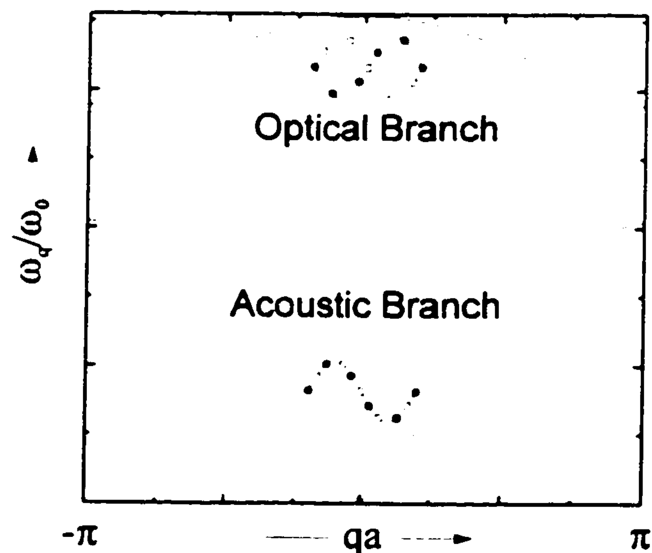

Figure II-7

Dispersion relationship for phonons in a uni-dimensional crystal with two atoms in the primitive cell. In the upper optical branch the phonons carry an amount of energy which has a weak dependence on q and is non-zero at q=0.

transitions for structures with at least one direction of continuous dispersion (electrons in a bulk, well or wire) and in a cubic quantum dot. In the first case, inter-band transitions are very easily mediated by photons which can take any energy, but according to equation II-36a this transition has to be vertical in k-space (the wavevector ascribed to the hole is minus the wavevector of the promoted electron). For semiconductors, phonon-mediated inter-band transitions are forbidden in first order since even the optical phonon energies are much smaller than the bandgap. For example in GaAs the optical phonons have an energy of approximately 36 meV compared to a bandgap of 1.4 eV at room temperature. Intra-band transitions are more likely to be phonon-assisted since transitions cannot be vertical in k-space and small energy steps are allowed. The same reasoning applies to quantum boxes, but with one difference. Since the dispersion relationship is now discontinuous it is likely that phonon assisted intra-band transitions are forbidden to first order, for example if the smallest energy difference is greater than the optical phonon energies, or if it falls in the phononic gap of Figure II-7. This restricted phonon relaxation rate for intra-band transitions is often referred to as the phonon bottleneck. Some authors have invoked such an effect to account for the poor luminescence intensity observed in some early low-dimensional structures[50], and the debate about this issue remains an important one.

Finally, it should be mentioned that intra-band and inter-band transitions can be mediated by carrier-carrier (ex. Auger) scattering. For example, an electron in an excited quantum dot state can relax to the ground state by giving its extra energy to an electron in neighboring material.

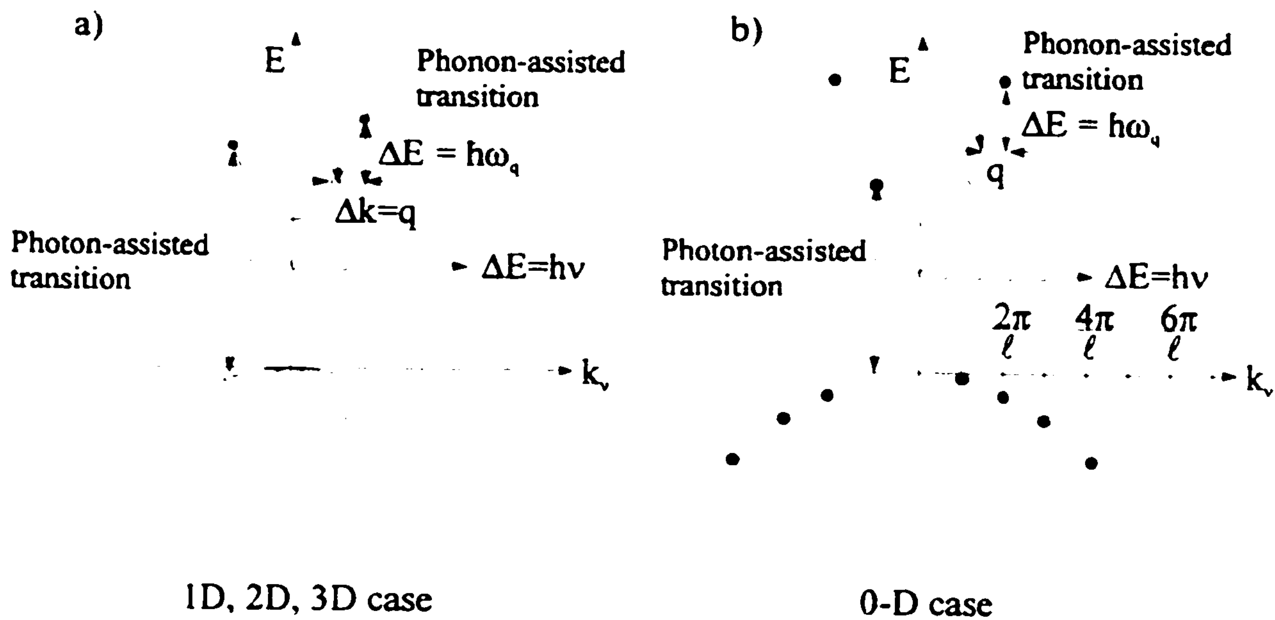

Figure II-8

Illustration of electron transitions. a) In a structure with at least one macroscopic direction. Photon-assisted transitions are vertical and generally inter-band whereas phonon-assisted transitions are generally non-vertical and intra-band. b) For zero-dimensional structures the situation is similar except that intra-band phonon transitions can be forbidden if the smallest energy difference is higher than the optical phonon energies. This phonon bottleneck effect is exemplified for a conduction-band transition in the 0D case. Since a single phonon energy cannot match the inter-level spacing, multi-phonon transitions are higher order and therefore slower.

II.4.2 Excitonic transitions

The presence of Coulomb interaction between the electron and hole states modifies the band-to-band picture presented in the previous section. The calculations involving Coulomb interactions in quantum dots is still a matter of discussion at this time, and the models usually require tedious calculations. Discussing excitonic effects for the various dimensionalities is therefore beyond the scope of this work. However, bulk exciton

properties are well documented in the literature and some of these results will be useful as a basis for comparisons with the results of the present work. Figure II-9 presents the dispersion relationship obtained for bulk excitons, as per equation II-25. A series of curves is obtained for each value of n, and eventually a continuum of electron-hole pairs is obtained. The binding energy for bulk excitons is of the order of 5 meV in GaAs (from equation II-25). The selection rules for radiative transitions are given by

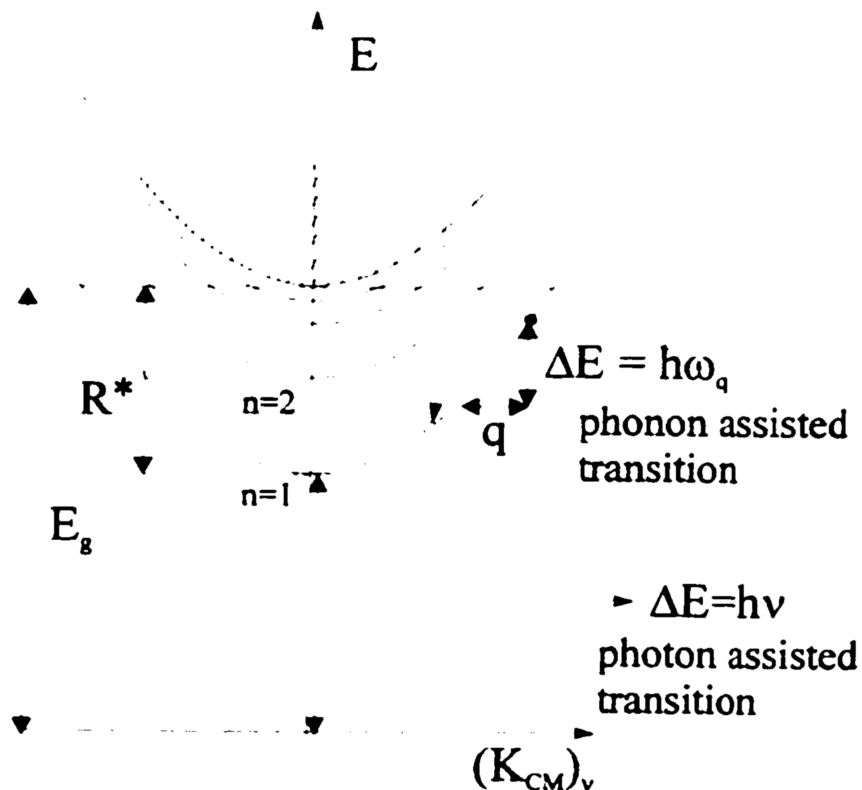

Figure II-9

Dispersion relationship for an exciton state shown along one of the three axes of quantization. For each value of n a new curve is obtained.

$$\vec{K}_{CM} = 0 \quad \text{II-40a}$$

$$E_g + E_n^{exc} = \hbar\omega \quad \text{II-40b}$$

where the photon wavevector is neglected in II-40a, and E_g is the semiconductor bandgap. The equivalent set of rules for phonon emission assisted transitions is

$$\vec{K}_{CM}^{f} = \vec{K}_{CM}^{i} - \vec{q} \quad \text{II-41a}$$

$$\Delta E^{exc} = -\hbar\omega_q \quad \text{II-41b}$$

Where $\vec{q}$ is the momentum carried by the phonon.

An interesting remark about the dispersion relationship presented in figure II-9 combined with the above selection rules is that it gives rise to a set of narrow emission (or absorption) lines below the bandgap with a FWHM independent of temperature and excitation intensity. Indeed, let us assume a low exciton density is present so that only the edge of the n=1 dispersion curve is populated. If the temperature is raised moderately, only non-radiative high center-of-mass states are populated and the emission line is not broadened. In this case however, the intensity of the emitted luminescence is quenched even at very low temperatures. For similar reasons, raising the Fermi level (higher exciton concentration) does not cause broadening of the exciton line. However, the above selection rules have neglected acoustic phonon scattering, and it has been shown that the homogenous linewidth of an exciton is broadened as the temperature is raised due to exciton-acoustic phonon interactions[51,52].

Also, at higher temperatures and higher Fermi levels the radiative decay rate of the exciton population is considerably slowed down as most carriers are forced to dwell in

non-radiative high momentum states. This should be reflected in time-resolved experiments as a longer effective carrier lifetime.

II.5 Finite potential barrier and related effects

In order to simplify the discussion, only infinite potential barriers were considered so far. In real semiconductor structures the barrier material has a finite bandgap and consequently the barrier heights are finite. Figure II-10 shows the potential profile obtained when a thin layer of low-gap semiconductor is surrounded by a high-gap semiconductor material. E_g^{qw} and E_g^{bar} are the energy gap of the QW and barrier material respectively so that the total band discontinuity is given by $\Delta E_g = E_g^{bar} - E_g^{qw}$. Q_c and Q_v are the conduction band and valence band offset respectively, and the conduction (valence) band discontinuity is given by $V_0^c = Q_c \bullet \Delta E_g$ ($V_0^v = Q_v \bullet \Delta E_g$).

A first consequence of finite band discontinuities is that for the same well width, the bound state energies are changed with respect to the infinite band discontinuity case. The symmetry of the finite well problem is exactly the same as that of the infinite well considered in section II-1, and the Hamiltonian can be separated in the same way along the axis directions. For x and y the well layer has macroscopic dimensions so that the solution in these directions are exactly the same as those given in equation II-4b, provided the potential is taken to be zero in the well layer:

$$\Psi_x = e^{ik_x x} \qquad ;k_x = \frac{2\pi n_x}{L} \qquad ;n_x = \pm 1, \pm 2, \ldots \qquad \text{II-42a}$$

$$\Psi_y = e^{ik_y y} \qquad ;k_y = \frac{2\pi n_y}{L} \qquad ;n_y = \pm 1, \pm 2, \ldots \qquad \text{II-42b}$$

$$E_{x,y} = \frac{\hbar^2}{2m^*}\left(k_x^2 + k_y^2\right) \qquad \text{II-42c}$$

However, in the z direction the problem reduces to

$$-\frac{\hbar^2}{2m^*(z)}\nabla^2\Psi_z + V(z)\Psi_z = E_z\Psi_z ; \quad V(z) = \begin{cases} 0 \; for \; 0 < z < l \\ V_0 \quad otherwise \end{cases} \qquad \text{II-43}$$

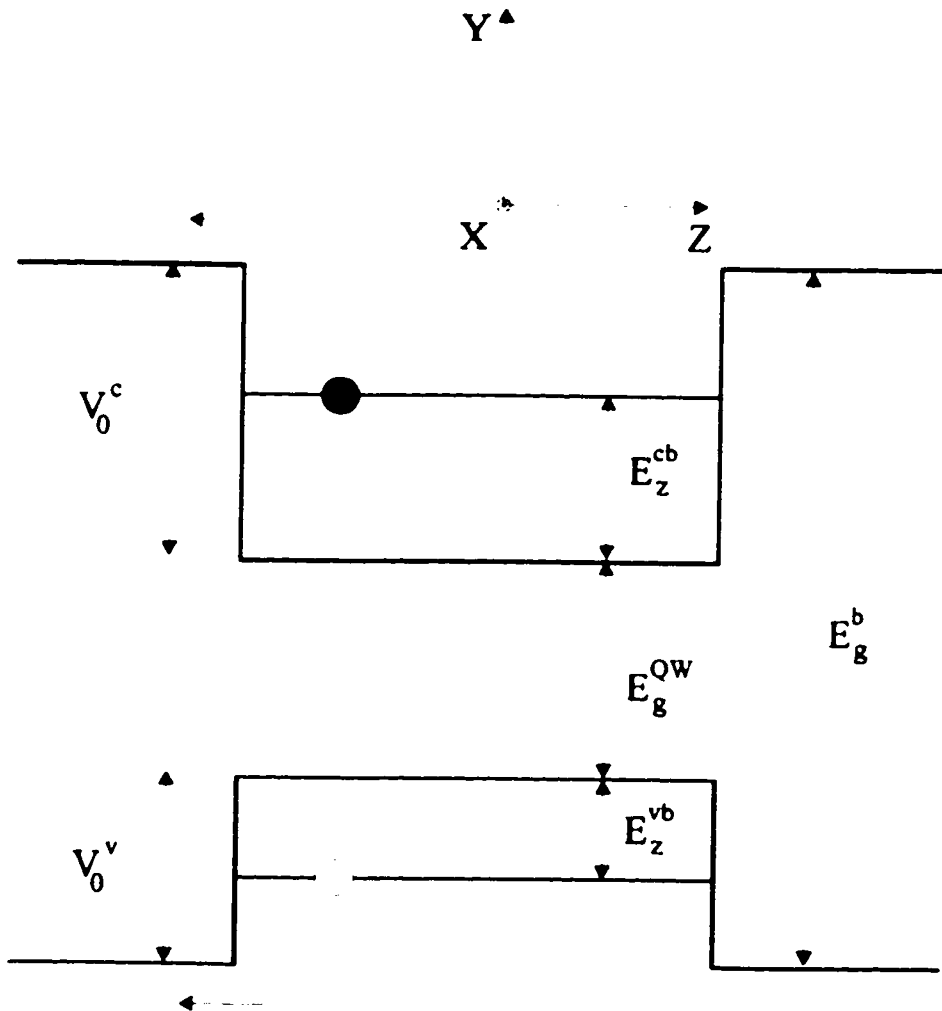

Figure II-10

Band profile for a quantum well with finite barriers. The carriers can escape the well region by thermionic emission.

where V_0 is finite and the effective mass is now z-dependent because the well and barrier effective masses are in principle not the same. Since the energy step is now finite, the carriers can penetrate the barrier and boundary conditions II-3a are no longer valid. The Ben Daniel-duke model[53] provides a new set of boundary conditions for finite band discontinuities. The functions

$$\Psi_z(z) \quad and \quad \frac{1}{m^*(z)} \frac{d\Psi_z(z)}{dz} \qquad \text{II-44}$$

are continuous at the interfaces. Using these conditions the envelope function in the z direction as well as the bound state energies can be calculated. It is not possible to obtain an explicit expression for the bound state energy as a function of l, the well thickness. However, an explicit expression for $l(E_{nz})$ is reported in the literature[54]

$$l = \frac{2\hbar}{\sqrt{m_w^* E_z}} \left[arctan\left\{ (-1)^{(n_z+1)} \left(\sqrt{\frac{m_w^*}{m_b^*}\left(\frac{V_0}{E_z} - 1\right)} \right)^{(-1)^{(n_z+1)}} \right\} + \pi * int\left(\frac{n_z}{2}\right) \right] \qquad \text{II-45}$$

where m_w^* and m_b^* are the effective mass of the carrier in the well and barrier material respectively, V_0 is the band discontinuity and n_z is the subband index. Equation II-45 applies to both the conduction and valence band provided the corresponding effective masses and band discontinuities are used. This result can be used to improve the method presented in section II.2. Expression II-45 is used to calculate $E_{QW}(l(\rho))$ and $V(\rho) = E_{QW}(l(\rho)) - E_{QW}(l_0)$ for several values of ρ. The numerical form of the lateral potential thus obtained can be fitted to a harmonic function or solved numerically. This method will be used in chapter V to model sample IR.

A second consequence of finite band discontinuities is that carriers can now escape the confined region by thermionic emission. The number of carriers in the bound state can be seen to result from a competition between a capture and an emission rate. As the temperature is raised, creating a dense phonon population in the lattice, the probability per unit time for a carrier to absorb phonons and be emitted above the barrier is greatly enhanced. As a result, the intensity of emitted light is quenched for higher temperatures according to an exponential law of the form

$$I(T) = \frac{c}{1 + \alpha e^{-E_A / k_B T}} \qquad \text{II-46}$$

where c and α are adjustable parameters, E_A is the activation energy and $k_B T$ is the thermal energy. The activation energy corresponds to the minimal energy necessary to promote carriers to unbound energy levels. In the case of electrons in the well of Figure II-10, $E_A = V_0^c - E_z^{cb}$. The onset to observe significant thermionic emission depends on both α and E_A. The process of thermionic emission is represented in Figure II-10 for an electron in the conduction band and a hole in the valence band where the arrows symbolize the emission above the barrier.

II.6 Concluding remarks

In the first section of this chapter the density of states for structures of different dimensionalities was introduced. It was found that the DOS evolves from a smooth

function in 3D to a completely discretized function in 0D. The effect of this evolution on experimental results was discussed; in a quantum dot, the absence of an energy continuum implies that the PL emission line is not broadened by an increase in temperature or excitation power. This is in contrast with the case of a 1D, 2D or 3D structure. Also, saturation effects such as populating excited states occurs for lower carrier densities in a quantum well layer compared to a quantum dot layer.

In the second section, the ideal lens-shaped island was modeled using the adiabatic approximation. In the strong confinement limit (Coulomb interaction negligible), the lower energy states were described as quantum well states in the z direction and harmonic states in the x and y directions.

Next, the energy spectrum of the islands subject to a magnetic field perpendicular to the plane of the islands was obtained. It was found that the field partially lifts the degeneracy of the higher energy shells, with a high proportion of states shifting towards lower energies. This is not typical of what is observed in quantum wells for which the electronic states shift towards higher energies under application of a perpendicular field. This difference of magneto-properties between quantum wells and lens-shape dots provide an alternate way of revealing the 0D nature of the bound states in a specific type of quantum dots.

In view of the wide use of optical experiments in this work, the radiative selection rules were discussed in section 4. In the hard wall approximation for lens-shaped dots, the selection rules obtained from Fermi's golden rule imply that radiative transitions are observed only between valence band and conduction band states with the same set of

quantum numbers. Also, phonon-assisted transitions and Auger transitions were introduced in view of later discussions on carrier dynamics. The concept of phonon bottleneck was introduced in that context.

Finally, the quantum well with finite barriers was introduced. Two main consequences were mentioned: 1- the bound state energies have to be calculated with a different formula than in the infinite barrier case 2- thermionic emission out of the well region is now possible.

III Experimental methods

In this chapter the optical probing techniques used to characterize our samples are presented. Photoluminescence, time-resolved photoluminescence and up-conversion measurements are discussed. The characteristics of the different set-ups are discussed.

III.1 Photoluminescence

According to the selection rules presented in the previous chapter, if an electron is present in the conduction band it can recombine radiatively with a hole state in the valence band. If enough recombination events occur in a given layer, important information is obtained by mapping the luminescence intensity as a function of energy (or wavelength). This spectroscopic experiment is referred to as photoluminescence if the carriers are initially promoted to the conduction band using a light source.

Figure III-1 shows a schematic of a modern photoluminescence set-up. Under the perturbation caused by the impinging light beam (usually a laser), the sample produces luminescence that is collected and steered to the entrance slits of a spectrometer. The light spectrum is then dispersed by a grating and each wavelength is subsequently focused onto a different position on the detector surface. If the detector is position-sensitive, a spectrum

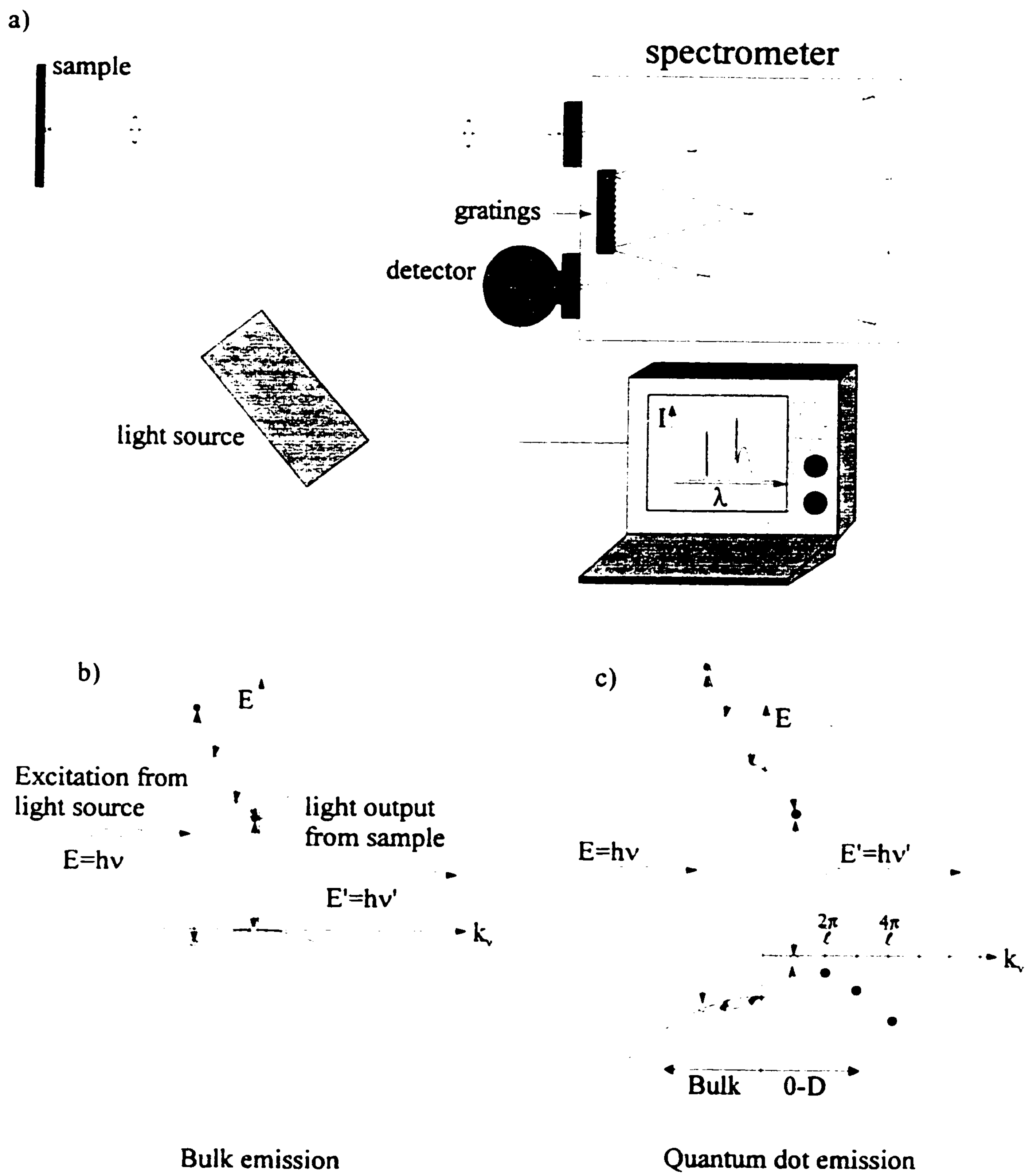

Figure III-1

Standard far field photoluminescence experiment. Figure a) shows a representation of all the components involved in a modern set-up. Part b) and c) show the sample reaction under the action of the excitation source for a bulk and a quantum dot respectively.

is acquired in parallel by simply feeding the intensity detected as a function of position to a computer. If the detector is position-insensitive, an exit slit is used to select a narrow wavelength range. The intensity of emission at this wavelength is measured and fed to the computer. The gratings of the spectrometer are then rotated to select a new wavelength and the process is repeated until the desired spectrum is obtained. The latter type of PL experiments will be called scanning spectrometer PL, as opposed to parallel detection PL obtained with position-sensitive detectors.

Figure III-1b shows, in k-space, the chain of events triggered by the absorption of a photon in a bulk structure. First, an electron is "vertically" promoted to the conduction band at the instant of absorption. If the energy of the photons absorbed is higher than the bandgap, the electron and hole are created with some excess kinetic energy. The carriers will thermalize to the band edge[55] by optical phonon emission and subsequently recombine radiatively to emit a photon of lower energy. The obtained spectrum would show an emission line at an energy roughly equal to the bandgap with a full width at half maximum strongly dependent on temperature and excitation intensity because of the continuous dispersion relationship.

For a quantum dot sample, several different excitation schemes are possible. For non-resonant excitation the carriers are created in the barrier material, usually a bulk structure. While thermalization to the band edge occurs, the carriers diffuse near a quantum dot; at this point they must relax from a continuum to the discrete states of the quantum dot. As discussed previously, in this case phonon relaxation could be slowed down due to the phonon bottleneck effect. Figure III-1c shows, in k-space, the chain of

events produced by non-resonant excitation in a quantum dot sample. For resonant excitation, the situation is similar except the laser energy is set to be in resonance with an excited quantum dot transition. Irrespective of the excitation scheme used, in the case of quantum dots, the luminescence resulting from transitions between discrete energy states should have an extremely narrow linewidth.

Also, it is often difficult to probe a single quantum dot in a luminescence experiment. For example, consider the case of the strained layer in sample VI with an island areal density of 200 μm^{-2}. The impinging laser beam is focused to a circular spot on the sample surface with typical diameter of 50 μm, thus probing a population of $\sim 10^6$ islands. Assuming the DOS inside each island is δ-function like, the resulting spectrum can still have a significant linewidth if each dot emits at a different energy due to inhomogeneous broadening factors such as size/composition fluctuations or different strain distributions. The homogeneous linewidth is revealed if one probes a small number of quantum dots such that their emission energy is well separated. For this thesis, photoluminescence experiments probing a large number of quantum dots are referred to as macro-photoluminescence (macro-PL), while those probing a small ensemble of quantum dots are referred to as micro-photoluminescence (micro-PL).

As an example of such photoluminescence experiments on quantum dot ensembles, Figure III-2 presents the spectra obtained when probing a self-assembled island sample with structural properties similar to those of sample VI. The macro-PL spectrum obtained when exciting the sample with a high power density of 300 W/cm^2 over a large surface area of 2×10^3 μm^2 is shown on the left hand side. Two peaks are observed in the

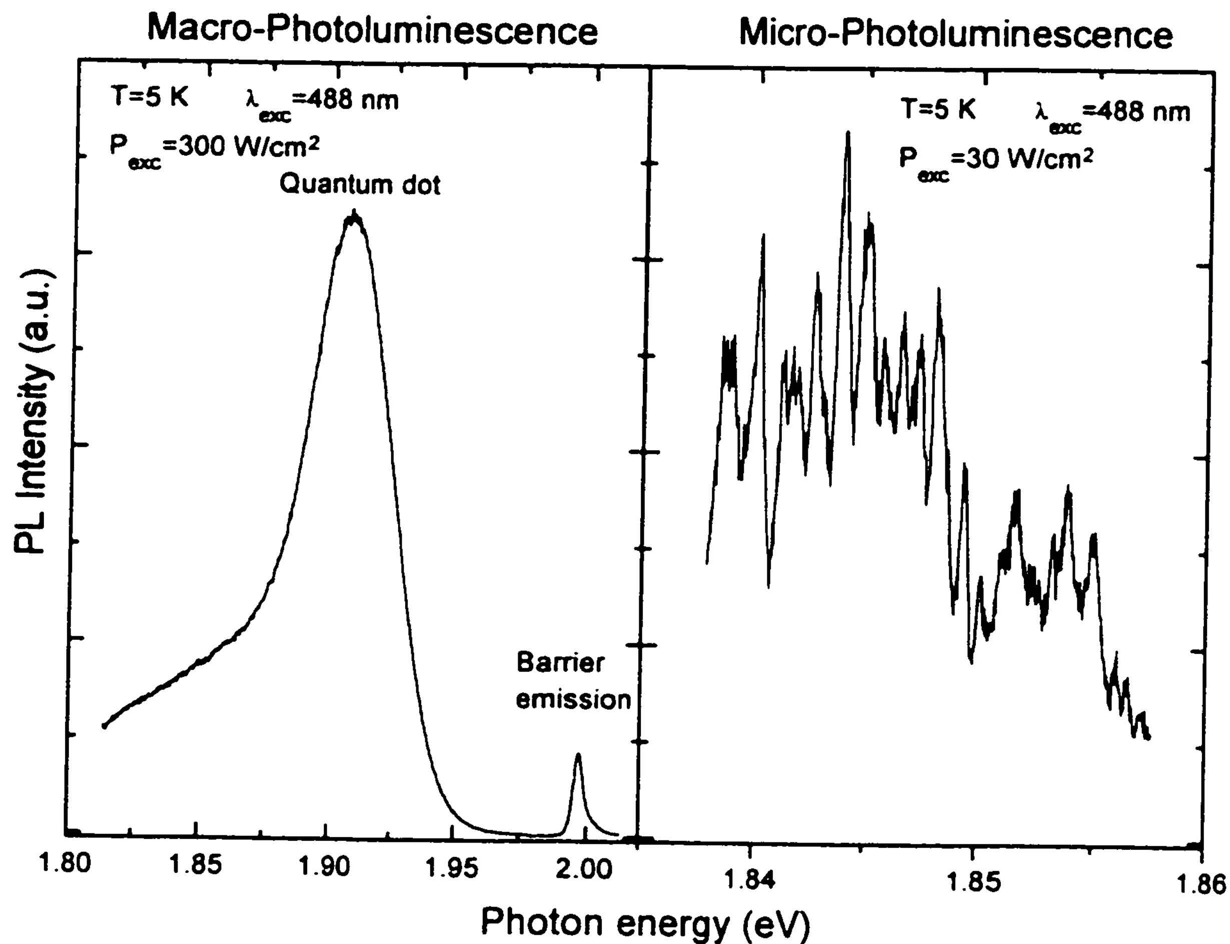

Figure III-2

Example of photoluminescence spectrum obtained from a self-assembled island sample. a) High excitation PL spectrum obtained when probing an area of about 5×10^3 μm^2; we refer to those experiments as macro-PL. b) PL spectrum obtained after depositing a thin gold film with small 3 μm^2 transparent windows on the surface; such experiments are referred to as micro-PL. The difference between the two spectra is interpreted as a change in the size of the quantum dot population probed.

spectrum. The smaller narrower emission line at ~2.0 eV is ascribed to light emission originating from the AlGaAs barrier since its energy closely corresponds to the bandgap of that material. Therefore, the broader emision band at ~1.91 eV is ascribed to emission from the strained AlInAs layer. This lower energy line is broader than the bulk emission from the AlGaAs and the δ-like density of states is not revealed by this macro-PL

experiment.

To perform a micro-PL experiment on the sample, a thin gold film was deposited on the sample surface and small (~3 μm diameter) transparent windows were obtained by standard lift-off techniques of the gold layer. This reduces the number of islands probed to approximately $\sim 10^3$. The spectrum obtained from this experiment is presented on the right hand side of Figure III-2. A series of ultra-narrow emission lines is obtained revealing the intrinsic homogeneous emission linewidth (~300μeV) of individual islands. In view of this the broad emission band of the macro-PL experiment is interpreted as the convolution of inhomogeneously broadened quantum dots emitting at different energies because of size fluctuations, composition fluctuations, strain distribution fluctuations, etc. This population-size dependence of the PL emission spectrum was one of the first evidence of the zero-dimensional nature of self-assembled islands reported in the literature[56].

In the next sections, two distinct and complementary PL set-ups are described. Each of these is associated with a particular time-sensitive optical measurement technique, namely time-correlated single photon counting and up-conversion, which will be described along with the experimental apparatus.

III.2 Imaging tube set-up and time-correlated single photon counting

The originality of this first system, presented in Figure III-3, resides in the fact that the traditional photomultiplier tube (used for single photon counting) has been replaced by an imaging photomultiplier tube (IPMT)[57] which can resolve the position of a photon

hitting its surface to within 60 μm both in the x and y directions. The detector can be used in several different modes. For example, in the first mode a PL spectrum can be acquired in parallel by integrating all the photons within the same vertical (y) slot. Knowing that the detector has a one inch radius optically active surface and that the light is being dispersed by a 0.75 m focal length double spectrometer with 1200 grooves/mm gratings, the wavelength range detected across the surface is calculated to be 12.2 nm. The spectral resolution of our set-up is then given by (12.2 nm X 60 μm / 1.0 inches =) 0.0305 nm which translates into an energy resolution of about 100 μeV at a wavelength of 600 nm. The multi alkali photocathode is sensitive in the range 400-900 nm. This set-up in the PL mode was used to obtain the spectrum of Figure III-2. The laser system used for PL experiments consists of a CW Ar^+-ion laser pumping a coherent c-599 dye laser with DCM dye emitting continuously in the range 610-690 nm. In the case of Figure III-2, only the argon laser was used.

In the second mode, the IPMT is used to obtain a time-dependence of the emission intensity. This type of experiment is called time-correlated single photon counting, commonly referred to as time-resolved photoluminescence (TRPL). In Figure III-3, the two-stage excitation source consists of a YAG pulsed laser emitting 100 ps pulses at 532 nm used to pump a coherent dye laser model 790 used with a rhodamine 640 dye which provides output pulses tunable between 620-690 nm of typically 10 ps duration at a repetition rate of 4 MHz[58]. In the experiment, a small fraction of the light pulse train is sent to an avalanche photodiode (APD) and acts as a trigger for a time to amplitude converter (TAC). The remainder of the pulse train is sent on the sample as the excitation

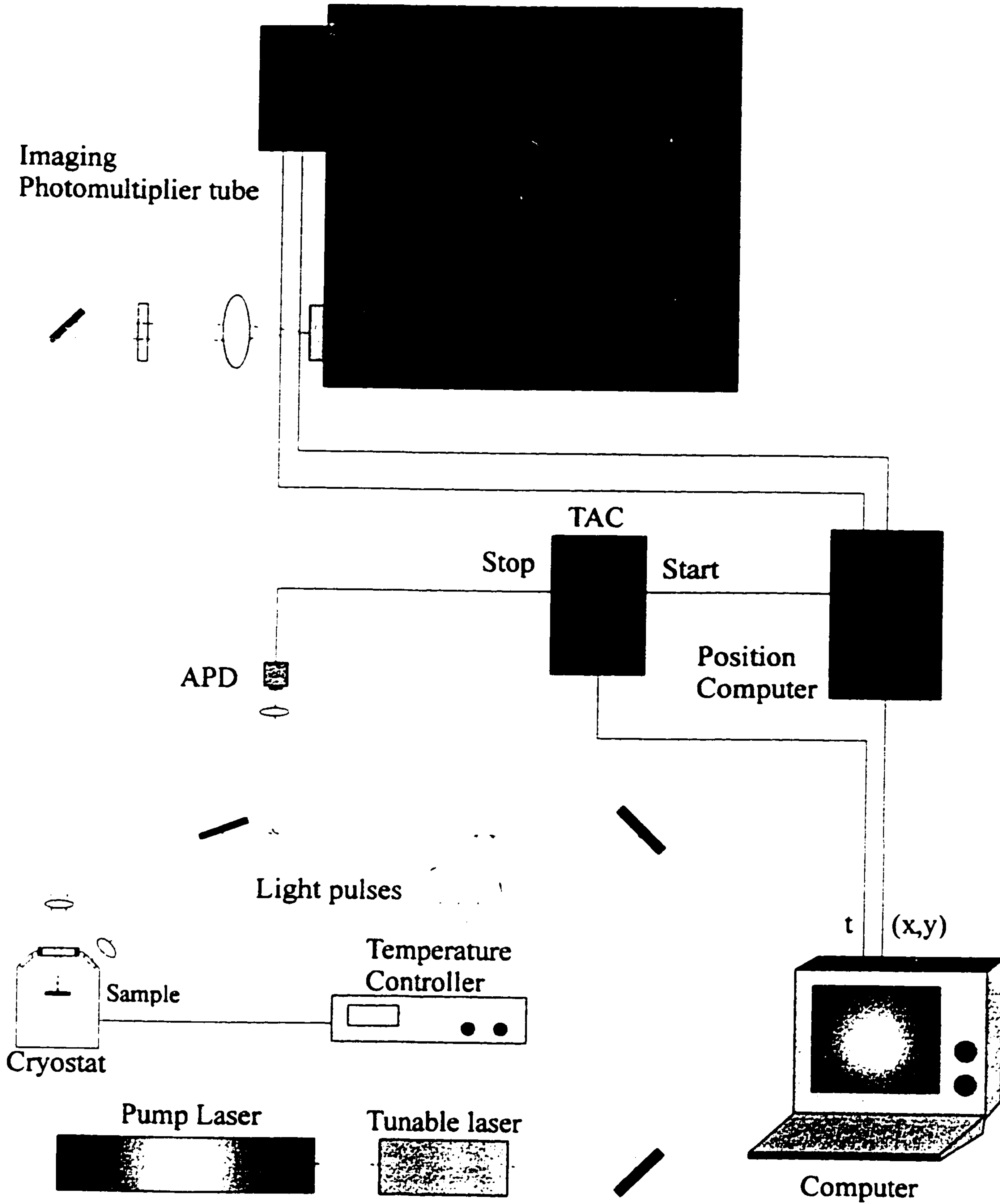

Figure III-3

Actual set-up used for photoluminescence and time-resolved photoluminescence.

source. A low temperature cryostat combined with a heater and temperature controller are used to keep the sample at a stable temperature between 4.2 and 300 K. Each time a pulse hits the sample, a time varying light output will be produced and part of it will be collected and steered into a double spectrometer. The first photon detected by the IPMT triggers the TAC to start counting and the next laser pulse that hits the APD stops the counting. The time difference is sent to the computer which will then add one count in the corresponding time slot. Repeating this process until satisfying statistics have been obtained allows us to build a time-dependent spectrum mapping the reaction of the sample with a typical temporal resolution of the order of 100 ps.

Finally, an important capability of the TRPL system with an IPMT is that the signal can be electronically gated. The analog output signal of the IPMT containing the x and y positions is processed by a position computer which allows the user to electronically gate the signal. Any rectangular surface of the detection cathode can be selected as being the active region, ignoring any event occurring outside the selected area. To illustrate the use of this gating technique, consider the spectrum of Figure III-2 where two distinct emission bands are detected at 1.91 and 2.0 eV respectively. To isolate the properties of the quantum dot band for example, the detector is gated around the region where the photons of this emission line hit the surface of the detector.

III.3 Up-Conversion

The two most severe restrictions of the TRPL set-up described above are its time

response and its spectral range. It is not possible to study samples that emit outside the range of 400-900 nm, nor is it possible to probe phenomena with timescales shorter than about 100 ps. For applications on the picosecond timescale or in the infra-red range, an up-conversion set-up is used, schematically shown in Figure III-4.

The sample is kept at a constant temperature between 4.2 and 300 K in a He-flow cryostat with a heater and a temperature controller. Any of the laser sources available can be used as an excitation source, depending on the particular experiment performed.

For up-conversion experiments, the laser output is split in two branches, one of which is directed to the sample, the other one being sent through a delay stage. As a reaction to the impinging light pulses, the sample emits time-varying luminescence. This light is collected and focused onto a nonlinear crystal, in this case made of Lithium Iodate ($LiIO_3$), spatially overlapping the laser light pulses coming from the delay stage. The $LiIO_3$ is placed on a rotating plate so as to satisfy phase-matching conditions. If the two beams have no temporal overlap the light output of the crystal will simply be at wavelengths given by λ_{laser} and λ_{sample}, the laser and sample PL wavelength. However, if there is a temporal overlap between the two pulses, the crystal will also show a light output at a wavelength given by the sum of the frequency of the two input beams. In other words the two photons interacting in the non-linear crystal are up-converted to produce higher energy output photon. The relationship between the input and output wavelengths is given by

$$\frac{1}{\lambda_{out}} = \frac{1}{\lambda_{laser}} + \frac{1}{\lambda_{sample}} \qquad \text{III-1.}$$

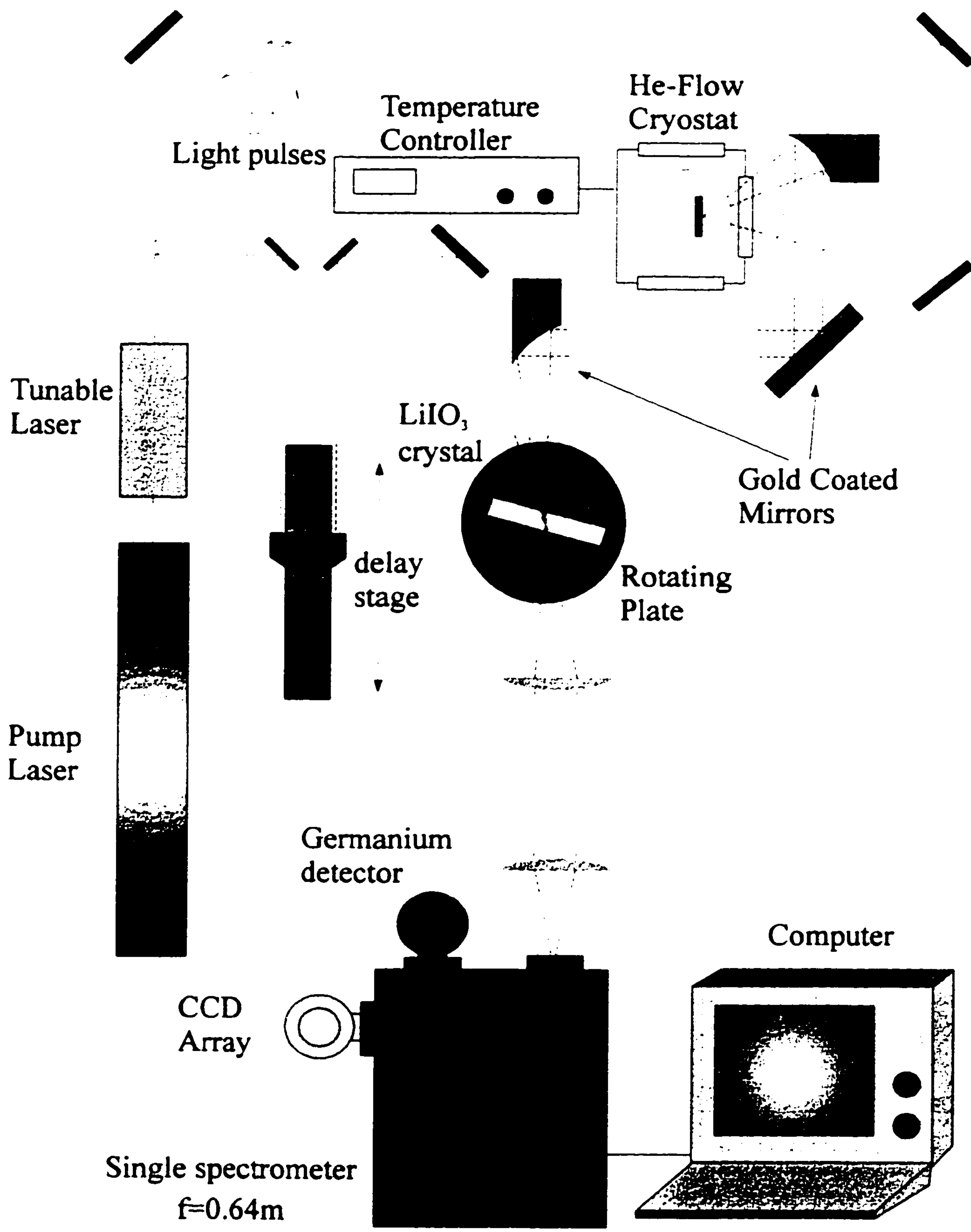

Figure III-4

Schematics of the set-up used for up-conversion experiments.

In actual experiments, the detection wavelength is set at λ_{out} so that a signal is obtained only when the laser pulse and the sample's luminescence overlap temporally on the $LiIO_3$ crystal. In other words, the laser pulse and the crystal act as a temporal gate for the luminescence coming from the sample. A signal proportional to the sample luminescence is transmitted only for a time window equivalent to the laser pulse. The delay stage is used to vary the time delay between the "gate" (laser pulse) and the sample luminescence. Thus, the intensity of the luminescence can be obtained for several different time windows. Figure III-5 presents an example of up-converted spectrum for a given time delay. The GaAs emission (~ 820 nm) of sample IR is focused on the crystal and overlapped with the laser emission at 641.1nm. The resulting PL ~366 nm is detected in parallel with the CCD array detector and a quasi-Gaussian lineshape with FWHM of ~2 nm is obtained. This linewidth depends on phase matching conditions[59] and corresponds to a 10 nm (~17 meV) bandwidth that is transmitted through the crystal. The area under the curve is proportional to the sample's luminescence at a corresponding time.

The CCD array can also be used to obtain CW PL spectra of samples in the 300-1000 nm range using a parallel detection scheme with a window range of 12.16 nm over 1024 pixels when using a 600 groves/mm grating. Assuming one cannot resolve a line sharper than 3 pixels this means the detector spectral resolution is of the order of 0.035 nm, which translates to an energy resolution of 122 μeV at 600 nm.

Finally, a liquid nitrogen cooled Ge detector incorporated in a scanning spectrometer acquisition scheme can be used to obtain CW PL spectra of samples emitting in the 800-1700 nm range. A spectral resolution of ~0.1 nm is obtained for 600 g/mm

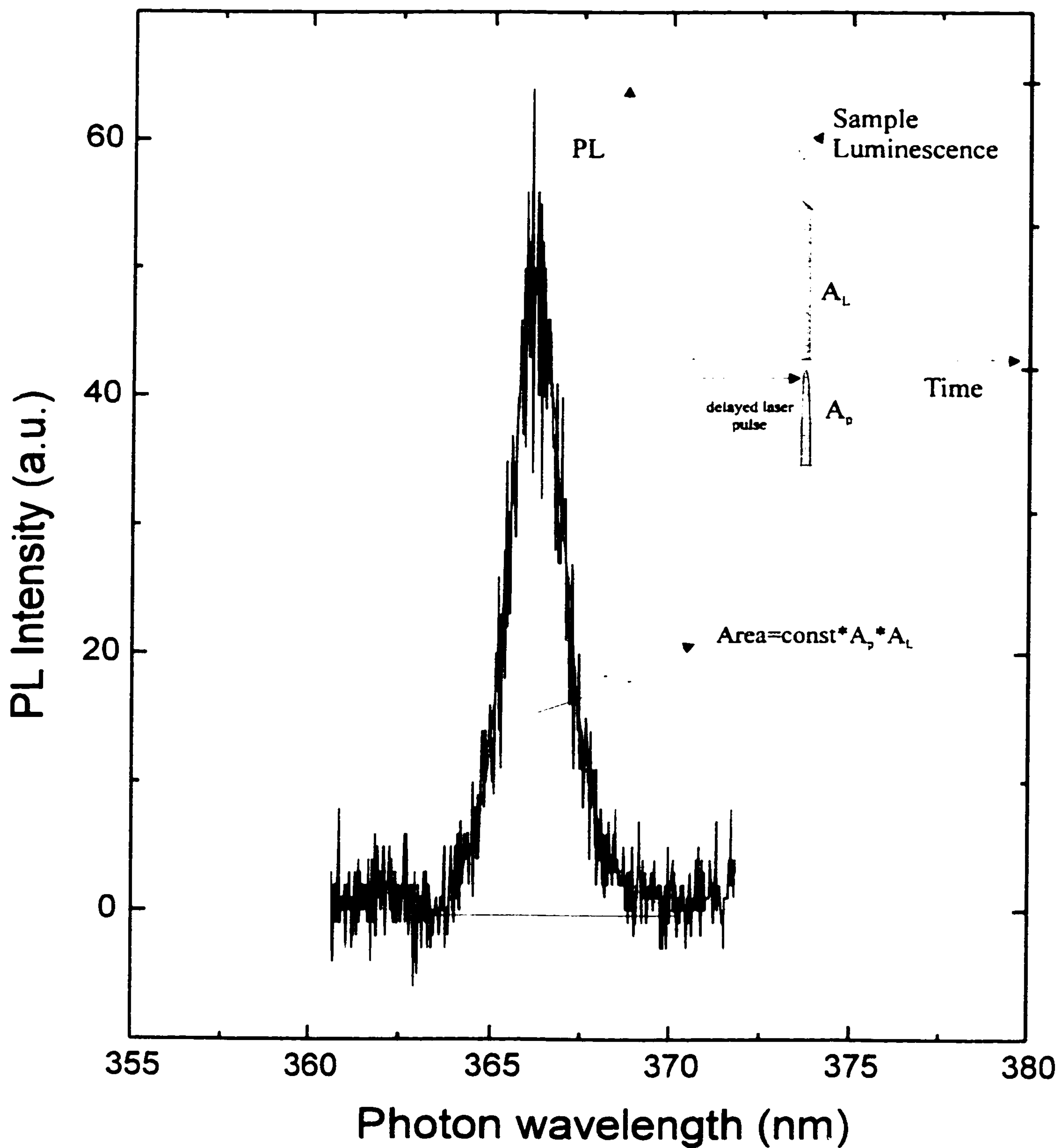

Figure III-5

Example of the up-converted spectrum obtained for a given time delay between the leading edge of the luminescence an the laser pulse. The area under the curve is proportional to the integrated luminescence intensity (gray shade in the inset) over the duration of the laser pulse.

gratings with entrance and exit slits open to 150 μm.

III.4 Rate-equation model

As an example of the type of spectrum one expects to obtain from the time-dependent measurements, let us consider the situation of Figure III-6 which depicts the carrier dynamics in a single quantum well. In what follows, the dynamics is discussed in terms of "rates" (γ), but is often discussed in terms of "lifetime" τ where $\gamma = \frac{1}{\tau}$.

The process starts when an electron-hole population is created in the barrier material which, after thermalization to the band edge, is captured in the quantum well. For simplicity, equal capture rates γ_c are assumed for the electrons and the holes. At this point, the carriers can recombine radiatively at a rate γ_r, or non-radiatively at a rate γ_{nr} (in the figure the non-radiative process is represented as thermionic emission). The electron-hole population in the well as a function of time is obtained by solving the following set of equations:

$$\begin{aligned} \frac{dN_b}{dt} &= -\gamma_c N_b \\ \frac{dN_w}{dt} &= +\gamma_c N_b - \gamma_r N_w - \gamma_{nr} N_w \end{aligned} \qquad \text{III-2}$$

where N_b and N_w are respectively the barrier and well electron-hole population. Assuming $N_b(0) = N_0$ and $N_w(0) = 0$, the solution is given by

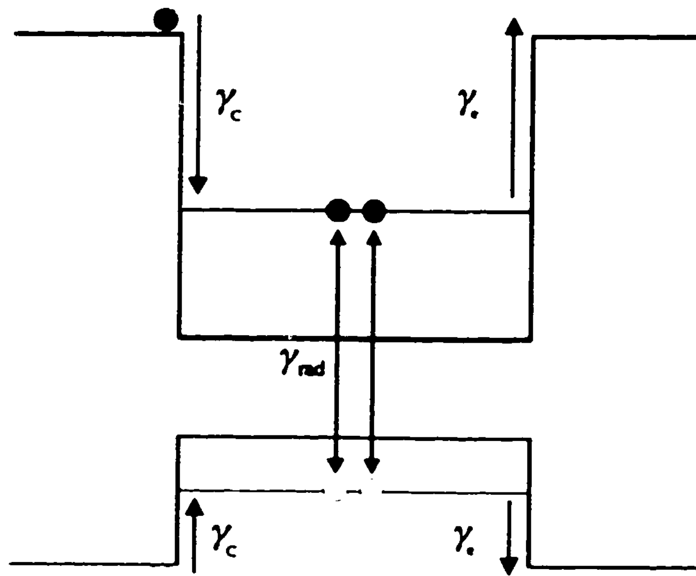

Figure III-6

Example of carrier dynamics for a one-dimensional quantum well. Only the carriers which recombine radiatively are detected.

$$N_b = N_0 e^{-\gamma_c t}$$
$$N_w = \frac{N_0}{\left(1-\left(\frac{\gamma_r + \gamma_{nr}}{\gamma_c}\right)\right)}\left(e^{-(\gamma_r+\gamma_{nr})t} - e^{-\gamma_c t}\right) \qquad \text{III-3}$$

and the intensity of emission as a function of time is simply given by $I = \gamma_r N_w$ which yields

$$I_w = \frac{\gamma_r N_0}{\left(1-\left(\frac{\gamma_r + \gamma_{nr}}{\gamma_c}\right)\right)}\left(e^{-(\gamma_r+\gamma_{nr})t} - e^{-\gamma_c t}\right) \qquad \text{III-4}$$

In many cases the capture rate is much faster than the decay rate and one obtains

$$I_w = \gamma_r N_0\left(e^{-(\gamma_r+\gamma_{nr})t}\right) \qquad \text{III-5.}$$

Thus, in most cases the time-dependent emission observed from TRPL or up-conversion

experiments shows a fast rise and a slower single-exponential decay. This is the situation represented in the inset of Figure III-5.

In general, the rise time is associated with the capture rate and the decay time is related to carrier lifetime in the level probed. However, care must be taken when assigning the decay time to the lifetime. Equation II-4 clearly shows that the lineshape is symmetric with the interchange of the total decay rate ($\gamma_r + \gamma_{nr}$) and the capture rate (γ_c). The faster and slower rates are therefore respectively associated with the rise time and the decay time of the luminescence intensity.

III.5 Summary

In this chapter, the three measurement techniques used to probe the self-assembled islands were introduced. First, photoluminescence experiments were discussed and a distinction between different types of photoluminescence was made. Macro-PL experiments were shown to be a useful tool to probe the inhomogeneous properties of large ensembles of quantum dots. On the other hand, Micro-PL experiments probing a small number of quantum dots revealed the homogeneous properties of "single" quantum dots.

Two distinct set-ups were then introduced, each associated with a specific type of time-dependent experiment, on top of their steady state PL capabilities.

Time-correlated single photon counting set-up is implemented using an imaging tube (IPMT) which possesses the useful feature of electronic signal gating. The detector is

sensitive in the 400-900 nm range. PL spectra can be accumulated using a parallel accumulation scheme with a total range of 12.2 nm and a resolution of 0.03 nm. Finally, time-resolved spectra can be obtained with a time resolution of ~100 ps.

The up-conversion set-up is complementary to the IPMT set-up. Better time resolution is obtained (10 ps) at the expense of dynamic range. Also, PL can be performed in the infra-red range (800-1700 nm) using a Ge detector while a state-of-the-art CCD array detector is available for visible and near-visible (300-1000 nm) applications.

Finally, the case of a single quantum well with one bound state is considered to introduce rate equation modelling. Single exponential decay of the luminescence intensity with time is obtained.

IV Properties of AlInAs/AlGaAs Islands

In previous chapters, care was taken to avoid labeling self-assembled islands as quantum dots, even though the calculations of chapter II and the results of chapter III suggest that such could be the case. In this chapter, optical measurement techniques are used to characterize the islands and show that their properties are really those of quantum dots. To this effect, micro-PL experiments are used to monitor the properties of "single" dot emission: FWHM as a function of temperature, lifetime as a function of temperature and FWHM as a function of excitation intensity. Finally, carrier dynamics in semiconductor self-assembled quantum dots is studied, emphasizing the role of phonons in the relaxation process.

IV.1 Intrinsic linewidth and related properties

Macro-PL measurements performed on sample VI using a scanning spectrometer detection scheme are reported in the literature[60] and these results are reproduced in Figure IV-1. The laser was focused to a spot ~80 μm in diameter, and with an island areal density of 200 μm^{-2} this means that a total of $\sim 10^6$ islands were probed. The resulting spectrum shows three peaks at 1.887, 1.960 and 1.993 eV which are respectively attributed to island, wetting layer and barrier luminescence. The broad emission line at lower energy has

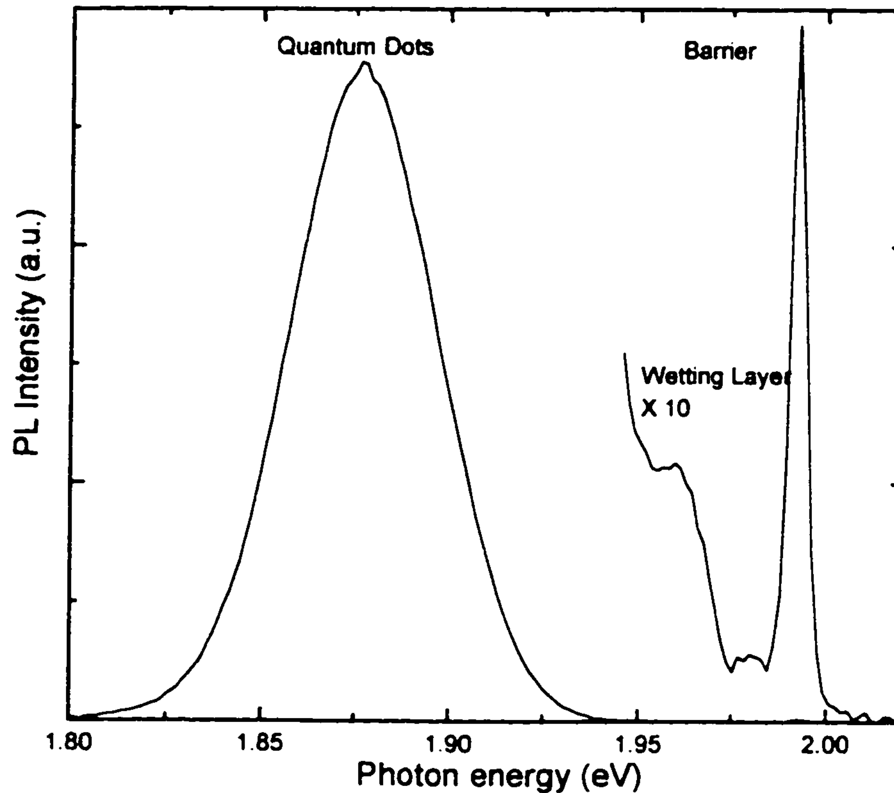

Figure IV-1

PL spectrum obtained for a macro-PL experiment on sample VI probing ~10^6 islands. The three peaks observed at 1.887, 1.96 and 1.993 eV are attributed to QD, WL and barrier emission respectively (after ref. 53).

a full width at half maximum of ~46 meV and its smooth shape has been shown to result from a convolution of a great number of inhomogeneously broadened emission lines coming from islands with slightly different size, strain and/or composition, much like the case presented in Figure III-2.

In order to confirm this assignment, micro-PL experiments are performed on sample VI to reveal the homogeneously broadened single dot emission line. In contrast with the window technique presented in chapter III, small island ensembles are obtained by defining a grid of small (~3 μm^2) mesas 100 μm apart on a section of the sample surface. Outside

the mesas, the material is deeply etched so that the self-assembled island layer is removed and consequently no PL signal originates from outside the mesas. As a result, even with a laser spot 80 μm in diameter one can probe a single mesa containing an average of ~600 islands.

Figure IV-2a shows the low-temperature PL spectrum obtained from one mesa at different temperatures with an excitation power of 25 W/cm^2 using the Ar^+-ion pumped DCM dye system, with the laser energy set at 1.96 eV. The spectrum exhibits several sharp spectral features of similar magnitude with a FWHM ranging from 190 to 400 μeV. Other mesas excited above the barrier material (E_{exc}=2.0 eV) with very low power densities (2.5 W/cm^2) have shown some spectral features as narrow as ~100 μeV. Most lines with typical FWHM of 250 μeV are resolved by the system, and as will be shown shortly, the carrier lifetime amounts to 400 ps for the island emission. Using the time-energy uncertainty relationship $\Delta E \Delta \tau \approx \hbar$ the linewidth is estimated as ~1.6 μeV. Thus, the experimental results are not transform-limited and other explanations have to be considered to account for the observed homogeneous linewidth.

The non-zero PL signal observed in between adjacent lines can be attributed in part to the finite intrinsic emission linewidth of each single QD which produces a collective emission background. It should be noted that the background signal left at high temperature in the regions of the spectrum where the sharp lines are quenched (see Figure IV-2d at ~1.892 eV) is stronger than the dark count signal of the system. The spectra b, c and d shown in Figure IV-2 have been shifted in energy to align the sharp lines at all temperatures using line C, which was clearly recognizable from spectrum to spectrum, as

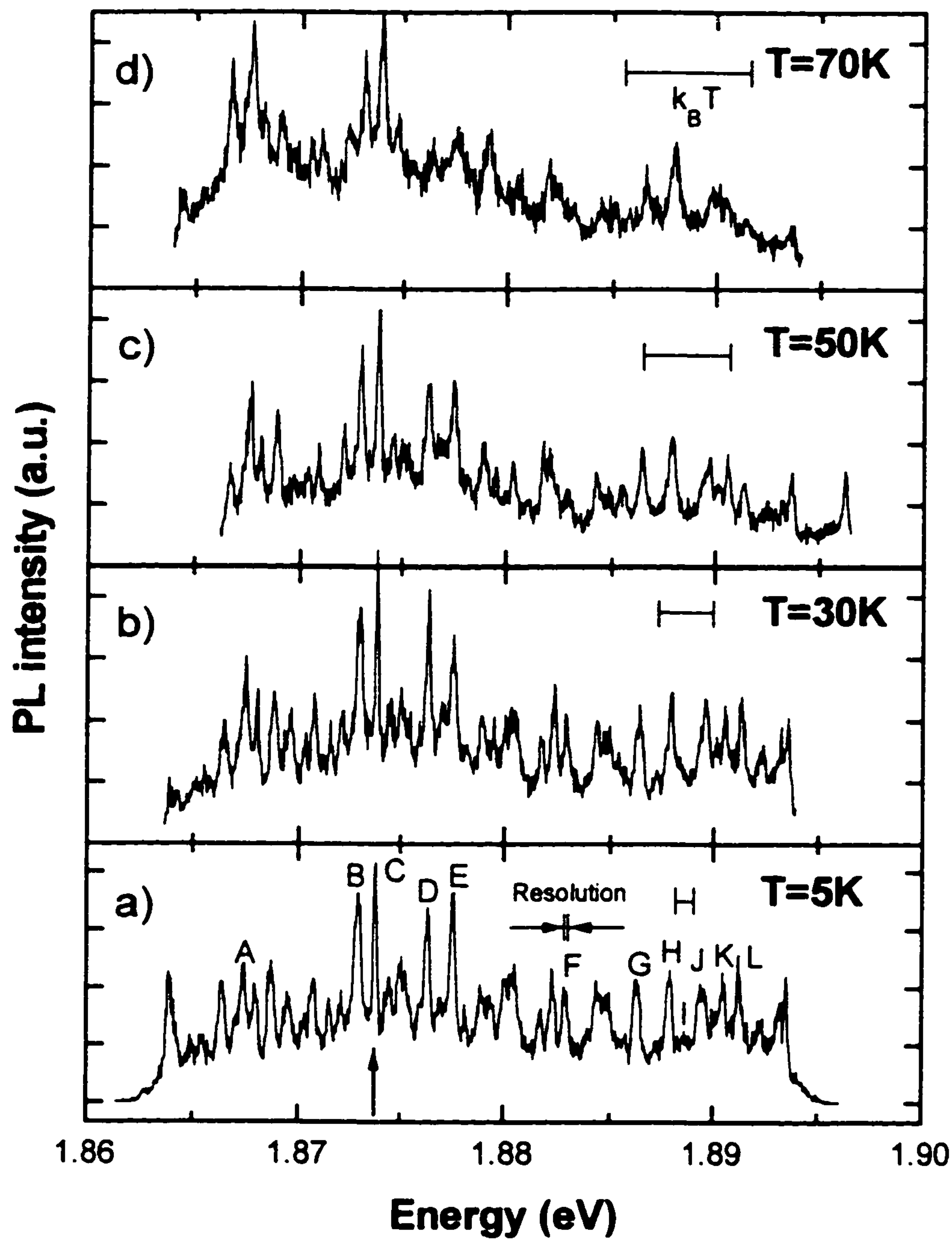

Figure IV-2

PL spectrum for a population of ~600 islands at different temperatures obtained with an excitation density of 25 W/cm^2. The energy scale is for the 5K spectrum. At higher temperatures the spectra were shifted to align the peak indicated by an arrow. The resolution of our set-up and the evolution of the thermal energy are also shown for comparison.

an alignment marker. It is a striking feature that these closely spaced sharp emission lines can be identified over a tenfold range in temperature. The sharp lines for which the intensity level remains well above the collective emission background show very little broadening as the temperature is increased up to 70K. Some lines, such as G, do show some broadening, although much less than the increase in the thermal energy (k_BT). This small effect can be attributed to the background noise in the experiment since at 70K the PL intensity has decreased by a factor of 10 due mostly to thermionic emission[61] and several lines are barely seen above the collective background emission. These temperature-independent linewidths are in contrast with the case of bulk, QW or QWR material where the 3D, 2D and 1D density of state permits a continuum of energy leading to thermal broadening of the emission line. For example, in a QW sample the theoretical band-to-band emission line has a FWHM of $\ln(2)*k_BT$[62], where k_B is the Boltzmann constant. Figure IV-3 shows a comparison of the measured FWHM of some of the lines in Figure IV-2 with the theoretical broadening of a quantum well sample as a function of temperature. The graph shows clearly that the island emission line broadening is negligible as a function of temperature, especially when compared to the expected broadening for a 2D layer emission line. Indeed, the physics is very different in both cases. Considering band-to-band emission for the case of a structure with at least one macroscopic dimension, there exist a continuum of states described by a wavenumber k and increasing the temperature causes higher k-states to be occupied. This means that one can now have electron-hole pairs with high internal energy while the net pair momentum remains zero, therefore allowing efficient radiative recombination of electron-hole pairs at higher

energies. On the other hand, for a zero-dimensional structure there is no continuum and as long as the thermal energy does not allow carriers to be excited to higher states one expects the linewidth to be constant.

Interpretation of the results of Figure IV-2 in terms of exciton emission in a 2D layer also has to be rejected. Assuming each individual line originates from the n=1 bound state of an exciton confined in regions of a well with different thickness would mean that there are as many regions as there are emission lines observed. Approximately 30 lines are clearly resolved in Figure IV-2, and this would imply a variation of the well thickness by as much as 30 MLs. This is unreasonable considering that ~15 monolayers of material were grown. Also, as mentioned in the section concerning selection rules, excitonic emission lines do broaden as a function of temperature and therefore an interpretation in terms of excitonic emission has to be rejected.

Finally, it should be noted that similar sharp spectral features as those observed in Figure IV-2 were unambiguously proved to originate from luminescence of a few (one to six) islands emitting at similar wavelengths[27]. Indeed, "gating" on the luminescence of a narrow emission line, only a few islands can be "seen" on the surface indicating strong localization of the carriers in the islands.

As discussed so-far, the temperature independent linewidths of the island's luminescence is a steady state manifestation of their 0D properties. Complementary information can be obtained by probing the transient properties of the islands. To do so, we take full advantage of the adaptability of our experimental set-up to isolate the properties of a single narrow emission line. Using the set-up of figure III-3 in PL mode

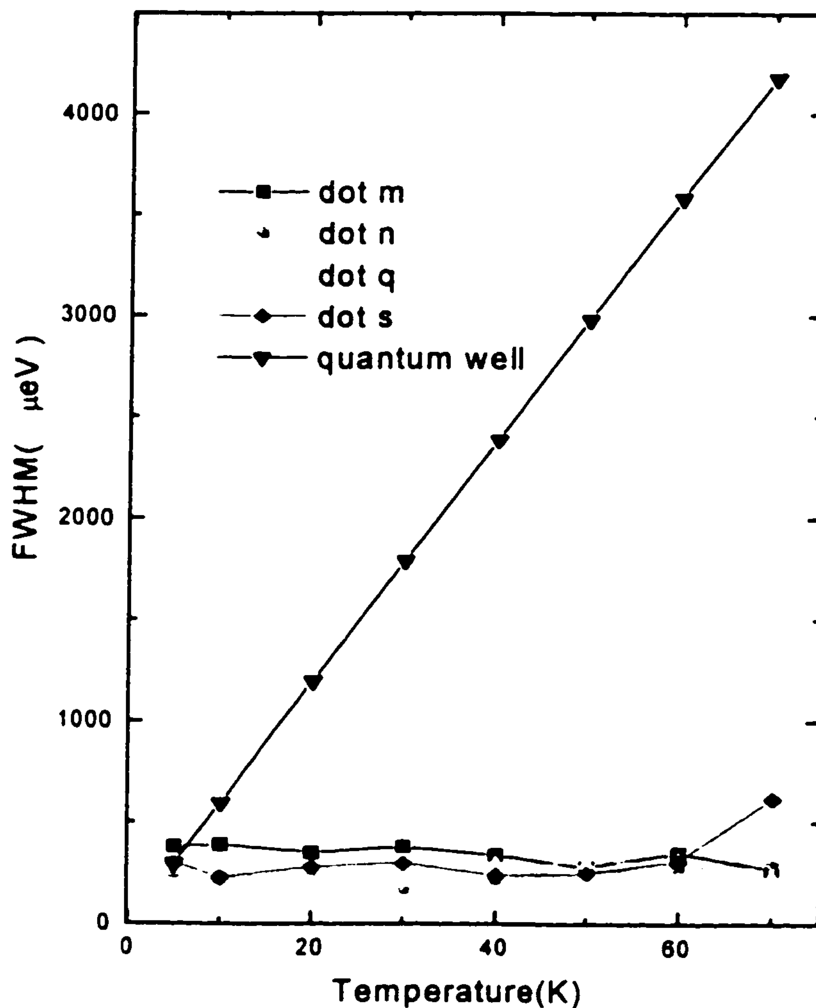

Figure IV-3

Comparison of the measured FWHM of some of the emission lines compared with the theoretical increase in FWHM for a quantum well sample.

with the pulsed dye laser system as the excitation source, a PL spectrum of the selected dot ensemble is first obtained and the result is shown in the inset of Figure IV-4. The laser energy was set at 1.993 eV for excitation in the AlGaAs barrier with an average excitation power density of 20 W/cm^2. The configuration is then changed to include the APD and the TAC in the set-up, allowing the system to probe the transient behavior of the sample. The

controls of the position computer are used to electronically reject all photon events outside a selected area on the detector surface. To probe the photons coming from a "single" quantum dot, we take advantage of the fact that each of them emits with slightly different energy: by gating around the surface of the detector which coincides with the emission energy of a given ultranarrow line, the properties of the corresponding "single" dot are probed.

The time decay traces obtained by gating around the peak indicated in the topmost inset at different temperatures are shown in Figure IV-4. As mentioned in chapter III, this decay time can be interpreted as a carrier lifetime or a capture time, depending on which is the slowest. The integrated barrier and wetting layer luminescence is shown to be much weaker than the dot luminescence in Figure IV-1, which suggests a short capture time. Therefore, for all discussion concerning sample VI, the rise times and decay times are interpreted respectively as the capture time and the lifetime.

The decay traces of Figure IV-4 are single-exponential over at least two order of magnitudes, and the observed decay times obtained by a single-exponential fit are summarized in the bottom left inset. The lifetime remains constant to within experimental uncertainty at around 400 ps for temperatures ranging from 4 K to 40 K, while at 60 K this time shortens to 340 ps. This last temperature correlates well with the onset of thermionic emission observed from CWPL experiments reported in the literature[61]. In this case, the carriers in the dot are lost via radiative recombination at a rate γ_r and via thermionic emission at a rate γ_e. At low temperatures, the emission rate is negligible and the decay reflects the radiative lifetime. As the temperature is raised, γ_e increases and

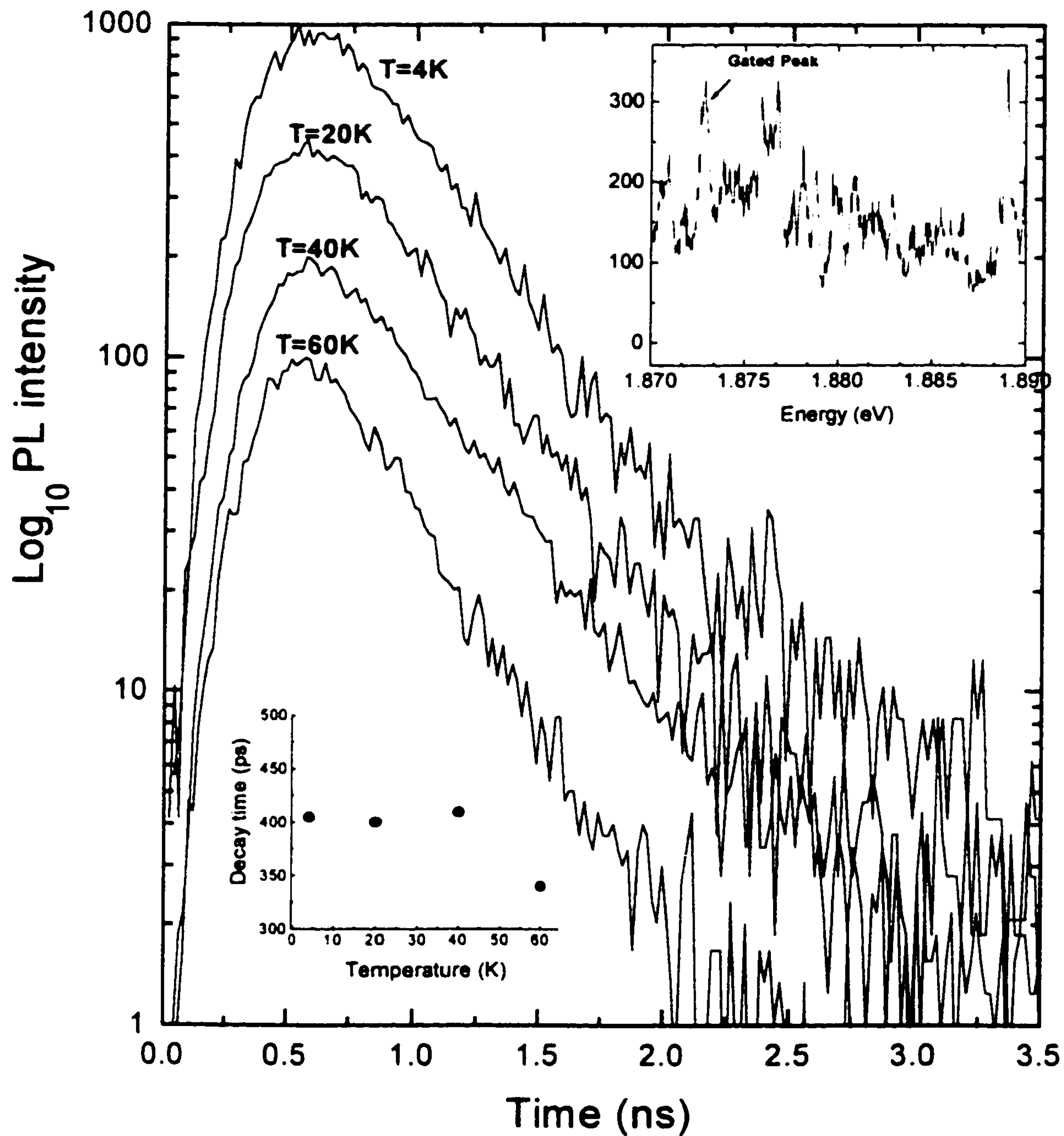

Figure IV-4

Time decay traces for a single sharp line at different temperatures. The curves have been y-shifted for clarity. The inset shows the peak used for the measurements, and the error on the lifetimes is of the order of 10 ps.

eventually contributes significantly to the total decay rate, and the signal is quenched faster. The speed-up of the carrier lifetime is therefore attributed to significant thermionic emission from the dot ground state to the WL or barrier states followed by other decay mechanisms.

In the literature, temperature dependent measurements on higher dimensionality (non 0D) systems are reported to show increasing lifetimes with increasing temperature. This effect was attributed to the higher proportion of excitons that are thermally excited to high center-of-mass momentum[10] states for which radiative recombination is prohibited according to the selection rules (see chapter II). Thus, the result obtained here can again be interpreted in terms of a set of discrete energy levels for which the radiation properties remain unchanged as long as no thermionic emission to higher energy states is possible. This interpretation is consistent with calculations done for quantum dots with large level spacing[63] for which thermionic emission can be neglected.

IV.2 Carrier dynamics: influence of phonons

In the previous section, clear evidence of the 0D nature of the bound states in self-assembled island was presented. This section will focus on the transient properties of quantum dots, more specifically addressing issues related to the influence of phonons.

In a previous study, Fafard *et al.* observed strong resonances in the PL spectrum of dot ensembles when resonant excitation was used[64]. These results are reproduced here in Figure IV-5a for clarity of the discussion. The dashed curve displays the steady-state PL

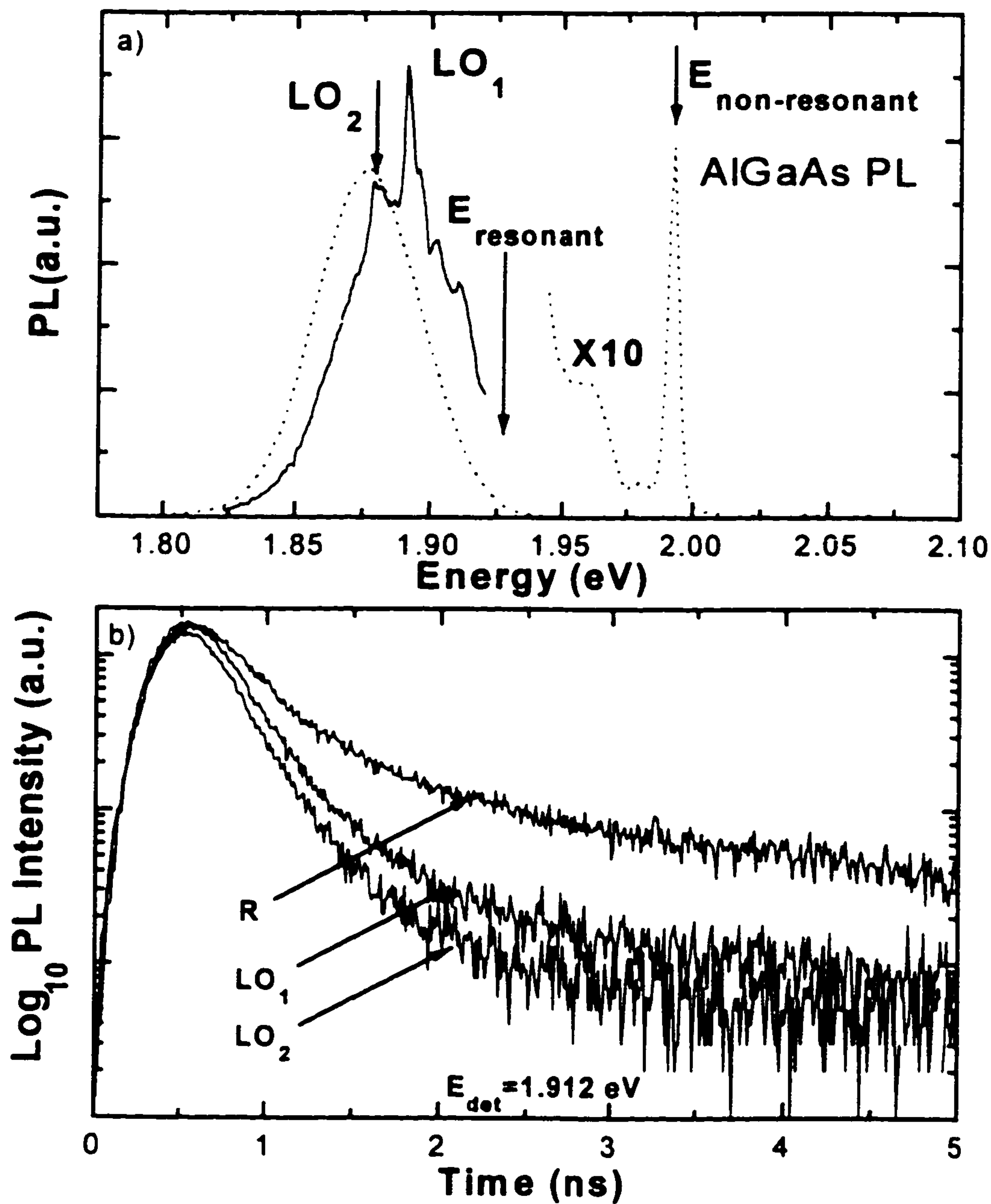

Figure IV-5

a) Low-temperature PL spectrum obtained for a dot population of ~10^6. The dotted curve is obtained using an excitation energy above the barrier material, and the solid line is obtained for resonant excitation. The peaks observed in resonant excitation are associated with phonon resonances, and for example the peaks labeled LO_1 and LO_2 are observed 35 meV (GaAs-like LO phonon) and 48 meV (AlAs-like LO phonon) below the excitation energy. b) Time decay trace of the quantum dot emission for E_{det}=1.912 eV. The decay traces "Nonresonant" (R), LO_1 and LO_2 are thus obtained for E_{exc}=1.993 eV, $E_{exc}=E_{det}$+35 meV and $E_{exc}=E_{det}$+48 meV.

spectrum obtained when exciting non-resonantly above the barrier material, where relaxation in the islands requires multi-phonon emission or other relaxation processes such as Auger scattering. The solid curve is obtained when the sample is excited resonantly on the high-energy side of the Gaussian dot peak at 1.927 eV. Peaks appear at fixed energies below the excitation line, corresponding to phonon modes in the dot and barrier materials. For example, the dominant peaks labeled LO_1 and LO_2 appear respectively 35 and 48 meV below the laser energy, and are associated with one GaAs and one AlAs-like longitudinal optical phonon in $Al_xGa_{1-x}As$[65]. Similar phonon signatures were observed in resonant TRPL spectra obtained with corrugated superlattices and were attributed to Raman scattering[66]. Here, however, the phonon signatures are observed for a wider spectral range than the exciting laser pulse, which identifies the peaks observed as being PL originating from dots excited with an excess of phonon energies. These results have triggered a new series of questions, more specifically related to the dynamics associated with the phonon resonances.

To this end, TRPL experiments are performed on sample VI. The spectra were obtained using the YAG pumped Rhodamine 640 dye laser system as the pulsed excitation source, and the detection energy was set by gating the detector on a narrow energy range (~1 meV) of the smooth Gaussian dot peak. The laser energy was then set one LO phonon energy above the detection energy to investigate the influence of the phonons on the carrier dynamics. A TRPL spectrum under non-resonant excitation conditions was also obtained for comparison. In all cases the excitation intensity was kept at 140 mW/cm^2, so that on average only 0.3 electron-hole pair per pulse per dot are created even if one

assumes that 100% of the laser energy is ultimately transformed into pairs captured in the zero-dimensional states of the islands. Figure IV-5b shows an example of the traces obtained for E_{det}=1.912 eV. The traces LO_1 (LO_2) are obtained for excitation energies one GaAs-like (AlAs-like) LO phonon energy higher than the detection energy, while the non-resonant trace is obtained with the excitation energy set at 1.993 eV (AlGaAs barrier).

We first observe that the decay times for the resonant excitation experiments have a longer time scale (200-300 ps) than the system temporal resolution (~100 ps). Raman-scattering phenomena, however, would appear to be instantaneous relative to the time scale involved here (i.e. instrumental response limited). This confirms the interpretation that the observed phonon resonances are not related to Raman scattering, and the most likely explanation is that the PL observed under resonant excitation comes from dots excited with an excess of one phonon energy. Furthermore, one notes that the non-resonant trace is in fact an experiment similar to the one presented in Figure IV-4, with the difference that we are now probing a few thousand dots as opposed to a few dots. A remarkable difference is observed between the two results since the decay traces of Figure IV-4 are single-exponential over two order of magnitude while the non-resonant trace of Figure IV-5b follows a single exponential decay over less than an order of magnitude. This effect will be discussed with the intensity dependent measurements presented at the end of this section.

For now, the dynamics and related relaxation processes are discussed in more details. For the nonresonant case, most carriers are created in the barrier layers, and will subsequently relax to the 0D QD ground state. Some of the possible relaxation processes

available are exemplified in Figure IV-6. After excitation in the barrier material, carriers can relax to the dot states via phonon emission, as shown on the left hand side of Figure IV-6. This can be achieved mainly in two different ways: multiple phonons can be simultaneously emitted to relax directly to the dot ground state, or alternatively, phonons can be emitted sequentially to relax to the wetting layer band edge, at which point multi-phonon emission is likely required to relax in the QD ground state (E_{wl}-E_{QD}~70 meV>$\hbar\omega_{LO}$). An alternative relaxation process is provided by Auger scattering, presented on the right hand side of Figure IV-6. Again, direct or sequential trapping is possible, depending on the types of collisions experienced by the carriers. However, it should be noted that the low excitation intensity used for the TRPL experiments reduces the possibility of carrier-carrier scattering.

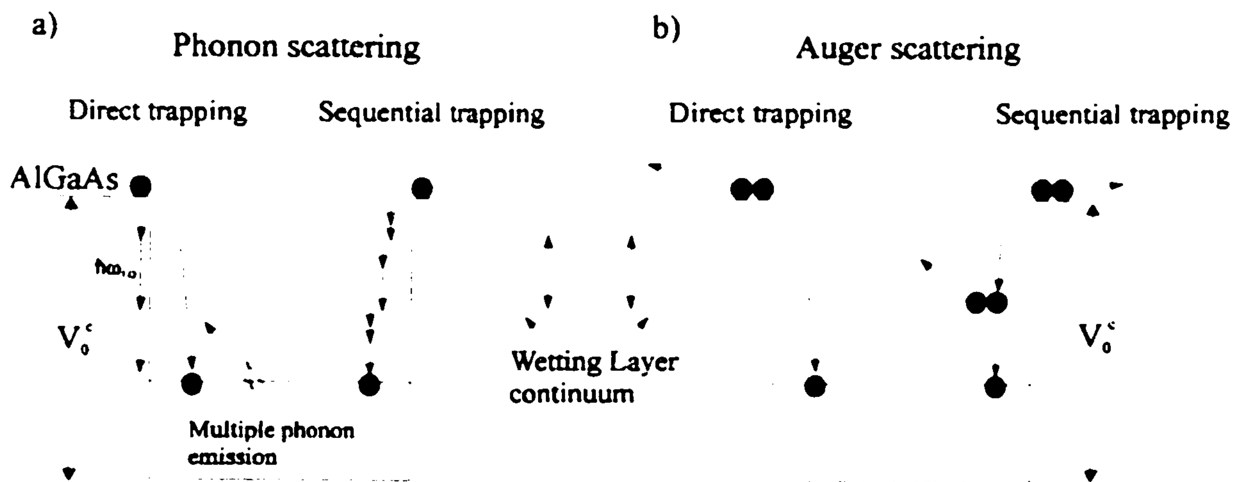

Figure IV-6

Representation of sequential and direct trapping for the phonon emission a) and Auger b) relaxation processes. a) In direct trapping, the carrier emits several phonons simultaneously in order to relax directly from the barrier to the dot ground state. For sequential trapping, the carrier emits a small number of phonons (one or two) to relax in a wetting layer state. The same process is repeated to relax to the WL band edge, and finally relaxation to the dot ground state takes place. b) For direct trapping, a single collision takes place in which the carrier falls to the dot ground state. For sequential trapping, the first collision helps the carrier to relax in the WL states, while a subsequent collision will help the carrier to relax in the dot ground state.

Irrespective of the precise capture process, it is clear in Figure IV-5 that the decay times for the QD are faster in cases of resonant excitation. Figure IV-7 gives a summary of the various rise times and decay times observed for different detection energies. The rise time is defined here as the time necessary for the TRPL signal to reach its maximum value. It should be noted that this definition of the rise time is not usually used, as normally a deconvolution of the spectrum is performed to extract the real rise time, as opposed to the observed rise time which is slower due to the detector response time. Decay times have been obtained by fitting our results to a triple-exponential decay and keeping the dominant (fastest) component which is adequate for at least the first decade in intensity. This does not represent a specific physical process but provides a general trend to summarize the data. Figure IV-7a shows the rise time for resonant (open symbol) and nonresonant (solid symbol) conditions. The rise time obtained for the resonant cases are consistently shorter than for the nonresonant case (except for two points at lower energy), although the difference is small. A possible explanation for this would be that the photons are first absorbed by creating an electron-hole pair in an excited state, exactly one LO phonon higher in energy, followed by a resonant phononic relaxation to the ground state. Such faster rise times for resonant excitation energies related to LO phonon energies above the band edge have been observed in quantum well structures[55]. However, even when pumping with high intensities the dot emission line does not show evidence of the emergence of a higher energy emission line associated with excited state emission. The interpretation in terms of absorption in an excited state is therefore not believed to be true. Also, it should be mentioned that, as can be seen in Figure IV-5b, the rise part of the

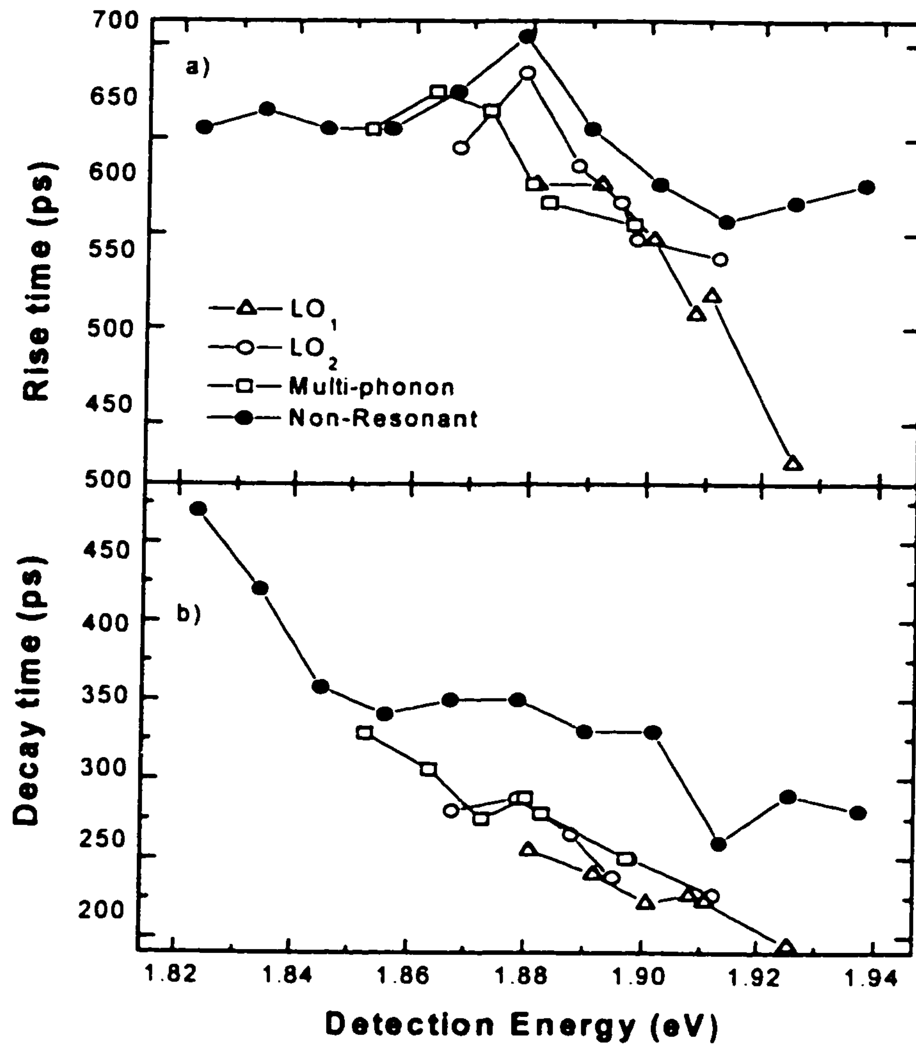

Figure IV-7

Rise times as defined in the text are shown in (a) and decay times in (b) as a function of detection energy. Solid (open) symbols show the results obtained for nonresonant (resonant) excitation conditions. The instrumental response of the system is 420 ps for the rise time and 100 ps for the decay time.

spectrum is very similar for the three curves shown. This suggests that the capture rates for a given detection energy are equal within experimental resolution for resonant and non-resonant excitation.

Figure IV-7b summarizes the decay times for resonant (open symbol) and

nonresonant (solid symbol) conditions. The nonresonant decay times become shorter with higher detection energies. This might be explained by an increased carrier confinement for higher emission energies. As smaller islands are probed, the decreased lateral and vertical dimensions cause a shift of the bound states towards higher energies. At the same time, the smaller island dimension causes a better overlap of the wavefunctions which increases the recombination rate. Figure IV-7b also confirms that for the detection energy range probed, the decay times are shorter in the case of resonant excitation. This was already observed in Figure IV-5, and this phenomenon seems puzzling since resonant phonon absorption is expected to speed up the capture process, but once the carriers have relaxed to the dot ground state the recombination time (lifetime) is expected to be the same irrespective of the capture process.

An element of the answer to this surprising result may be revealed by the study of the power dependence of the sharp line spectrum. The evolution of the micro-PL spectrum is monitored as a function of excitation intensity for the quantum dot emission lines in Figure IV-8. The excitation energy was set at 1.960 eV which corresponds to wetting layer absorption. The low intensity spectrum simply reproduces the features of Figure IV-2a. Exciting with even lower intensities will only produce a spectrum similar to the one observed in (a). As the intensity is increased, most of the sharp spectral features (A to F) lose amplitude with respect to the collective emission background, and in some cases even disappear completely, the most striking example being peak H. Lines that remain identifiable tend to stay narrow, although some of them do show evidence of broadening (peak B for example). In some cases, higher intensities have little effect (J, K, L) or even

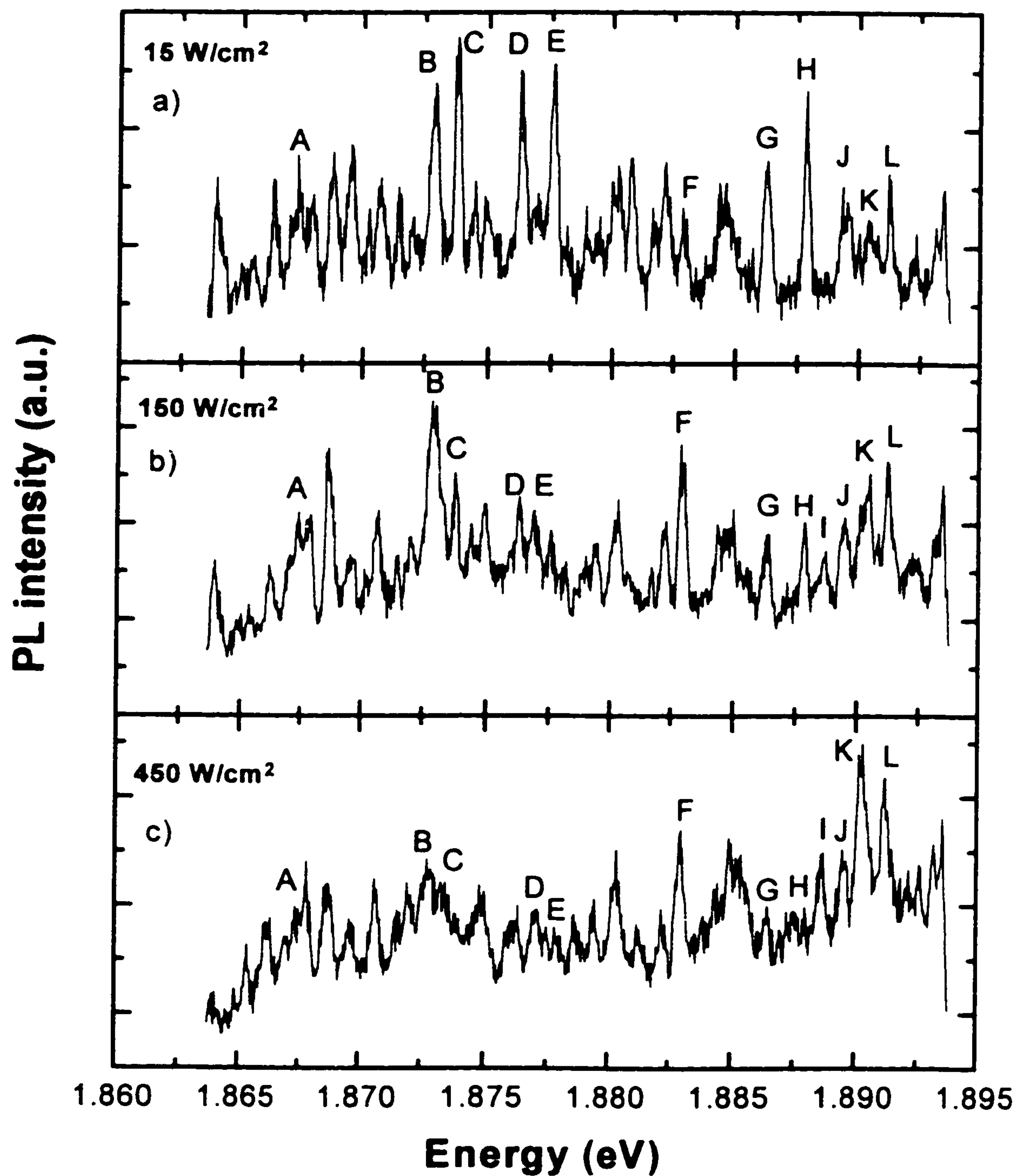

Figure IV-8

PL spectrum obtained at 4K from sample VI for different excitation intensities. The CW dye laser system was used with the excitation energy set at 1.960 eV.

cause the emergence of new features. Line I for example is barely detected at low intensity, but progressively rises above the background as the intensity is increased. These observations cannot be related to temperature effects, since Figure IV-2 clearly shows that increasing the temperature does not change the spectrum in that respect. An increase in the carrier population is more likely to be at the origin of the new spectral features. Neglecting the dynamics of the higher energy states, the steady state population is given by the product of the photogenerated carrier flux, $\Phi(I_{exc})$, and the lifetime in the quantum dot ground state, τ_{GS}. Estimating τ_{GS} to be 400 ps as obtained from our single dot experiment, and for excitation intensities of 15 W/cm^2, 150 W/cm^2 and 450 W/cm^2, the steady state population is estimated at 0.002, 0.02 and 0.06 per dot respectively[67]. Thus, it seems that even in the regime of fewer than one electron-hole pair for very low excitation power densities there is a significant change in the observed properties. The presence of carriers in the QD at the moment of recombination is expected to have an effect on the recombination energy[43,68]due to the modified Coulomb interaction. The corresponding renormalization in the emission energy are expected to be in the range of a few meV, depending on the exact nature of the interaction and the resulting binding energy. If one imagines that within a given dot, the radiative recombination will sometimes occur in the presence of other carriers and sometimes occur without this presence, the energy renormalization causes one dot to emit at two or more slightly different energies. At very low excitation energies only "excitonic" lines are observed, but as the excitation intensity is increased one should observe the emergence of "biexcitonic" lines in the spectrum. Thus, as the number of emission lines increases the collective emission background is

enhanced with respect to the sharp "single dot" lines. Note that this renormalization could cause the emergence of new features if one or a few of the "biexcitonic lines" happen to appear right in between two non-renormalized lines. Such could be the case of line I for example.

Alternatively, similar phenomenon could be observed if part of the dot population starts to contribute to the emission only above a certain excitation power threshold.

Radiative recombination from excited states would also give lines at higher energies, but this is an unlikely scenario here given that the large interlevel spacing associated to small quantum dots would lead to peaks several tens of meV on the high energy side of the ground state emission[64].

Finally, the enhanced background emission observed in Figure IV-8 could be the manifestation of "background states" associated with the quantum dots. S. J. Lee *et al.* (ref. 33) have shown that for semiconductor quantum dots with finite barriers the density of states, although comparatively small, is non-zero between the bound states. Thus, as the carrier population is increased, carriers are forced to dwell in this flat DOS background, producing a flat emission band which progressively rises with higher excitation intensity. This background could also be responsible for the slow tail observed in the TRPL spectra of Figure IV-5b, and it could significantly contribute to the strong resonant absorption characteristics of the quantum dots. Finally, the phonon resonances observed in the macro-PL spectrum of Figure IV-5a can be thought to be a manifestation of enhanced bound state emission compared to "background state" emission. In this case, the transient LO_1 and LO_2 spectra of Figure IV-5b reflect the shorter radiative lifetimes of the carriers in the

bound states. Thus, at the moment more experiments focusing on this issue are needed to clarify the role of phonons in self-assembled carrier dynamics.

In summary, temperature independent FWHM and lifetimes of the "single dot" (in reality one to six) emission lines have unambiguously shown the 0D nature of the DOS in the islands. Transient properties of the dot ensemble excited resonantly have shown clear speed-up of the dynamics, but this was not observed as a faster capture rate, but rather as a faster decay rate. Finally, intensity dependent measurements hint towards the presence of weak "background states" in the DOS between the dot bound states. This effect could be related to some of the properties observed in the "large ensemble" dynamics and experiments specifically designed to clarify this point are needed.

In this chapter, the experimental results show no manifestation of excited bound states in the quantum dots. Although the importance of resonant excitation was clearly shown, the absence of excited states limited our ability to study the inter-sublevel dynamics. This is one of the main objectives of the next chapter with sample IR.

V Excited states dynamics: properties of InGaAs self-assembled dots

Sample VI proved to be a useful system for an initial study of self-assembled islands. The strong emission in the visible range made it an easy sample to characterize experimentally, and the fact that most of its properties could be explained in terms of a single bound state per dot simplified the analysis. Also, the high quantity of sample pieces available allowed the use of destructive techniques, such as wet chemical etching, which proved useful to perform micro-PL measurements. In contrast, only a small 2x1.5 mm piece of sample IR was available. This restricted the possibility to study small ensembles of islands in order to reveal the properties of "single dots". To overcome this difficulty, a new way of proving the zero-dimensional properties of the islands was obtained by means of magneto-PL measurements on macroscopic ensembles of dots. This techniques takes advantage of the presence of many bound states in these bigger dots and the resulting evolution of the PL spectrum as a function of magnetic field will be presented in the last part of this chapter (section V-4). In the first section, the known properties of InGaAs/GaAs quantum wells are used to build a simple model for the potential in the quantum dots. The energy spacing between transitions can thus be determined, and the predictions of this calculation are compared with intensity dependent PL results presented in the second section. In the third section, the inter-sublevel dynamics of the carriers is studied by means of up-conversion measurements. As discussed in section II.4, the

presence of a continuum of energy states in higher dimensionality structures (1D, 2D, 3D) guaranties that selection rules for phonon-assisted transitions can be readily satisfied. Consequently, thermalization of the carriers to the ground state of a particular band can be achieved easily in higher dimensionality structures via sequential LO and LA phonons scattering[55,69,70,71]. This remains true even when the carriers are created in a high-index state (ex.: n=2) due to the continuum of states available[72]. The situation is different for a quantum dot with a discrete DOS in which the energy difference between the bound states is not likely to match the phonon energies. The presence of several bound states in the quantum dots of sample IR provides a very good test ground for the problem of inter-sublevel dynamics in quantum dots.

V.1 Single dot modeling

In this section, the method presented in chapter two to calculate the bound state energies of carriers trapped in a lens shaped dot is improved to obtain a more realistic estimation of the energy spacing for optical transitions.

The QD is modeled as a hemispherical cap, with a fixed height l_0 and radius at the base ρ_0, formed on a wetting layer of thickness t_w, as shown in Figure V-1. The confining potential is zero inside the dot and wetting layer, but finite outside. The effective-mass Hamiltonian is used to describe both valence and conduction band states:

$$-\frac{\hbar^2}{2m^*}\nabla^2\Psi + V\Psi = E\Psi \qquad \text{V-1}$$

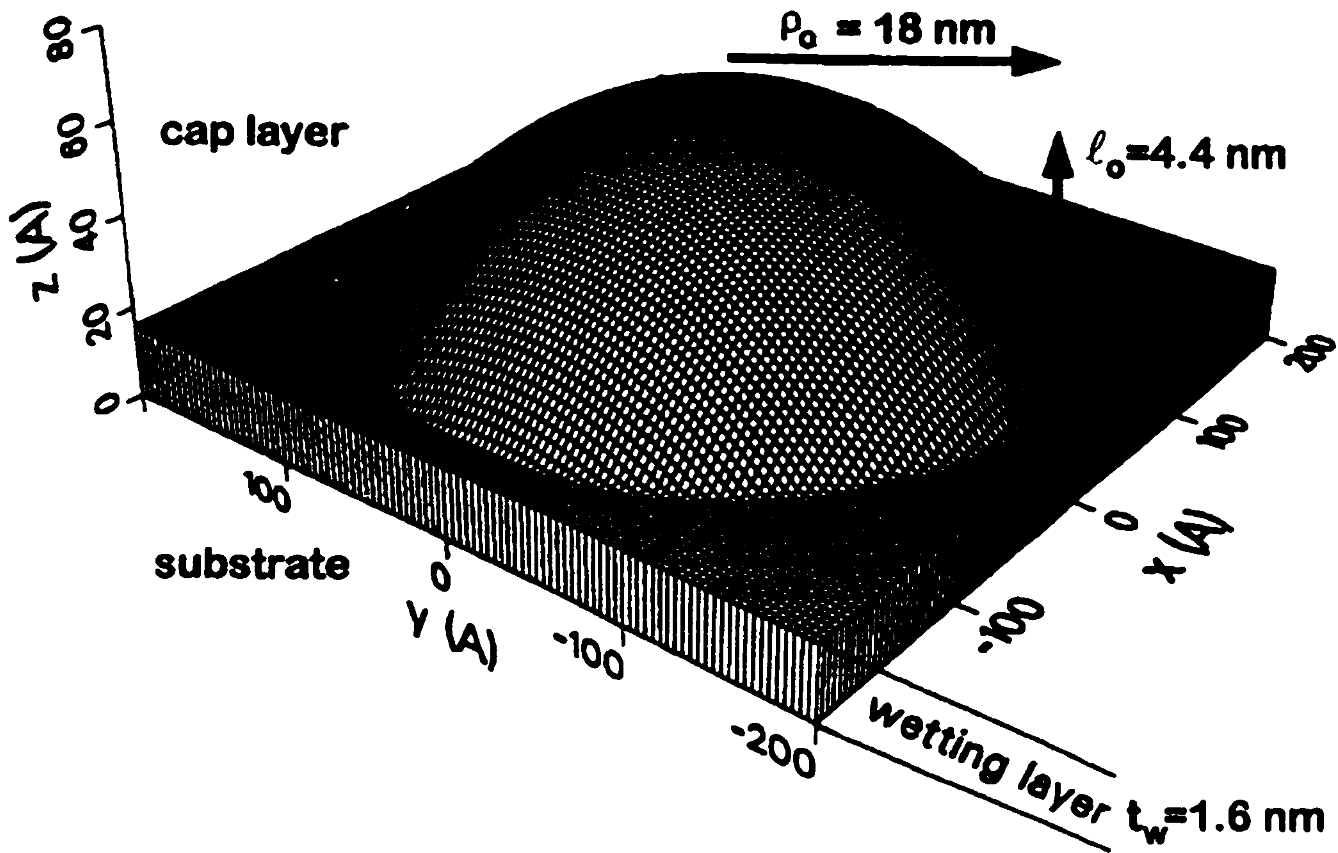

Figure V-1

Representation of the shape of the quantum dot used in the model. A typical island has a hemispherical cap of height ℓ_0=4.4 nm, with radius at the base ρ_0=18 nm and wetting layer thickness t_w=1.6 nm.

where the effective mass (m^*), and the potential (V) have to be chosen consistently with the band described. Equation V-1 can be separated as explained in Section II-2 and is transformed into an equivalent system of equations:

$$-\frac{\hbar^2}{2m_w^*}\frac{\partial^2\Phi_x(x)}{\partial x^2}+V_x^{eff}\Phi_x(x)=E_x\Phi_x(x) \qquad \text{V-2a}$$

$$-\frac{\hbar^2}{2m_w^*}\frac{\partial^2\Phi_y(y)}{\partial y^2}+V_y^{eff}\Phi_y(y)=E_y\Phi_y(y) \qquad \text{V-2b}$$

$$-\frac{\hbar^2}{2m^*(z)}\frac{\partial^2\Phi_z(z)}{\partial z^2}+V_z^{QW}\Phi_z(z)=E_z\Phi_z(z) \qquad \text{V-2c}$$

$$E=E_x+E_y+E_z \qquad \text{V-2d}$$

$$\Psi=\Phi_x\Phi_y\Phi_z \qquad \text{V-2e}$$

where $V_x^{eff}=E^{QW}(l(x))-E^{QW}(l_0+t_w)$ and $V_y^{eff}=E^{QW}(l(y))-E^{QW}(l_0+t_w)$ are effective potentials obtained in the adiabatic approximation; V_z^{QW} is the potential of an InGaAs/GaAs quantum well of width l_0+t_w:

$$V_z^{QW}=\begin{cases}0 & for \quad 0<|z|<l_0+t_w\\ V_0 & otherwise\end{cases}$$

and finally $m_z^*(z)$ is replaced by the appropriate mass depending on the layer considered

$$m^*(z)=\begin{cases}m_w^* & for \quad 0<|z|<l_0+t_w\\ m_b^* & otherwise\end{cases}$$

where m_w^* is the effective mass of the carriers in the InGaAs layer and m_b^* is the carrier effective mass in the barrier layer.

The main improvement of equations V-2 compared to the theory presented in chapter two comes from the consideration of a finite potential barrier. In this case, the energy levels of a quantum well of thickness l can be obtained from the implicit equation[54]

$$l\left(E_{nz}^{QW}\right)=\frac{2\hbar}{\sqrt{m_w^*E_{nz}^{QW}}}\left[arctan\left\{(-1)^{(n_z+1)}\left(\sqrt{\frac{m_w^*}{m_b^*}\left(\frac{V_0}{E_{nz}^{QW}}-1\right)}\right)^{(-1)^{(n_z+1)}}\right\}+\pi*int\left(\frac{n_z}{2}\right)\right] \qquad \text{V-3}$$

where n_z=1,2...is the level index in the z direction, V_0 is the band discontinuity, m_w^* and m_b^* are the effective masses inside the island and in the barrier respectively. The above equation cannot be inverted to obtain an exact expression for $E_{n_z}(l)$ and one must obtain a numerical solution. Also, one should note that equation V-3 does not directly take the strain into account and this causes a significant error (several tens of meV) on the absolute position of the emission lines. More accurate models including the effect of the strain have been developed for lens shaped dots of InGaAs/GaAs[35] and for pyramidal dots of InAs/GaAs[73]. However, assuming that the strain causes a constant energy shift independent of the well thickness, one can still estimate the separation of the energy levels with good accuracy.

V.1.1 Conduction Band

For the conduction band, the following parameters are used:

m_w^*	m_b^*	V_0 (meV)
$0.067\,m_0$	$0.067\,m_0$	350 meV

Table V-1

Parameters used for modeling the conduction band.

where m_w^* is the strained InGaAs conduction band effective mass[74], m_b^* is the unstrained GaAs effective mass and V_0 has been estimated for InGaAs/GaAs strained layers assuming

a 67% conduction band offset in reference 35.

For $l = l_0 + t_w$ =6.0 nm, the values found for E_{nz}^{QW} are

$$E_{nz=1}^{QW}(6.0nm) = 116meV$$

$$E_{nz=2}^{QW}(6.0nm) = 347meV$$

from which one can see that the first excited state in this direction is very weakly bound ($E_2^{QW} \sim V_0$) which justifies the approximation of a single bound state in the z direction. Replacing for $n_z = 1$, in equation V-3 one gets

$$l = \frac{2\hbar}{\sqrt{0.067m_0 E^{QW}}} * arctan\left(\sqrt{\frac{V_0}{E^{QW}} - 1}\right) \qquad \text{V-4.}$$

This equation is used to numerically calculate $E^{QW}(l(x))$ and $E^{QW}(l(y))$. An expression for $l(x)$ ($l(y)$) can be found in a similar way as $l(\rho)$ was obtained in chapter 2 with the difference that one now has to consider the presence of the wetting layer. Figure V-2 presents a cross section of the ideal quantum dot presented in Figure V-1 along the x direction. From that picture one can easily see that

$$l(x) = \sqrt{R^2 - x^2} - h \qquad \text{V-5}$$

and the values of R and h can be obtained from the two equations presented in the figure along with the known values of ρ_0, l_0 and t_w so that $E^{QW}(x)$ can be calculated by numerically inverting the implicit equation

$$\sqrt{39.02^2 - x^2} - 33.02 = \frac{67.6}{\sqrt{E^{QW}}} * arctan\left(\sqrt{\frac{350}{E^{QW}} - 1}\right) \qquad \text{V-6}$$

where E^{QW} is in meV and x is in units of nm. The result obtained from the above

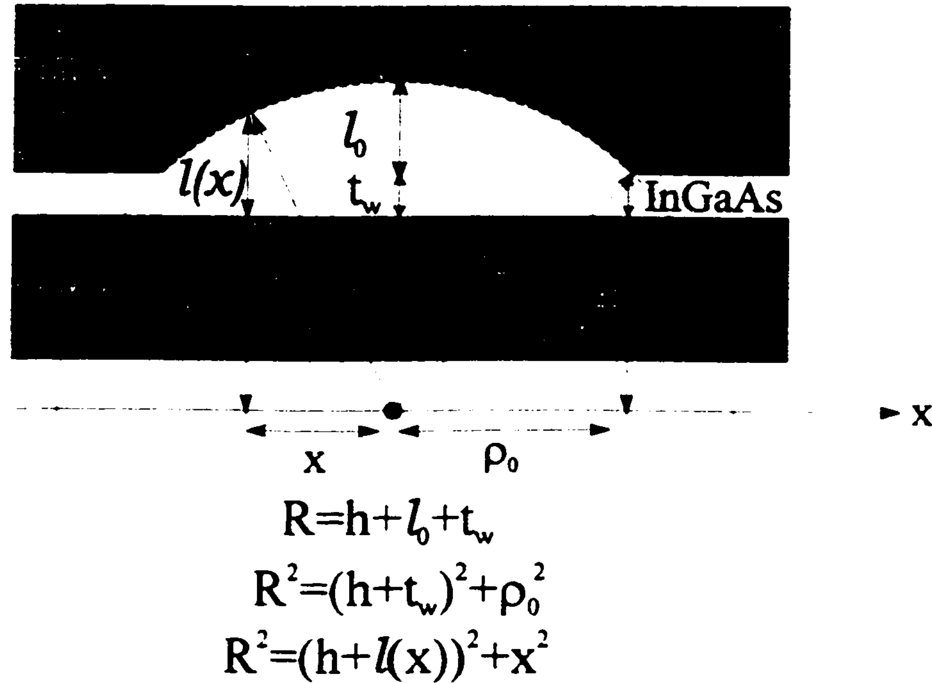

Figure V-2

Cross section of the idealized quantum dot as defined in picture V-1.

equation is shown as a solid curve in Figure V-3 where the energy reference is taken at the bottom of the conduction band. Starting at 116 meV, the confinement energy of an InGaAs/GaAs quantum well of thickness $l_o + t_w$, the effective potential curves upwards until it reaches the wetting layer ground state energy, at which point the electrons are no more confined laterally since they are free to move in the x-y plane. The dashed curve is obtained from a quadratic fit of the effective lateral potential for $|x| < 10nm$ and the corresponding expression for V_x^{eff} is given in the inset. By symmetry the same expression is valid for V_y^{eff} provided one replaces x by y. Substituting the expressions of V_x^{eff} and V_y^{eff} in equation V-2 yields

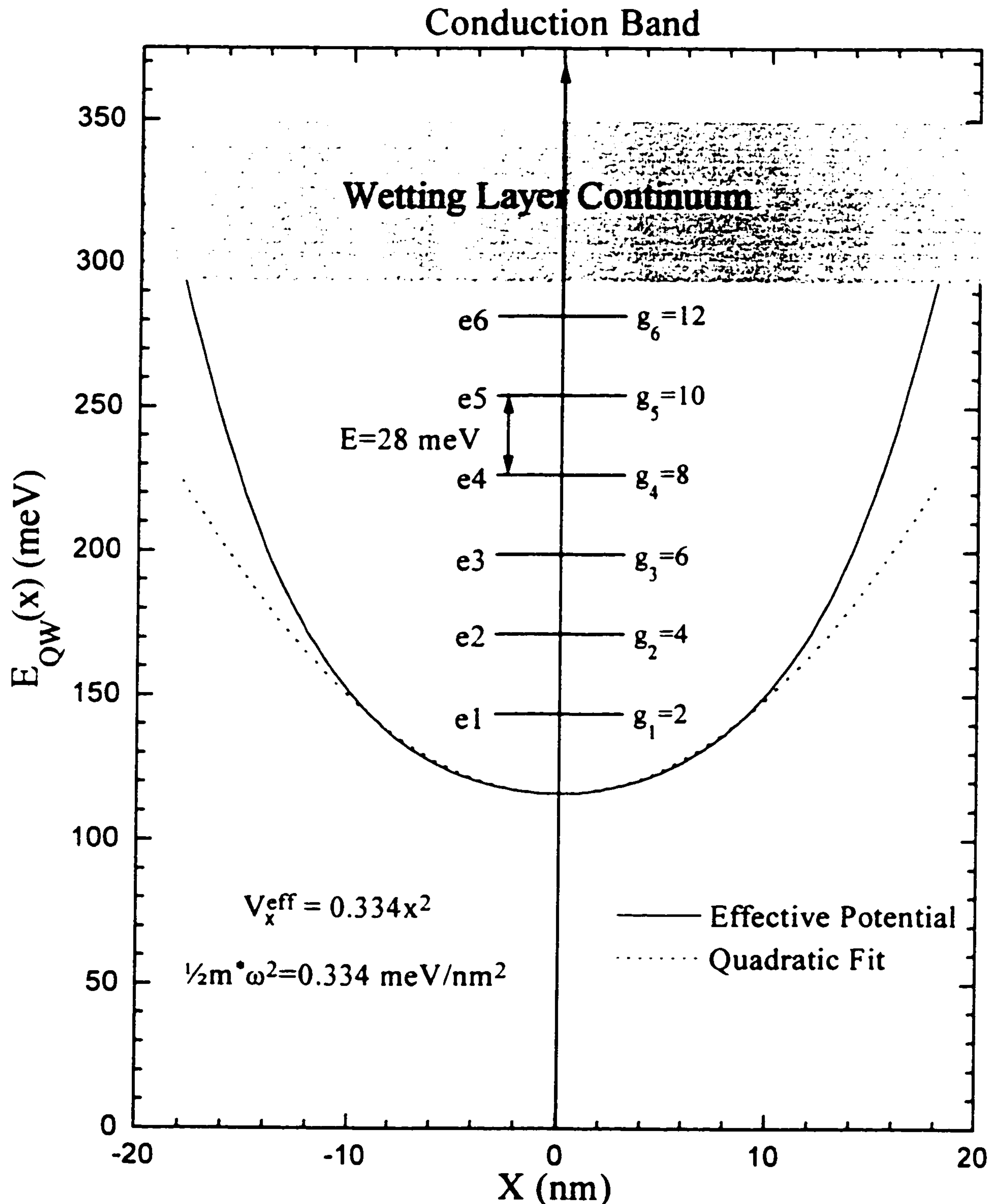

Figure V-3

Evolution of the effective lateral confining potential (solid line) for the conduction band states as obtained from the ground state energy of an InGaAs/GaAs quantum well of thickness L(x). The quadratic approximation (dashed curve) gives a good approximation for x<10 nm and provides a simple expression for the effective potential as shown in the inset. From the coefficient of the quadratic term, the eigenenergy is found to be 28 meV.

$$-\frac{\hbar^2}{2m_w^*}\frac{\partial^2\Phi_x^{cb}(x)}{\partial x^2}+0.334x^2\Phi_x^{cb}(x)=E_x^{cb}\Phi_x^{cb}(x) \qquad \text{V-7a}$$

$$-\frac{\hbar^2}{2m_w^*}\frac{\partial^2\Phi_y^{cb}(y)}{\partial y^2}+0.334y^2\Phi_y^{cb}(y)=E_y^{cb}\Phi_y^{cb}(y) \qquad \text{V-7b}$$

where the energies and the wavefunctions have been identified as conduction band values by the superscript cb. The above is the set of equations for a two-dimensional uncoupled harmonic oscillator with $\frac{1}{2}m^*\omega^2 = 0.334(meV/nm^2)$, from which the energy eigenvalues can immediately be obtained by computing the product $\hbar\omega$ and one gets a value of 28 meV. The eigenvalue spectrum is then

$$E^{cb} = E_x^{cb} + E_y^{cb} + E_z^{cb} = 28(n_x + n_y + 1) + 116 \quad n_x, n_y = 0,1,2... \qquad \text{V-8.}$$

where n_x (n_y) is the number of oscillations in the x (y) direction. The bound state energies are indicated by transverse bars in Figure V-3 along with their degeneracy level g_i (including spin degeneracy). A natural basis for the wavefunctions is given by $|n_x, n_y, n_z\rangle$ where n_x, n_y = 0,1,2,3,4,5 and n_z=1. Since this last index is fixed it can be dropped and one only needs to specify n_x and n_y. Moreover, for most of the discussion in this chapter it is sufficient to specify the level index defined as n=(n_x+n_y+1), hence the notation e1,e2... which denotes an electron in level 1,2...

The wavefunctions are given by

$$\Psi = \Phi_x^{cb}\Phi_y^{cb}\Phi_z^{cb} = \phi_{nx}(x)\phi_{ny}(y)\chi_1(z) \qquad \text{V-9}$$

where ϕ_n stands for the nth one-dimensional harmonic oscillator wavefunction with a

length scale given by $\beta_{cb}^{-1} = \left(\frac{\hbar}{m_w^* \omega} \right)^{\frac{1}{2}} = 5.7\,nm$; χ_1 denotes the ground state wavefunction of an InGaAs/GaAs quantum well of thickness $l_0 + t_w$.

V.1.2 Valence Band

For the valence band, the situation is somewhat more complicated. First, the presence of the strain splits the $m_J = \pm\frac{3}{2}$ (heavy-hole) and $m_J = \pm\frac{1}{2}$ (light-hole) at $\vec{k} = 0$ and as a result the band edge states are heavy hole states while the light-hole states are not confined anymore[75]. Also it has been shown that for strained InGaAs quantum wells the $m_J = \pm\frac{3}{2}$ states have an anisotropic mass[74], as the in-plane mass is a light-hole mass and the transverse mass is a heavy-hole one. These effective masses are strain dependent and despite a growing interest, the strain distribution in self-assembled dots remains a matter of discussion[73]. Since this subject is not the focus of this work, as a first approximation the following discussion assumes that a simple isotropic mass can give us a reasonable estimate for the spacing of the energy levels. The hole mass is assumed to be close to the GaAs light hole mass due to the heavy-hole light-hole mixing induced by the strain distribution. The barrier effective mass is the GaAs heavy-hole mass and the band discontinuity is obtained assuming a 33% valence band offset. The resulting parameters are presented in Table V-2.

m_w^*	m_b^*	V_0 (meV)
$0.085\, m_0$	$0.45\, m_0$	175 meV

Table V-2

Parameters used for modeling the valence band.

Replacing these parameters in equation V-3, assuming $n_z=1$ and using equation V-5 for $l(x)$ one obtains the following implicit equation for $E^{QW}(x)$

$$\sqrt{39.02^2 - x^2} - 33.02 = \frac{59.9}{\sqrt{E^{QW}}} * arctan\left(\sqrt{\frac{0.085}{0.45}\left(\frac{175}{E^{QW}} - 1\right)}\right) \qquad \text{V-10}$$

where energy is in units of meV and length in units of nm. The resulting effective lateral potential is shown as a solid curve in Figure V-4 where the energy reference is taken at the top of the valence band. Note that for simplicity, the energy scale in Figure V-4 has been inverted with respect to the one used in Figure V-3 since we are now considering holes. Starting at 43 meV, the confinement energy for the valence band of an InGaAs/GaAs quantum well of thickness $l_o + t_w$, the effective potential curves upwards until it reaches the wetting layer ground state energy, at which point the electrons are free to move in the x-y plane and are no more confined laterally. The dashed curve shows a quadratic fit near the center ($|x| < 10$ nm) of the dot and one can see that it provides a satisfying approximation for this portion of the potential. From the fit, a constant energy spacing of 14 meV is deduced and only five bound states are observed, in contrast with the case of the conduction band where 6 bound states are predicted. The eigenvalue spectrum for the valence band is given by

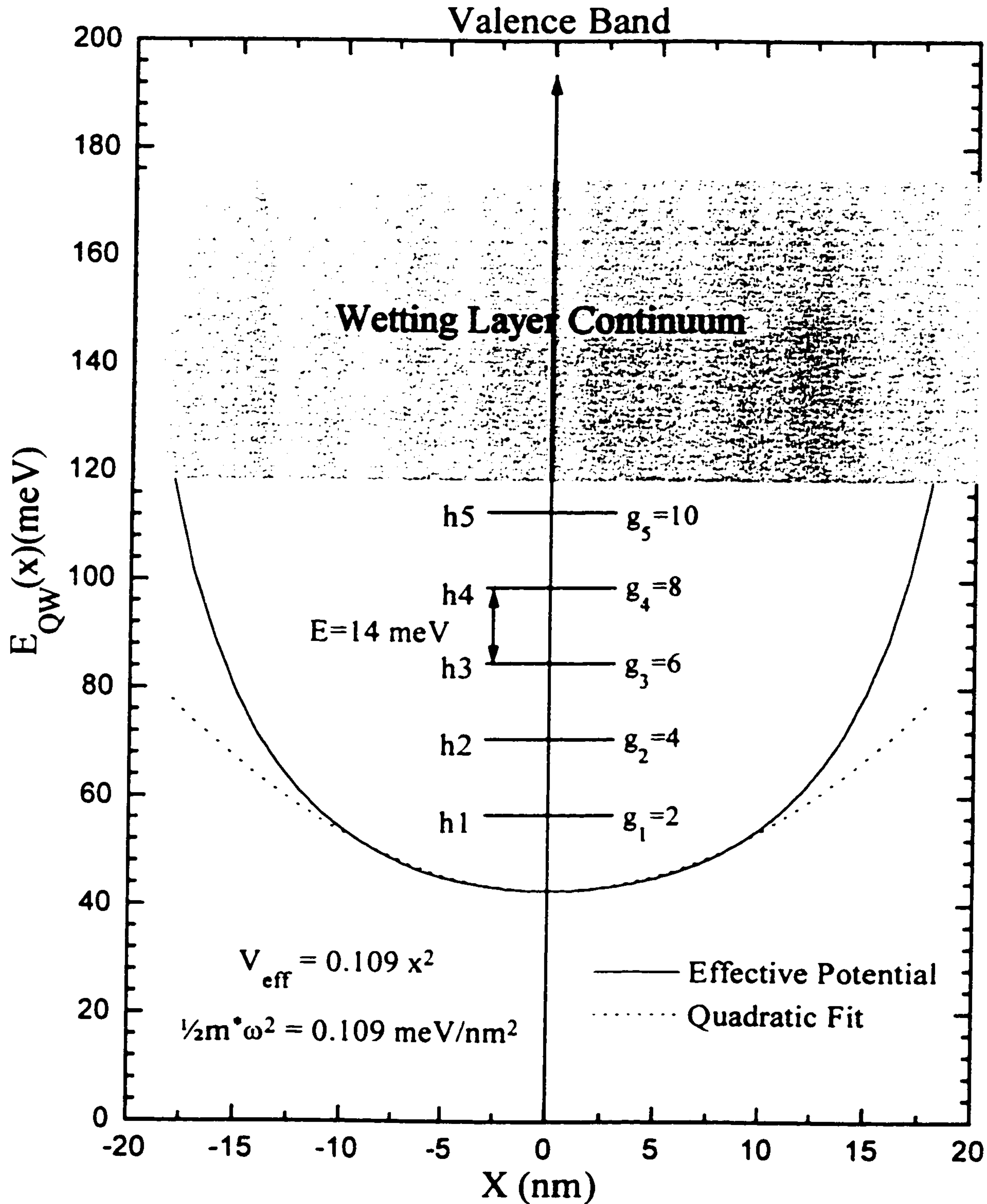

Figure V-4

Evolution of the effective lateral confining potential (solid line) for the valence band states as obtained from the ground state energy of an InGaAs/GaAs quantum well of thickness L(x). The quadratic approximation (dashed curve) gives a good approximation for x<10 nm and provides a simple expression for the effective potential as shown in the inset. From the coefficient of the quadratic term, the eigenenergy is found to be 14 meV.

$$E^{vb} = E_x^{vb} + E_y^{vb} + E_z^{vb} = 14\left(n_x + n_y + 1\right) + 43 \quad n_x, n_y = 0,1,2\ldots \qquad \text{V-11}$$

Following the notation for the conduction band the states are labelled h1,h2... according to a single quantum number related to the total number of energy quanta $n=(n_x+n_y+1)$. The corresponding wavefunctions are

$$\Psi = \Phi_x^{vb}\Phi_y^{vb}\Phi_z^{vb} = \phi_{nx}(x)\phi_{ny}(y)\chi_1(z) \qquad \text{V-12}$$

where ϕ_n stands for the nth one-dimensional harmonic oscillator wavefunction with a length scale given by $\beta_{vb}^{-1} = \left(\frac{\hbar}{m_w^* \omega}\right)^{\frac{1}{2}} = 8.0\ nm$; χ_1 denotes the ground state wavefunction of an InGaAs/GaAs quantum well of thickness $l_0 + t_w$.

Comparing the length scales β^{-1} obtained for the conduction and valence band, one can conclude that there is a significant difference between the lateral extension of the electron and hole wavefunctions. This is in contrast with the result obtained in chapter II for infinite potential barriers, in which case it was shown that the lateral extension is independent of the effective mass. In that case the selection rules obtained in section II.4 implied that radiative transitions can only occur betwen states with the same quantum numbers. In contrast, for a finite wall case the lateral extension of the wavefunction is not the same for both electrons and holes, and as a consequence the selection rules obtained are somewhat relaxed compared to those of chapter two. This means that some of the transitions forbidden for the hard wall case become allowed in the finite wall case. This effect is neglected in the discussion that follows, and it is assumed that transitions between states with the same quantum number n are much stronger than other transitions. In

particular transitions between an even and an odd index state remain forbidden because of parity. Therefore, in the discussion that follows an e1-h1 recombination between a n=1 hole and a n=1 electron is simply referred to as an n=1 transition.

With the above selection rules, there are 5 different radiative transitions allowed for carriers trapped in a quantum dot of sample IR. The energy of the photons emitted are given by

$$E^{rad} = E_{gap} + E_{strain} + E^{cb} + E^{vb} \qquad \text{V-13}$$

where E_{gap} is the energy gap of lattice-matched InGaAs and E_{strain} is the contribution of the strain distribution. Replacing E^{cb} and E^{vb} by their respective expression from equation V-8 and V-11 yields

$$E^{rad} = E_{gap} + E_{strain} + 159\,meV + n*42meV \qquad \text{V-14}$$

where n is the transition index and accepts values ranging from 1 to 5. From this, the energy spacing between radiative transition lines is expected to be ~42 meV.

V.2 Steady state photoluminescence

In the previous section, the time-independent form of the Hamiltonian for a typical InGaAs quantum dot was modeled and the stationary states of a single dot were obtained. In this section, steady state photoluminescence experimental results obtained from sample IR are presented under different excitation conditions, namely CW excitation and pulsed excitation. The results are interpreted in light of the calculation of section V-1, and also in terms of dynamical properties of an ensemble of quantum dots.

V.2.1 CW excitation

As a starting point for the investigation of the steady state properties of sample IR, the set-up of Figure III-4 is used to perform CW PL. A CW AR^{+}-ion laser is used as an excitation source and the sample signal is detected with the Germanium detector.

Figure V-5 summarizes the results obtained for different excitation intensities. At very low excitation density (0.20 W/cm^2), only one emission peak is observed at 1.10 eV with a shoulder at 1.13 eV. As the power is increased, up to 5 peaks are resolved including the ground state, and the transitions are labeled from n=1 to n=5 according to the labeling scheme developed in the previous section. Table V-3 summarizes the transition energies obtained from the peak positions of Figure V-5.

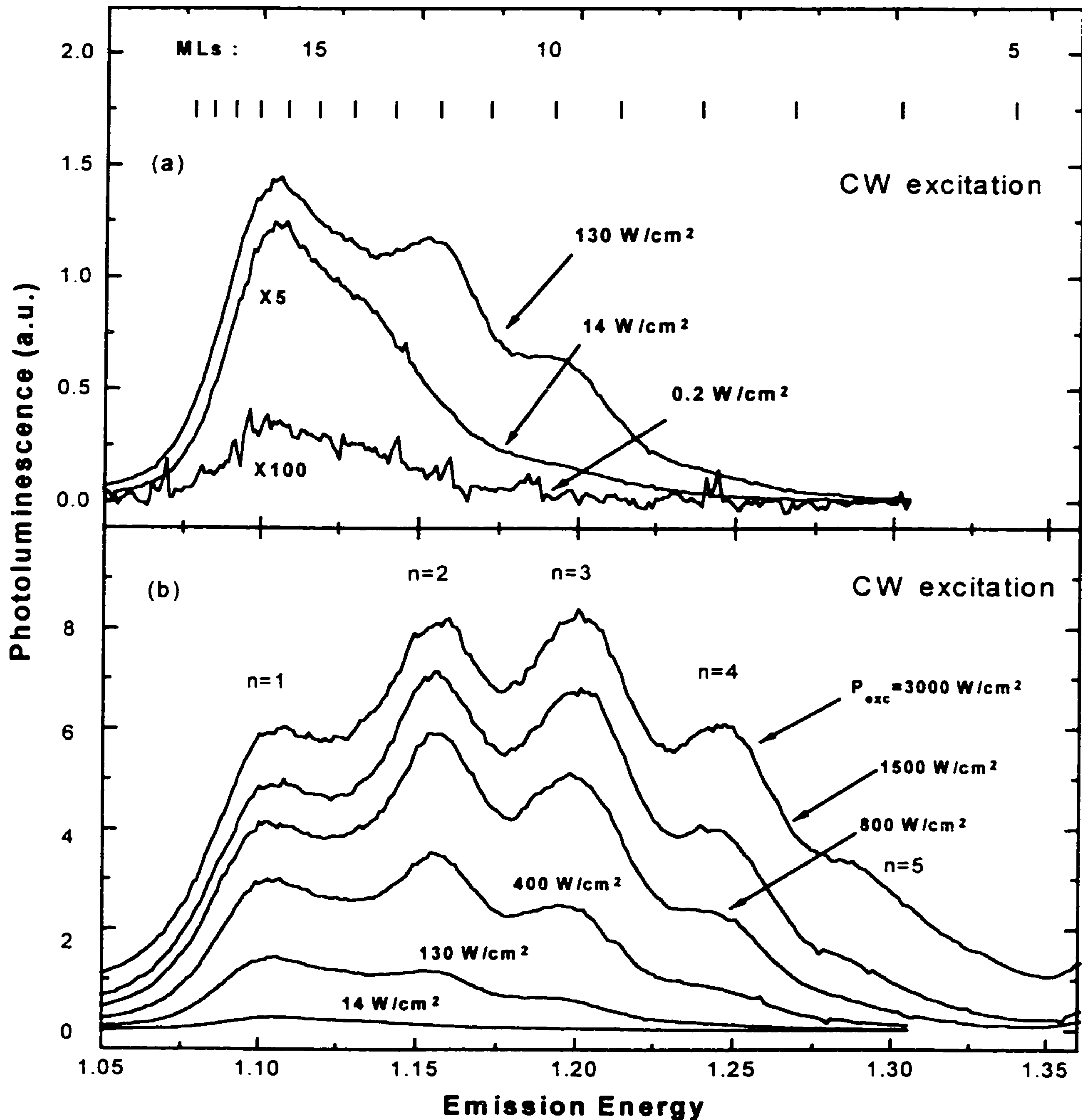

Figure V-5

Evolution of the low temperature (4 K) emission spectrum as a function of nonresonant (E_{exc}=2.54 eV) excitation intensity with a CW laser source. In (a), for very low excitation intensity only ground state emission is observed. The vertical bars show the emission energy of strained InGaAs/GaAs quantum wells of the same composition as sample IR as a function of thickness in monolayers. In (b), higher energy emission lines appear progressively as the excitation intensity is increased.

	n=1	n=2	n=3	n=4	n=5
Peak Position (eV)	1.107	1.157	1.202	1.247	1.287

Table V-3

Transition energies obtained from the peak positions of figure V-5.

The higher energy peaks of Figure V-5 could originate from various phenomenon, each one having its own characteristics. For example, in the absence of the self-assembling process, it is possible that monolayer fluctuations (ML) of a 2D layer will lead to the observation of multiple peaks in the macro-PL experiments[76]. Alternatively, higher energy emission could originate from excited quantum dot state interband transitions[64,77]. In the latter case, the population of higher levels could be achieved because of a restricted relaxation rate (phonon bottleneck), or via the Pauli exclusion principle forcing carriers to remain in higher energy states when lower states are populated (state-filling). Alternatively, if one assumes that only ground state emission is observed, the higher emission line can be ascribed to segregated inhomogeneous broadening. In this case, it has been observed that long range fluctuations along the sample surface could be held responsible for the existence of different families of islands[78], each giving rise to a distinct emission line. The above four effects (monolayer fluctuations, phonon bottleneck, state-filling and segregated inhomogeneous broadening) are represented in Figure V-6. All of them can give rise to higher energy emission peaks, and each has specific characteristics.

The good island size and near-neighbor distance uniformity observed in Figure I-3

A) Monolayer Fluctuations

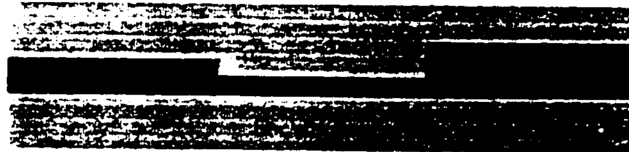

B) Inhomogeneous broadening - Phonon Bottleneck
- State Filling

C) Segregated Inhomogeneous broademing

I- From wetting layer monolayer fluctuations

II- From compositional disorder

Figure V-6

Illustration of the different types of layers that could give rise to higher emission lines as observed in Figure V-5. In the figure, inhomogeneous broadening in a given dot population is represented by size fluctuations, while compositional disorder is represented by a change in color. A) Excitons localized in regions of a QW with different thickness give rise to emission lines at different energies. B) Electron-hole pairs localized in large islands can give rise to excited state emission C) Electron-hole pairs localized in quantum dots with different wetting layer thickness/alloy composition or other variations could give rise to several emission lines, even if there were only one bound state in the dots.

tends to dismiss the possibility of segregated inhomogeneous broadening for this sample. Also, the calculated emission energies for a corresponding hypothetical quantum well with various numbers of MLs are shown at the top of Figure V-5a. One can see that there is a complete lack of correlation of the emission energies with the emission expected for ML fluctuations. On the other hand, the average energy spacing of 45 meV obtained by inspecting Table V-3 correlates well with the transition energy spacing predicted in section V-1 for a quantum dot.

Also, one expects that the excitation intensity required to observe saturation effects will be different when comparing a quantum well to an ensemble of quantum dots. For example, in Table IV-4 D_{QW} represents the density of conduction band states in the ground state of a quantum well, while D_{QD} represents the density of conduction band states for the ground state of a quantum dot layer. To calculate D_{QW} , equation II-9 is used considering only the ground state in the sum, which yields

$$D_{QW}(E) = \frac{m_e^*}{\pi\hbar^2}(E_2 - E_1) \qquad \text{V-15}$$

where L^2 has been factored out so as to consider the areal density of states, and E has been set to E_2, since no saturation will be observed in a PL experiment unless the Fermi level is raised above the energy of the second subband. From Table V-3, the energy difference E_2-E_1 is equal to 50 meV, while m_e^* for strained InGaAs is given in Table V-1. To calculate D_{QD}, the island areal density given in figure I-3 is multiplied by g_1, the degeneracy of the n=1 state as given in Figure V-3. Comparing D_{QW} and D_{QD} in Table V-4, one can see that the population density required to observe state-filling effects differs

P_{exc}(W/cm^2)	f	σ(cm^{-2})	D_{QW}(cm^{-2})	D_{QD}(cm^{-2})	N_D
0.2	0.19	8.8x10^7	1.4x10^{12}	2.3x10^{10}	0.0077
1.4	0.18	6.4x10^8	1.4x10^{12}	2.3x10^{10}	0.056
14	0.18	6.5x10^9	1.4x10^{12}	2.3x10^{10}	0.56
45	0.20	2.2x10^{10}	1.4x10^{12}	2.3x10^{10}	1.9
130	0.16	5.3x10^{10}	1.4x10^{12}	2.3x10^{10}	4.6
250	0.15	9.3x10^{10}	1.4x10^{12}	2.3x10^{10}	8.0
400	0.15	1.5x10^{11}	1.4x10^{12}	2.3x10^{10}	13.1
800	0.14	2.8x10^{11}	1.4x10^{12}	2.3x10^{10}	24
1.5x10^3	0.099	3.7x10^{11}	1.4x10^{12}	2.3x10^{10}	32
3.0x10^3	0.068	5.1x10^{11}	1.4x10^{12}	2.3x10^{10}	44

Table V-4

Evolution of the density of carriers (σ) created in the InGaAs layer as a function of nonresonant excitation intensity (P_{exc}). Column f gives the fraction of the energy that is converted into carriers trapped in the InGaAs layer, D_{QW} gives the number of states available per cm^2 in a quantum well, D_{QD} gives the number of states available in the ground state of a population of quantum dots with the same areal density as the Island density of sample IR, and finally N_D gives the average number of carriers contained in a given quantum dot at any time. Absorption coefficient of 1.0x10^5 cm^{-1}, carrier lifetime of 1.0 ns and interlevel separations of 50 meV were assumed.

by two orders of magnitude for a quantum well compared to a quantum dot layer.

In order to relate the level of excitation used in our experiments to D_{QW} and D_{QD}, an estimate of the average carrier density (σ) created in the strained InGaAs layer is calculated. The integrated PL intensity (I_{out}) of each spectrum in Figure V-5 is assumed to be proportional to the fraction "*f*" of carriers captured in the layer, and that for a very low

intensity "f" can be estimated from optical constants given in the literature[79] and shown in table V-5.

E_{exc} (eV)	n	k	$\alpha(cm^{-1})$	R
2.54	4.2	0.43	$1.0x10^5$	0.38

Table V-5

Optical parameters for GaAs used to evaluate the absorption in sample IR under CW excitation.

where E_{exc} is the excitation energy of the laser, n and k are respectively the real and imaginary part of the refractive index, and α is the absorption coefficient in GaAs at E_{exc}. From these parameters a reflection of 38% at the sample surface is obtained. Next, using the absorption coefficient the remaining intensity at the strained layer and at midpoint between the two InGaAs layers is obtained. Assuming that the island layer captures the electron-hole pairs created in the GaAs barrier betwen these two points (see inset of Figure V-7), and that carriers created in the cap layer recombine non-radiatively before they can be captured, one concludes that for low excitation 19% of the incident radiation is transformed in carriers that will fall in the strained layer. Therefore f is set equal to 0.19 at the lowest excitation intensity (3.7 μW), as can be seen in Table V-4. Figure V-7 shows the wavelength integrated radiated output power as a function of the incident excitation intensity. At high intensities, the relationship between P_{exc} and I_{out} ceases to be linear, and clearly f can not be considered independent of the laser excitation power. A correction for this non-linearity can be calculated assuming that the total radiated power from the

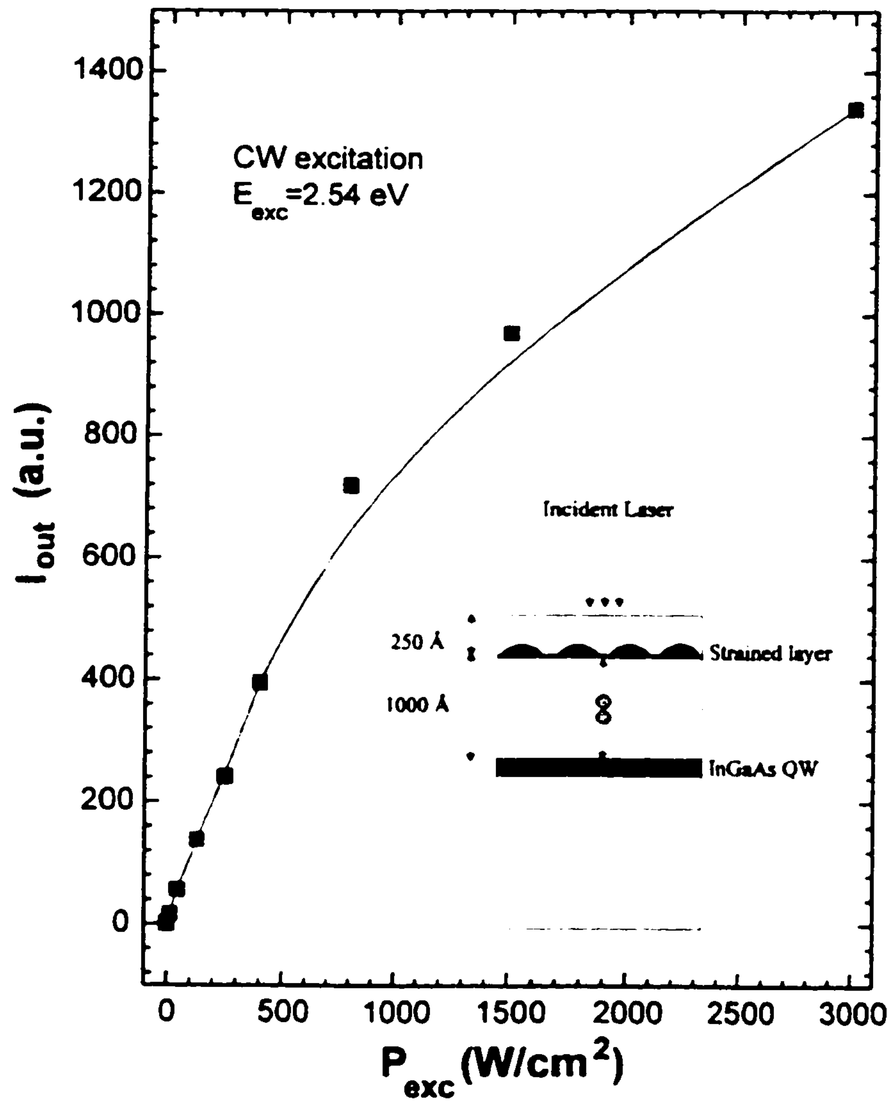

Figure V-7

Integrated radiation intensity output of the sample as a function of excitation power intensity; the line is a guide to the eye. The inset shows the structure of the sample and the limit of the carrier capture regions for both InGaAs layers present in the sample.

strained layer is proportional to both the excitation intensity and the fraction of carriers captured, $I_{out}(P_{exc}) \propto P_{exc} \bullet f(P_{exc})$. Using the result for 3.7 μW as a reference, the effective fraction captured can be estimated as

$$f(P_{exc}) = \frac{I_{out}(P_{exc})}{I_{out}(3.7\mu W)} \frac{3.7\mu W}{P_{exc}} f(3.7\mu W) \qquad \text{V-16}$$

where f is the fraction of the total carrier population created that is captured in the island layer, I_{out} is the integrated intensity emitted from the island layer, P_{exc} is the laser excitation power and $f(3.7\mu W)$ is given by 0.19. The resulting values of f are presented in Table V-4. Finally σ, the average areal carrier density created in the layer, is obtained by computing the product $\Phi(P_{exc})\tau$, where $\Phi(P_{exc})$ is the carrier generation function given by $\Phi(P_{exc}) = \frac{P_{exc}}{E_{photon}} f(P_{exc})$ with E_{photon} the energy of each individual photon in the laser beam, and τ is the carrier lifetime in the dots. The latter is estimated at 1.0 ns as will be shown by the time-resolved experiments presented later in this chapter. By comparing columns 3 and 4 in Table V-4, it can be seen that even at the highest excitation intensity, the number of carriers generated is clearly insufficient to saturate the conduction band ground state of a quantum well.

Also, dividing σ by the island areal density, one can obtain N_D, the average number of electron-hole pairs per dot present in the layer at any given time. This quantity is listed in the last column of Table V-4. From these numbers, it is seen that the twofold degenerate ground state of the dots become saturated at P_{exc} = 45 W/cm^2. The next state is fourfold degenerate and becomes saturated at an excitation intensity of 250 W/cm^2, and so on until the 30 available electron-hole states become completely saturated for an excitation intensity of 1.5 kW/cm^2. Clearly, the excitation levels used here are consistent with saturation effects in a quantum dot layer and completely inconsistent with saturation effects in a quantum well layer (monolayer fluctuations). After complete saturation has

been reached (i.e 30 carriers per dot are created), excess carriers are simply forced to dwell in unbound states such as the wetting layer states.

The detailed temperature dependence of the PL emission spectrum, in the high optical excitation regime (where higher energy lines can be observed), was obtained and the evolution of the emission spectrum is shown in Figure V-8. It is clear from the figure that as the temperature is increased, the number of high energy satellites is reduced. This quenching effect starts with the highest energy peak and progressively moves towards the lower lying peaks as the temperature is increased, such that at T=225K, only the low energy n=1 transition can be observed. This temperature dependence is typical of electron-hole pairs localized in deep confining potentials with excited states. For excitons localized in shallow minima originating from ML fluctuations, one would expect the lower energy transitions to be quenched at much lower temperatures depending on the localization potential (typically a few tens of Kelvins[80]). It should also be emphasized that a PL signal was detected up to room temperature with a modest excitation power density of 200W/cm^2. This is a clear indication that Stranski-Krastanow growth is capable of producing QDs of very high optical quality with very few nonradiative recombination sites present. The red shift observed as the temperature is increased reflects the reduction of the bandgap with temperature. The quenching effect observed at high temperatures can be understood simply by the thermionic emission of the photocarriers out of the QD into the wetting layer material. From the calculation of section V.1, the energy difference between

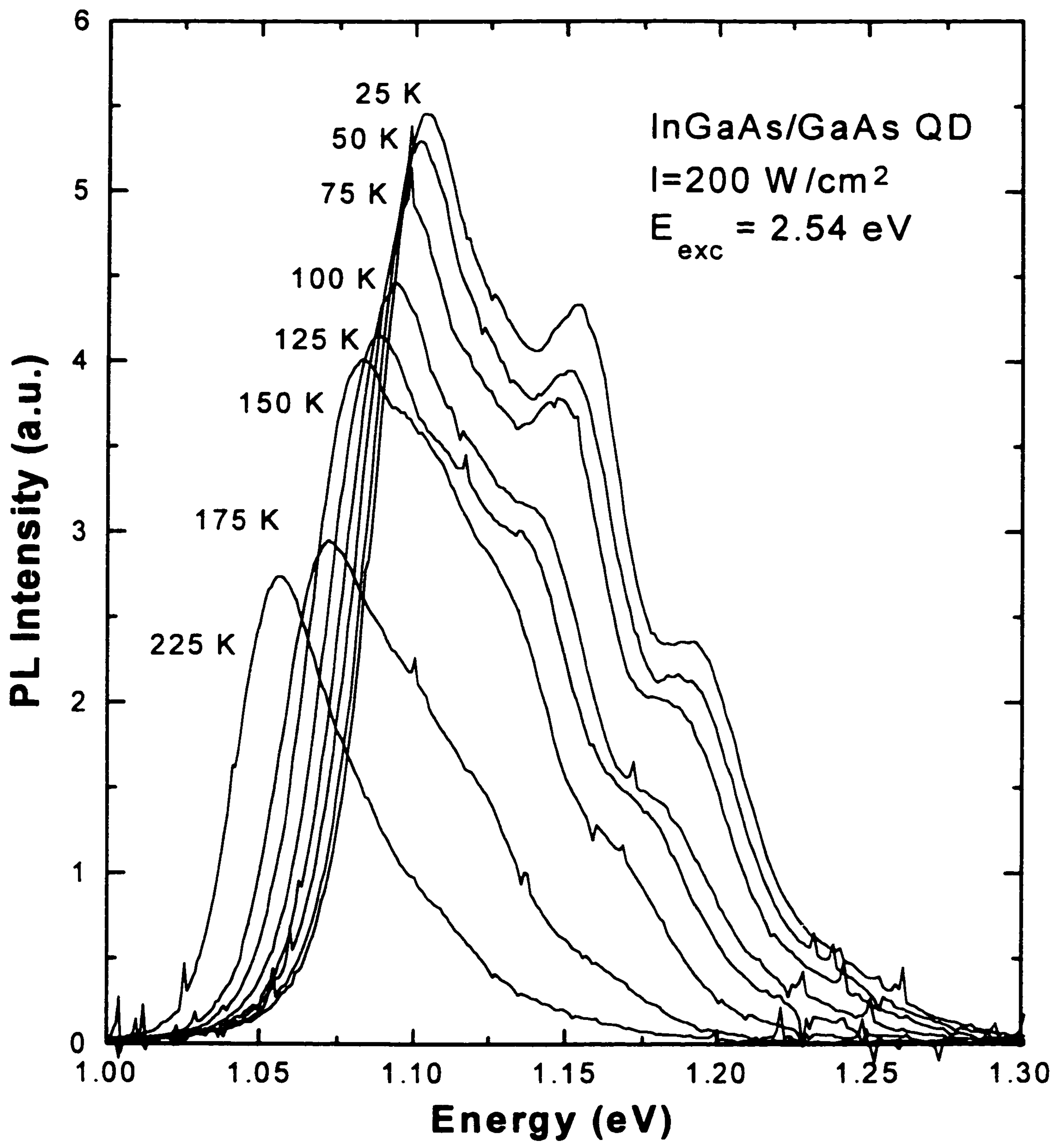

Figure V-8

Evolution of the emission spectrum as a function of sample temperature.

the various levels and the wetting layer continuum ("activation energy") are: $\Delta E_{1\text{-wl}} \sim 249$ meV, $\Delta E_{2\text{-wl}} \sim 207$ meV and, $\Delta E_{3\text{-wl}} \sim 165$ meV. Therefore, a deeper confinement clearly leads to thermal quenching at higher temperature.

To summarize the CW excitation PL results, the transition energy spacing observed is consistent with excited state emission of quantum dots, the excitation power densities used are consistent with saturation effects in a quantum dot layer as opposed to a quantum well layer, and the successive quenching of the transition lines as a function of temperature is consistent with excited state emission from an ensemble of quantum dots.

V.2.2 Pulsed excitation

For emission originating from quantum dot excited states, the luminescence intensity of each line depends on two main factors: the subband degeneracy and the inter-sublevel dynamics. Changing from CW to pulsed excitation conditions is expected to have an effect on the carrier dynamics for different reasons. For example, exciting the sample with high peak power short laser pulses can create a high density electron-hole plasma in the wetting layer. It has been shown that such a 2D electron-hole gas in the vicinity of a quantum dot can affect the inter-sublevel dynamics by means of Auger interactions[81]. This is a situation similar to the one presented in Figure IV-6. Also, irrespective of the dominant relaxation process, in CW operation the carriers lost by radiative recombination are replenished by the constant flow of new carriers created. In contrast, for pulsed excitation the initial population is allowed to decay completely so that each dot becomes empty before its

carrier population is replenished. Each situation gives rise to different results.

The PL experiments presented in Figure V-5 were repeated using a mode-locked YAG pumped dye laser system as an excitation source, with 10 ps laser pulse impinging on the sample at a repetition rate of 76 MHz. Figure V-9 shows the intensity dependence of the PL spectrum obtained under these excitation conditions. Once again, the emergence of higher energy emission is observed as the excitation intensity is increased.

In order to verify if the excitation levels used are consistent with saturation of quantum dot states, the carrier density created in the dot layer is calculated following the method used for CW excitation. The following optical parameters found in the literature[79] are used

E_{exc} (eV)	n	k	$\alpha(cm^{-1})$	R
1.968	3.5	0.12	$3.5x10^4$	0.31

Table V-6

Optical parameters of GaAs used to evaluate the absorption in sample IR under pulsed excitation.

where the same symbol definitions as before are used. Figure V-10 shows the integrated PL intensity as a function of average excitation power for pulsed excitation. There is again evidence of saturation in the fraction of carriers captured and this effect can be corrected in the same fashion as described earlier. The capture efficiencies (f) thus obtained are listed in Table V-7, along with the corresponding excitation powers. It is worth noting that the populations created by two consecutive pulses will not overlap since the carrier lifetime (~1.0 ns) is much shorter than the repetition time of the laser (~13 ns).

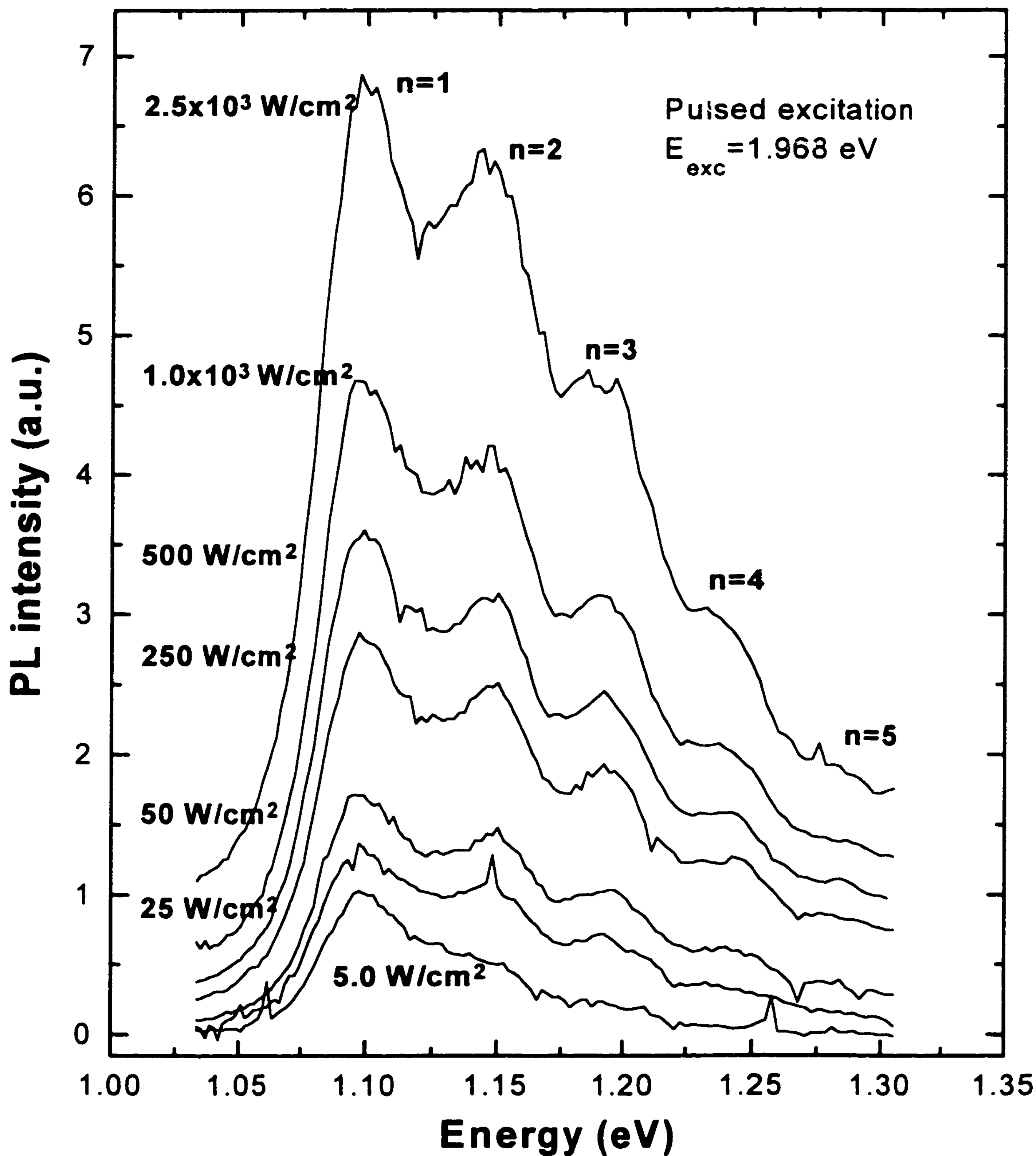

Figure V-9

Evolution of the low temperature (4 K) emission spectrum with the excitation intensity for pulsed excitation. The laser energy was set at 1.968 eV with a repetition rate of 76 MHz and pulsewidth of ~10 ps.

Significant information is therefore contained in σ_p, the carrier density created per pulse, and in N_{PD}, the average number of carriers created per pulse per dot. Both quantities are listed in Table V-7 as a function of average excitation power. As can be seen from the results listed, for all excitation intensities studied here, the carrier density created by a laser pulse is less that the density of states available for the ground state of a quantum well. However, from these calculations it is predicted that the quantum dot ground state

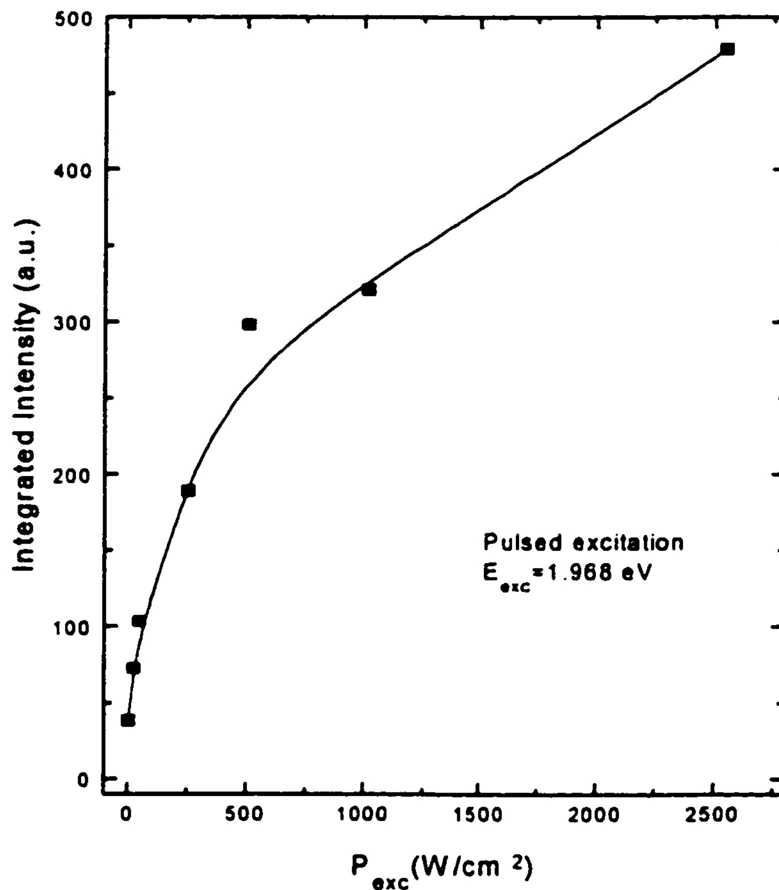

Figure V-10

Integrated sample output intensity as a function of average excitation power for pulsed excitation. The line is a guide to the eye.

P_{exc}(W/cm^2)	f	σ_p(cm^{-2})	D_{QW}(cm^{-2})	D_{QD}(cm^{-2})	N_{PD}
5.1	0.101	2.2x10^{10}	1.4x10^{12}	2.3x10^{10}	1.8
25	0.038	4.0x10^{10}	1.4x10^{12}	2.3x10^{10}	3.5
50	0.027	5.7x10^{10}	1.4x10^{12}	2.3x10^{10}	4.9
255	0.010	1.1x10^{11}	1.4x10^{12}	2.3x10^{10}	9.1
510	0.0066	1.4x10^{11}	1.4x10^{12}	2.3x10^{10}	12.0
1.0x10^3	0.0042	1.8x10^{11}	1.4x10^{12}	2.3x10^{10}	15.4
2.5x10^3	0.0025	2.7x10^{11}	1.4x10^{12}	2.3x10^{10}	22.8

Table V-7

Evolution of the density of carriers (σ_P) created by each pulse in the strained InGaAs layer as a function of excitation intensity (P_{exc}). Column f gives the fraction of the energy that is converted into carriers trapped in the layer, D_{QW} gives the number of states available per cm^2 in a quantum well, D_{QD} gives the number of states available in the ground state of a population of quantum dots with the same areal density as the Island density of sample IR, and finally N_{PD} gives the average number of carriers per dot reaching the layer after each pulse.

should become saturated for excitation intensities of 25W/cm^2 and higher. Thus, the results presented in Table V-7 are consistent with an interpretation in terms of quantum dot emission. This confirms the conclusion reached with the steady-state excitation PL measurements.

So far, the saturation effects observed in the PL spectra obtained from CW and pulsed excitation experiments have been discussed separately. In the following section, the two series of experiments are compared and a detailed analysis in terms of state-filling dynamics is presented.

V.2.3 Modeling of the PL results: state-filling

When comparing the results of CW excitation (Figure V-5) with the results of pulsed excitation (Figure V-9), two striking differences can be observed: **1**- In the case of pulsed excitation, the amplitude of an excited state peak never becomes higher than that of a lower level, and the ground state emission remains strongest at all excitation intensities. **2**- excited state emission is observed for lower average excitation powers in the pulsed case. For example, the 25 W/cm^2 spectrum in Figure V-9 clearly shows emission from the first three levels, while a comparable spectrum, obtained for 14 W/cm^2 and presented in Figure V-5, shows negligible excited state emission.

The second observation can be explained in the following way. For a similar average excitation intensity, the time average number of carriers created in a dot should be similar for both experiments. However, in the pulsed excitation case all carriers that would have been created over a period of 13 ns are now created within 10 ps, before radiative recombination takes place. This causes higher excited states to be occupied in view of Pauli's exclusion principle. This explains why excited state emission is observed for lower average excitation powers in the pulsed case.

In order to explain the first observation, a model of the carrier dynamics is developed that will allow us to compare the relative intensities of the emission lines for both PL experiments. In the discussion that follows, it is assumed that the inter-sublevel relaxation rate is infinite (i.e. $\gamma_{ISL} = \infty$) so that the carriers in the dot relax instantaneously to the lowest energy configuration. An example of such a configuration is shown in Figure

V-11 for a dot filled with 9 electron-hole pairs. In the case of non-resonant excitations studied here, the electrons and holes are created in the barrier region. The carriers will then diffuse near a quantum dot with a time τ_D and get captured at a rate given by γ_C. Since one expects the relaxation time of the carriers to increase with the energy difference between the initial and final states[82], carriers are more likely to first enter the dot by occupying the highest excited state, and then relax to the ground state in a sequential way. In this case, one would expect to observe excited state luminescence at low excitation power, which is not the case as seen in Figure V-5. This can be explained if the inter-sublevel relaxation rate is much faster than the radiative recombination rate. Indeed, the luminescence intensity for a given excited state is proportional to $\gamma_{RAD}/(\gamma_{ISL}+\gamma_{RAD})$. This factor becomes negligible if $\gamma_{RAD}<<\gamma_{ISL}$, and excited state luminescence can be observed only if γ_{ISL} is comparable to γ_{RAD}. Since no excited state emission is observed at low excitation intensities, the above condition is believed to be true in empty quantum dots, which justifies the approximation $\gamma_{ISL}\sim\infty$. Also, based on Pauli's exclusion principle this relaxation rate is set to zero when all the states at lower energies are occupied. The above assumptions define the state-filling approximation.

The CW excitation experiment is first modeled in this limit. Defining I_i as the number of e_i-h_i recombination observed per second, one has

$$I_i = \sum_{r=1}^{30} I_i^r N_r \qquad \text{V-17}$$

where the sum extends up to a maximum carrier population of 30 (see Figure V-4), I_i^r is the number of e_i-h_i recombination observed given the dot contains "r" electron-hole pairs

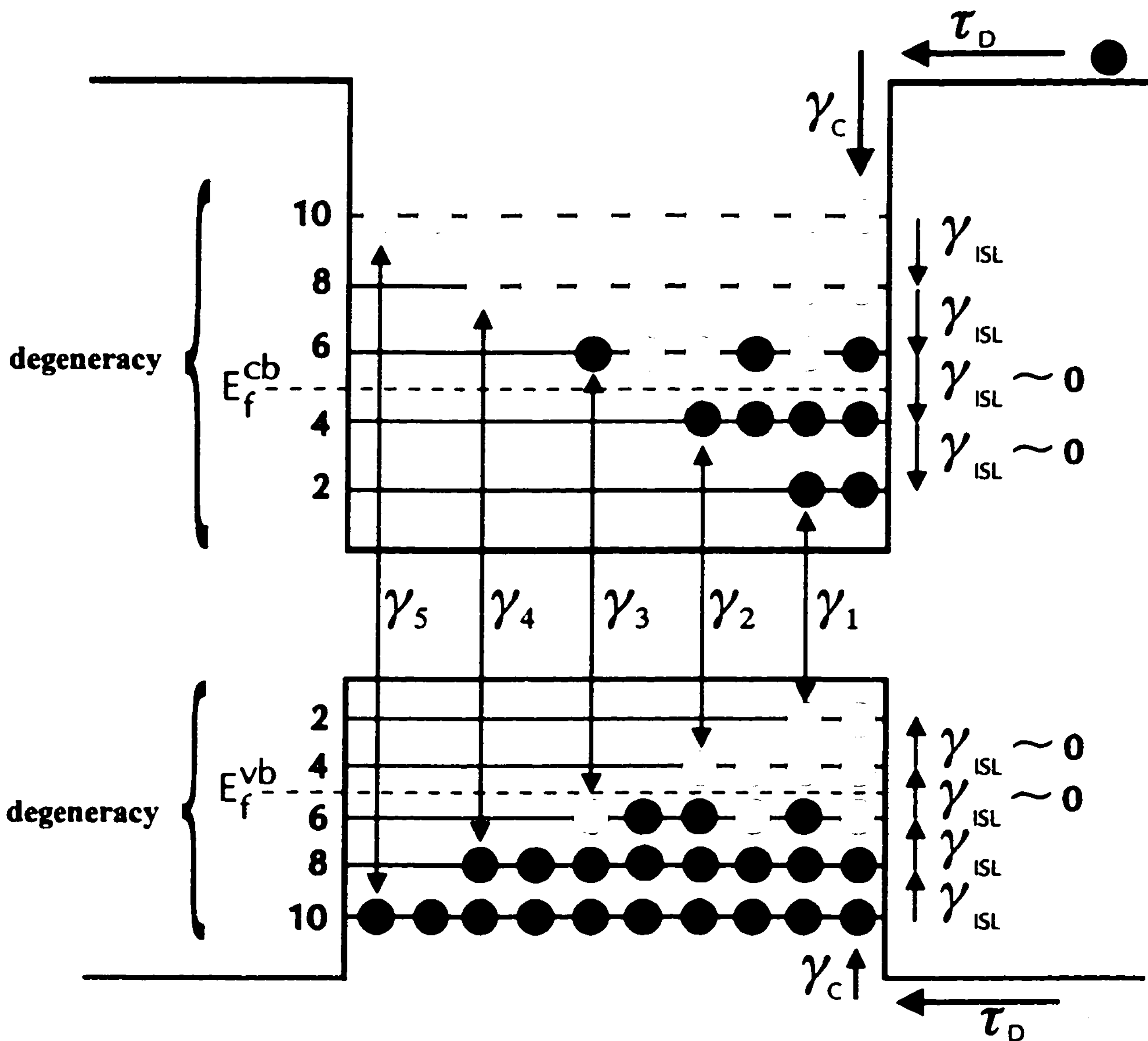

Figure V-11

Schematics of a typical InGaAs quantum dot filled with 9 electron-hole pairs. The γ_i are the radiative recombination rates for a pair in level i, while γ_{ISL} represents the inter-sublevel relaxation rate. Each filled circle stands for a state occupied by an electron, while open circles represent holes.

and N_r is the total number of dots containing "r" pairs in the ensemble probed. To estimate N_r the only available quantity is N_D, the average number of pairs per dot. Assuming the probability of a particular dot to contain n pairs can be calculated from a

known distribution around a mean N_D, equation V-17 can be written as

$$I_i(N_D) = \sum_{r=1}^{30} I_i^r\left(P_r^{N_D} N_{dot}\right) \qquad \text{V-18}$$

where $P_r^{N_D}$ represents the probability of a given dot to contain n pairs given an average of N_D pairs per dot, and N_{dot} is the total number of dots probed. I_i can therefore be calculated assuming one can estimate $P_r^{N_D}$ and I_i^r in a way that is consistent with the conditions of a steady state excitation.

The probability distribution function $P_r^{N_D}$ is obtained by considering that at any instant it maps a binomial distribution obtained when one throws a total of N (= $N_D * N_{dot}$) objects in N_{dot} boxes, with the objects having an equal probability of falling in any box. Thus

$$P_r^{N_D} = \frac{(N_D * N_{dot})!}{r!(N_D * N_{dot} - r)!}\left(\frac{1}{N_{dot}}\right)^n\left(1 - \frac{1}{N_{dot}}\right)^{(N_D * N_{dot} - r)} \qquad \text{V-19}$$

and in the limit $N_{dot} \to \infty$, this reduces to a Poisson distribution and one obtains[83]

$$P_r^{N_D} = \frac{(N_D)^r}{r!}e^{-N_D} \qquad \text{V-20.}$$

Note that this distribution is not defined for r<0 which is consistent with the fact that a dot cannot contain a negative number of carriers.

Next, the definition of I_i^r is based on the fact that the number of photons emitted from a given e_i-h_i transition is given by the number of electron-hole pairs in level *i* times a constant radiative recombination rate γ_i. The matrix elements I_i^r is simply given by

$$I_i^r = \gamma_i N_i^r \qquad \text{V-21}$$

where N_i^r is the number of electron-hole pairs in level i and can be determined as follows for a dot filled with r pairs:

$$N_i^r = \begin{cases} 0 & if \quad r \le \sum_{k=0}^{i-1} g_k \quad a) \\ g_i & if \quad r \ge \sum_{k=0}^{i} g_k \quad b) \\ \left(r - \sum_{k=0}^{i-1} g_k\right) & otherwise \quad c) \end{cases} \qquad \text{V-22}$$

where g_i is the degeneracy of the ith energy level, and $g_0 = 0$ has been introduced so that this definition of N_i^r can be applied to the ground state. As an example of how to use equation V-22, consider the situation of Figure V-11 where n=9, g_1=2, g_2=4, g_3=6. In this case the ground state is completely filled since (n=9) > (g_0+g_1 = 0+2) (i.e. condition b is true) and $I_1^9 = \gamma_1 N_1^9 = \gamma_1 g_1$. The first excited state is also completely filled since (n=9) > (g_0+g_1+g_2 = 0+2+4) and $I_2^9 = g_2\gamma_2$. The second excited state is only half filled as there are only three pairs left after filling the first two levels, while 6 states are available and therefore $I_3^9 = 3\gamma_3$. The fourth and fifth confined levels are empty and $I_4^9 = I_5^9 = 0$. Thus, equation V-21 combined with the set of rules V-22 allow us to determine the radiated intensities for each transition considered, provided the radiative recombination rates (γ_i) are known. To determine these parameters precisely, time-dependent experiments are necessary, and results of such experiments are presented in the next section. However, as will be explained shortly, only an estimate for γ_1 is obtained while other rates remain unknown. As a starting point, for this discussion it is simply assumed that the e_i-h_i

radiative recombination rates are equal for all i.

In the case of the pulsed excitation experiments, one can consider that the effect of each pulse is independent, as mentioned before. An equation analogous to V-17 can therefore be expressed as

$$I_i = R\sum_{r=1}^{30} I_{ip}^r N_r \qquad \text{V-23}$$

where I_i is the the number of e_i-h_i recombination observed per second, R is the laser repetition rate, I_{ip}^r is the number of e_i-h_i recombinations observed per pulse in a dot filled with r pairs, and N_r is the number of dots filled with r pairs after each laser pulse. Expanding N_r as before one gets

$$I_i = R\sum_{r=1}^{30} I_{ip}^r \left(P_r^{N_{PD}} N_{dot}\right) \qquad \text{V-24}$$

where $P_r^{N_{PD}}$ is the probability of having a dot filled with r pairs given an average of N_{PD} pairs per pulse per dot are created in the layer, and N_{dot} is the total number of dots probed.

The definition of $P_r^{N_{PD}}$ is obtained by considering that for each pulse impinging on the sample, one distributes randomly N ($= N_{PD} * N_{dot}$) pairs in N_{dot} boxes. This problem is similar to the one considered in the steady state excitation case with N_{PD} replacing N_D. Thus, $P_r^{N_{PD}}$ is given by

$$P_r^{N_D} = \frac{(N_{PD})^r}{r!} e^{-N_{PD}} \qquad \text{V-25.}$$

The calculation of the matrix elements I_{ip}^r is more complex in the case of pulsed

excitation. Here, one cannot consider the number of dots with population n to remain constant since each dot is allowed to empty itself completely before the next carrier supply arrives. Let us consider one of these dots filled with r pairs shortly after a pulse reaches the sample surface. A few instants later, a number of carriers have recombined radiatively (non-radiative decay is neglected in view of the results of Figure V-8) leaving only k electron hole pairs in the dot. The probability of the next event to be an e_i-h_i recombination is given by $Q_i^k = N_i^k/k$, the proportion of pairs in level i, and the total number of e_i-h_i recombination is therefore given by

$$I_{ip}^r = \sum_{k=1}^{r} Q_i^k = \sum_{k=1}^{r} \frac{N_i^k}{k} \qquad \text{V-26}$$

where one has to sum the number of photons emitted from level i for all successive total populations until the dot is empty. For example, in the situation presented by Figure V-11 the first recombination event might produce a photon of energy E_1, E_2 or E_3 with probabilities of $Q_1^9 = 2/9$, $Q_2^9 = 4/9$ and $Q_3^9 = 3/9$ respectively. The next event produces a photon of similar energies with probabilities $Q_1^8 = 2/8$, $Q_2^8 = 4/8$ and $Q_2^8 = 2/8$ and so on. One obtains

$$I_{1p}^9 = \frac{2}{9}+\frac{2}{8}+\frac{2}{7}+\frac{2}{6}+\frac{2}{5}+\frac{2}{4}+\frac{2}{3}+\frac{2}{2}+\frac{1}{1} = 4.66$$
$$I_{2p}^9 = \frac{4}{9}+\frac{4}{8}+\frac{4}{7}+\frac{4}{6}+\frac{3}{5}+\frac{2}{4}+\frac{1}{3}+\frac{0}{2}+\frac{0}{1} = 3.62$$
$$I_{3p}^9 = \frac{3}{9}+\frac{2}{8}+\frac{1}{7}+\frac{0}{6}+\frac{0}{5}+\frac{0}{4}+\frac{0}{3}+\frac{0}{2}+\frac{0}{1} = 0.73$$

Using a similar method the matrix elements I_{ip}^r can be calculated, and using definition V-25 for $P_r^{N_{PD}}$ one can compute the intensities of emitted photons with equation V-24.

The results of the calculations for both the CW and pulsed excitation case are presented in Figure V-12 for average populations of 20 pairs or less per dot. In the case of steady state excitation one can see that the ground state and first excited state are expected to show absolute saturation of their emission intensities for populations of 3 pairs per dot and 8 pairs per dot respectively. This effect is not observed in the actual experiment even for average populations much higher than those included in the calculation, as can be seen in Figure V-13a. In the calculation it was assumed that the dot population is excited uniformly. In real experiments, the gaussian profile of the laser beam will always create an increasing number of carriers in the tail of the beam profile where the dots are not filled, and this prevents the absolute saturation of the luminescence as a function of intensity. Also, carriers created in a region where all dot states are occupied can diffuse laterally and eventually be trapped in an empty dot at the edge of the beam profile. This means that an ever increasing dot population is probed as the excitation intensity is increased. Again, this effect prevents absolute saturation of the emission. Finally, the inter-sublevel relaxation rate should become slower as the number of states available in the lower level decreases. If the slower rate becomes comparable to the radiative rate, a situation is reached where the average number of carriers in a lower level scales with the total number of carriers in the dot, thus preventing an absolute saturation of the emission.

Comparing the relative emission intensities at N_D=44 in figure V-13a, it can be seen that the e_2-h_2 and e_3-h_3 lines have similar intensities, as well as the e_1-h_1 and e_4-h_4 transitions, while e_5-h_5 is the weakest emission line. This situation is similar to the one

predicted for an average population of 12 electron-hole pairs per dot, as presented in Figure V-12a. Therefore, it seems that the capture ratio has been overestimated. The biggest source of error in the calculation of *f* is the capture range which was arbitrarily set at midpoint between the dot layer and the quantum well. This range depends on the diffusion length and might in fact not extend this far from the quantum dot layer. An error of a factor of three would correspond to a capture range of about 14 nm.

In Figure V-12a one can see that ground state emission is expected to be dominant for an average number of dots of 3.5 or less. Above 3.5 the first excited state shows strongest emission until the second excited state reaches the same level of emission at 11 carriers per dot. This successive importance of one of the emission lines is also observed in Figure V-13a and is typical of a state-filling effects. Each time a level is filled, excess carriers are forced to dwell in higher states causing the emergence of a new emission line.

Inspecting Figure V-13b it can be seen that in the pulsed case the emission of an excited state never becomes stronger than that of a lower level. This is in contrast with the case of steady state excitation and is in good agreement with the calculations. The model qualitatively predicts the observed evolution for excitations up to 15 carriers per dot at which point a discrepancy may be observed from the fact that the emission of the first excited sate is expected to exceed that of the ground state. This inaccuracy suggests that the recombination rate of the excited state is lower than that of the ground state. This is consistent with the observation that the relative intensity I_1/I_2 observed in Figure V-13a tends to approach a ratio greater than $g_1/g_2 = 1/2$. Also, the calculation predicts almost

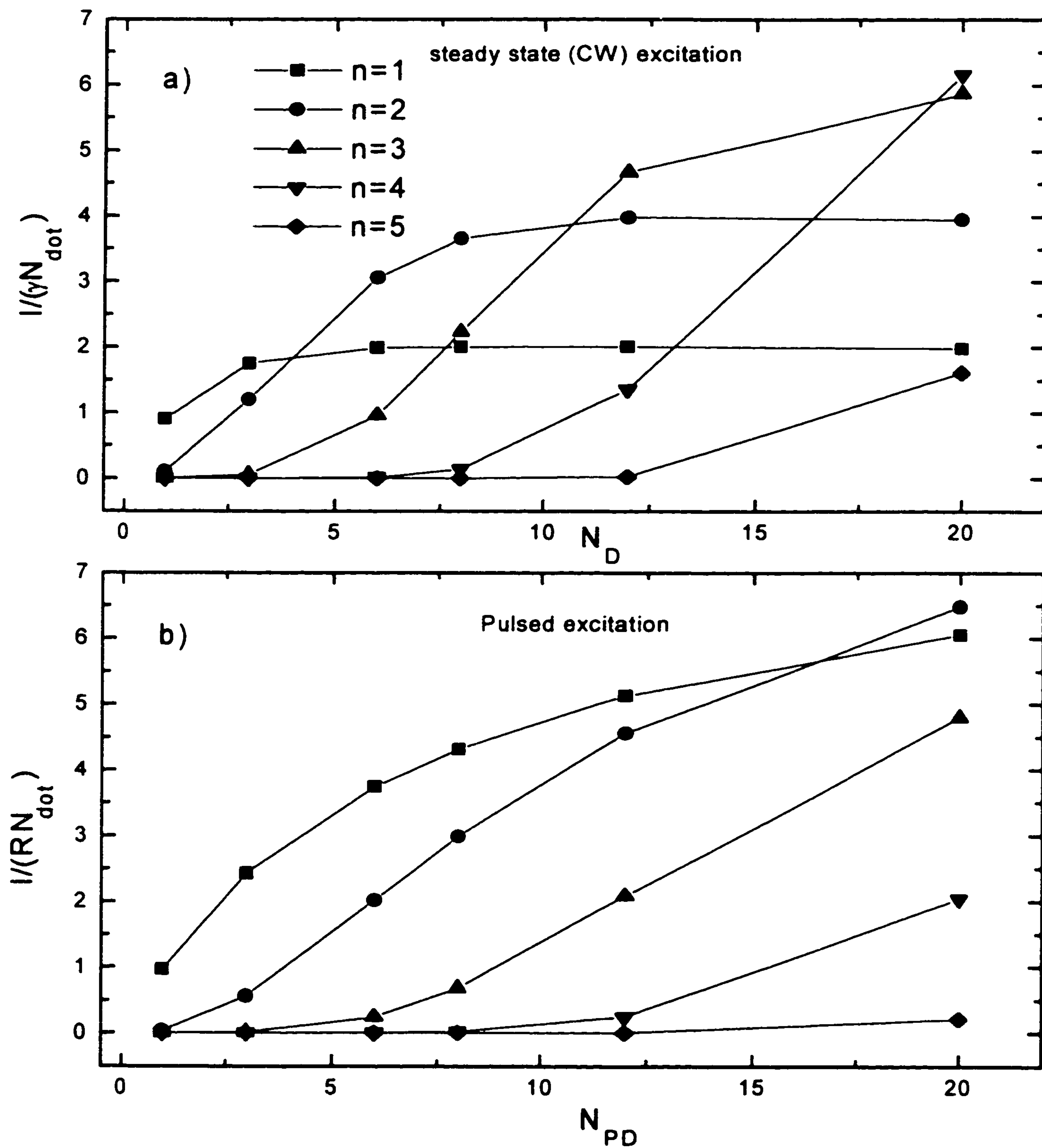

Figure V-12

Calculated emission intensities for the transition lines observed in sample IR as a function of a) average dot population for steady state excitation, and b) average number of pairs per dot per pulse created.

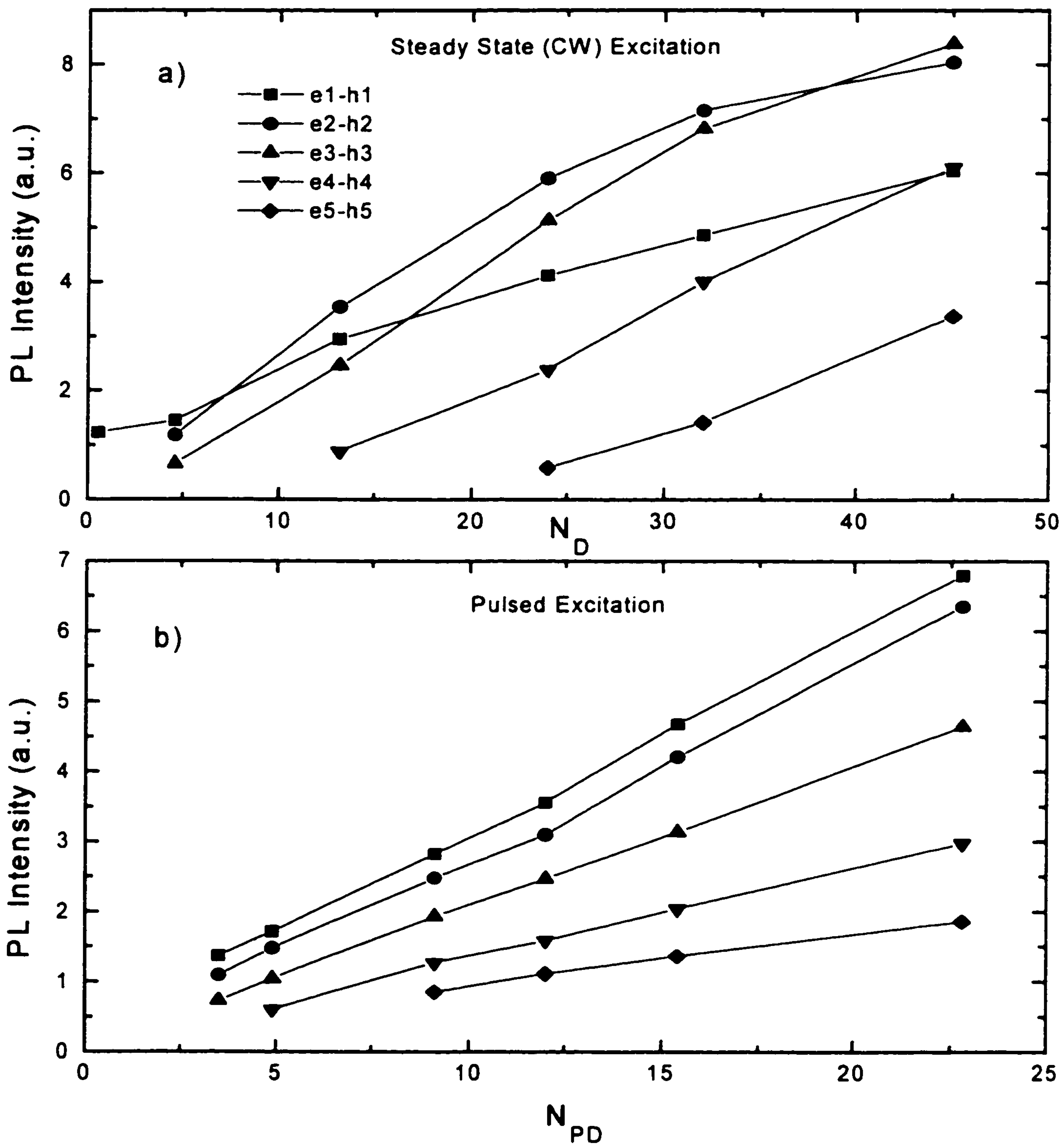

Figure V-13

Measured emission intensities for the transition lines of sample IR as a function of a) average dot population for steady state excitation, and b) average number of pairs per dot per pulse created.

no emission from a transition unless the lower levels are filled. In the actual experiment however, higher level emission is observed for occupation numbers much lower than those necessary to completely fill the lower levels. For example, consider e_4-h_4 emission in Figure V-13b for which the emission is significant for N_{PD}=12 whereas it should be almost negligible according to Figure V-12b. This observation is consistent with restricted inter-sublevel transfer rates when the number of final states available decreases.

The discussion of section V-2 can be summarized as follows:

1- The transition energy spacing observed are consistent with an ensemble of quantum dots.

2- The progressive rise of higher energy lines is inconsistent with segregated inhomogeneous broadening of any type.

3- The excitation power densities used for the CW PL experiments are consistent with saturation effects in a layer of quantum dots.

4- The temperature dependence of the PL spectrum is inconsistent with a QW layer with ML fluctuations.

5- The comparison of transition intensitites as a function of excitation power for PL spectra obtained with CW and pulsed excitation is consistent with a simple state-filling model, with possible restricted inter-sublevel transfer rates before the dots become completely filled.

V.3 Time-Resolved Photoluminescence

As discussed in section V-2, all of the observations extracted from the experimental results can be explained in terms of state-filling dynamics. This section presents time-resolved experiments on sample IR to probe the dynamics of carrier relaxation more directly.

The measurements are performed using the up-conversion set-up of Figure III-4. The sample was excited using a YAG pumped dye laser system with the laser energy set at 1.968 eV. During each experiment the sample was kept at 4.2 K. The $LiIO_3$ crystal allowed phase matching over a range of ~20 meV so that each individual peak was monitored in separate successive experiments using the method presented in chapter III.

The time-dependent trace for each PL peak is shown in Figure V-14 for an average excitation intensity of 50 W/cm^2. The decay part of each curve was empirically fitted to a single exponential function of the form $Ae^{-t/\tau}$ in order to extract a decay time constant. The ground state as well as the first and second excited state do not seem to show a single exponential decay, but for the dynamic range permitted by the experiment, deviations from the trial function were small. The same procedure was applied for two other excitation intensities, namely 5 W/cm^2 and 1.3×10^3 W/cm^2.

The time decay constants thus obtained are summarized in Figure V-15. From these results, one concludes that the decay time of a given luminescence peak speeds up as

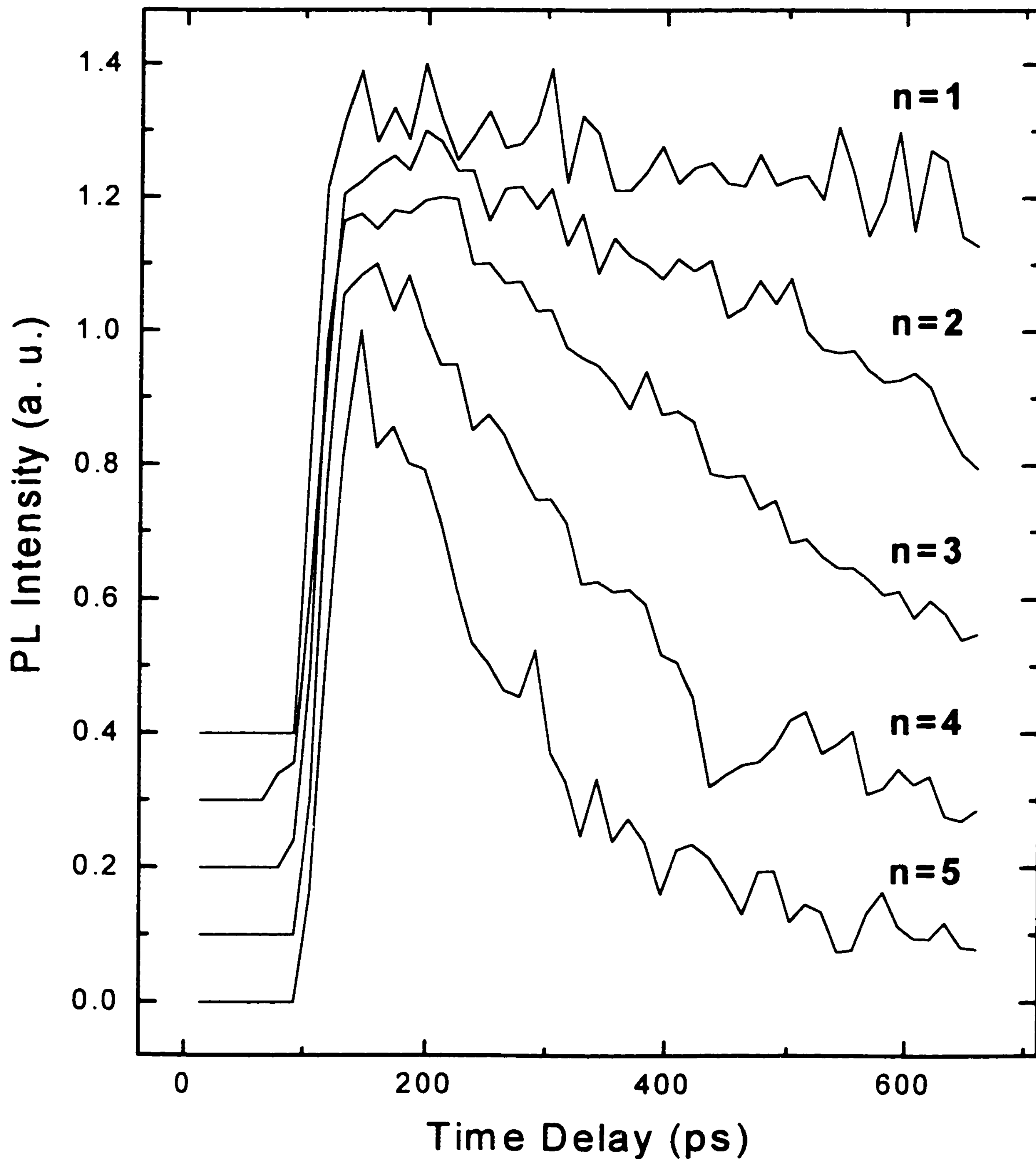

Figure V-14

Time decay of the various transitions obtained by up-conversion at 4 K. The experiment monitors an energy bandwith of ~20 meV centered on the peaks presented in Figure V-9. A constant offset was added to some of the curves for clarity.

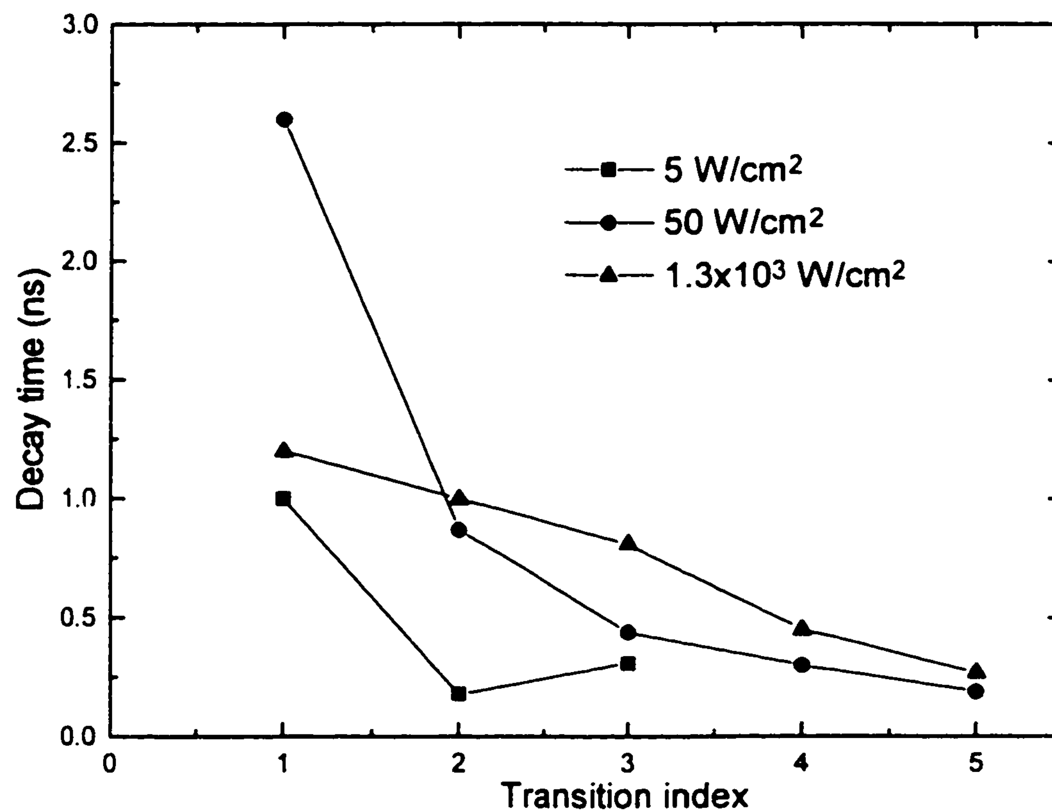

Figure V-15

Summary of the decay time constants obtained for the various transitions (n=1 to n=5) at different excitation power densities.

higher energy lines are probed and as the intensity of excitation is decreased. These observations are consistent with state filling effects in a quantum dot supporting a number of excited states. In this approximation, the photocarriers are quickly captured in quantum dots and relax to the lowest energy configuration (see Figure V-11). After this initial step, and neglecting non-radiative recombination, the carriers can relax either by radiative recombination or inter-sublevel relaxation, except for carriers in the ground state which can decay by radiative recombination only. When a recombination event occurs, it creates

an empty state. This empty state is eventually filled by a carrier coming from a higher energy level, which in turn leaves an empty state in this higher level. This cascade stops when the highest occupied level loses a carrier which cannot be replaced. Thus the state filling effect explains the temporal behavior observed, i.e. shorter decay times for higher levels. Also, the non-single exponential decay of lower energy levels is caused by the constant supply of carriers coming from higher states.

From the above discussion, the cascade observed in Figure V-14 implies a carrier transfer between the different states. For segregated inhomogeneous broadening of the type shown in Figure V-6c, a transfer of carriers between the different families of islands cannot be achieved[78]. Therefore, any interpretation of the results in terms of segregated inhomogeneous broadening has to be rejected for sample IR.

The excitation intensity dependence can be understood if one assumes that the relaxation rates are reduced as the number of available states in lower levels decreases. For lower exciton intensities the average occupation probability of a given state decreases, and the number of decay channels available for carriers in excited states becomes higher, hence the observed decay times are shorter.

According to the numbers of Table V-7, at 5 and 50 W/cm^2 the average initial population of a quantum dot is 1.8 and 4.9 electron-hole pairs respectively. Therefore, in the case of low excitation power densities, some of the excited states are initially empty. In this case the decay time of the highest occupied level approaches the inter-sublevel relaxation time. For 5 W/cm^2 excitation, the decay time of the n=3 level is 310 ps, and if one considers a sequential picture in which carriers can only decay to the next lowest

level, this time is an estimate of the n=3 to n=2 inter-sublevel relaxation time. With the above interpretation, the experimental rise times are also expected to become slower as the excitation intensity is increased. However, defining the rise time as the time necessary to increase the luminescence intensity from 10% to 90% of the maximum, all rise times are found to be equal within the experimental resolution (35±10 ps).

As the excitation intensity is lowered one expects the carrier refill to become negligible, even for the ground state. For an excitation power density of 5 W/cm^2, table V-7 gives an average dot population of 1.8 electron-hole pairs, which means that for this excitation level the ground state is not saturated. The decay time observed in this condition suffers from little refill from higher states, and is attributed entirely to n=1 radiative recombination events. The value of τ_1 is therefore estimated at 1.0 ns ($\gamma_1 = 10^9 s^{-1}$) from the results of Figure V-15. A precise determination of other radiative and inter-sublevel relaxation rates from the available information is not possible. A modeling of the non-resonant experiments presented in this section would involve too many unknown parameters to yield accurate results. To obtain good values for all the radiative rates and all the inter-sublevel relaxation rates, resonant excitation experiments would be required. For example, creating the carriers resonantly in the n=2 level would greatly restrain the number of parameters involved and would allow a good determination of the n=2 to n=1 relaxation rate along with the n=2 radiative relaxation rate. Such resonant experiments proved more challenging with sample IR in view of the low luminescence signal obtained for such experimental conditions. This aspect is left for future investigations.

Every measurement performed so far on sample IR reveals a fast inter-sublevel dynamics that is not restricted due to the discrete density of states. The inter-level relaxation can be supported mainly by three mechanisms: LA phonon emission, LO phonon emission and Auger scattering. Once again, the reader is referred to Figure IV-6 for an illustration of these processes.

Relaxation rates between a set of two discrete levels have been considered from a theoretical point of view in the literature. Bockelmann *et al.* have studied a quantum dot made of an $In_{0.47}Ga_{0.53}As$/InP well in the z-direction and infinite barriers in the x-y plane. In a first calculation, only LA phonons are considered and the contribution of LO and Auger scattering is neglected[69]. The results of the calculation for a lattice temperature of 4 K show that a minimum scattering time of ~1 ns is achieved for an energy level separation of 1.0 meV. For higher energy separation, the scattering rate is quickly quenched and becomes negligible (scattering time > 10 ns) for an energy separation of 2 meV. Thus, fast inter-sublevel dynamics in sample IR cannot be explained by LA phonon emission.

Inoshita and Sakaki[82] have considered the case of LO phonon emission for a parabolic GaAs quantum dot. In their calculation, transitions involving one LO and one LA phonon are considered. The results for low temperatures show that relaxation rates of the order of ~10 ps are achieved if the energy level separation is equal to the energy of one LO phonon with a tolerance of 2 meV. In sample IR, phonons with an energy of 30 meV (InAs-like) and 36 meV (GaAs-like) are available. Thus, relaxation between conduction band states can be achieved via LO phonon emission since the energy separation of 28 meV closely matches the InAs-like phonon energy.

Auger scattering can also contribute significantly to the inter-sublevel relaxation. Using the same system as for the LA phonon relaxation calculation, Bockelmann *et al.* have considered the interaction of a carrier trapped in the first excited state of a quantum dot with a surrounding 2D electron-hole plasma[81]. This situation is of relevance in the case of self-assembled dots for which the carriers trapped in a dot can interact with the carriers trapped in the wetting layer. At low temperatures, the calculation predicts relaxation times lower than 10 ps for an energy level separation of 40 meV with a plasma density of the order of 2×10^{10} cm^{-2}. Given the densities estimated in Table V-7, Auger scattering may play a significant role in the inter-sublevel relaxation. Other types of Auger interactions involving energy transfer between an electron and a hole trapped in the same dot have been invoked to explain efficient relaxation[84]. In experiments, rise times of the QD emission for a self-assembled system subject to non-resonant excitation was reported[85] to shorten from 90 ps to 30 ps around a transition excitation intensity of 10 W/cm^2. This effect was attributed to Auger scattering at higher excitation intensities.

In this section, TRPL experiments using non-resonant excitation were performed on sample IR. The results have shown faster decay rates for higher levels and lower excitation intensities. Both observations could be explained in terms of state-filling effects in an ensemble of quantum dots with excited state emission.

V.4 Magneto-Photoluminescence

The zero-dimensional nature of the shell structure in sample VI was demonstrated by direct probing of the discrete density of states as a function of temperature. Similar conclusions were reached by monitoring the evolution of the inhomogeneously broadened emission line as a function of magnetic field up to 40 T[86] for quantum dots with a single bound state.

In the case of sample IR, both theory and experiment are consistent with the presence of a degenerate electronic shell structure with excited states. Much work has been devoted to understand unusual behavior of excitons in strong magnetic fields[43,44,87,88,89,90]. More specifically, for self-assembled dots the degeneracy of the energy shells is partially lifted by the application of a magnetic field perpendicular to the plane of the islands[35], and this is expected to have an effect on the emission spectrum. The magnetic field dependent single particle energy spectrum of a lens-shape quantum dot was obtained in chapter two (equation II-31), and Figure V-16 presents the results obtained using the oscillator frequency ω calculated in section V-1[91]. The energy axis reflects the in-plane degrees of freedom. At zero magnetic field, carriers carrying the same number of quanta have degenerate energies and can be labeled according to a single level index as introduced earlier in section V-1. As the magnetic field is increased, the energy of the right handed and left handed quanta are progressively split so that one now needs to specify the number

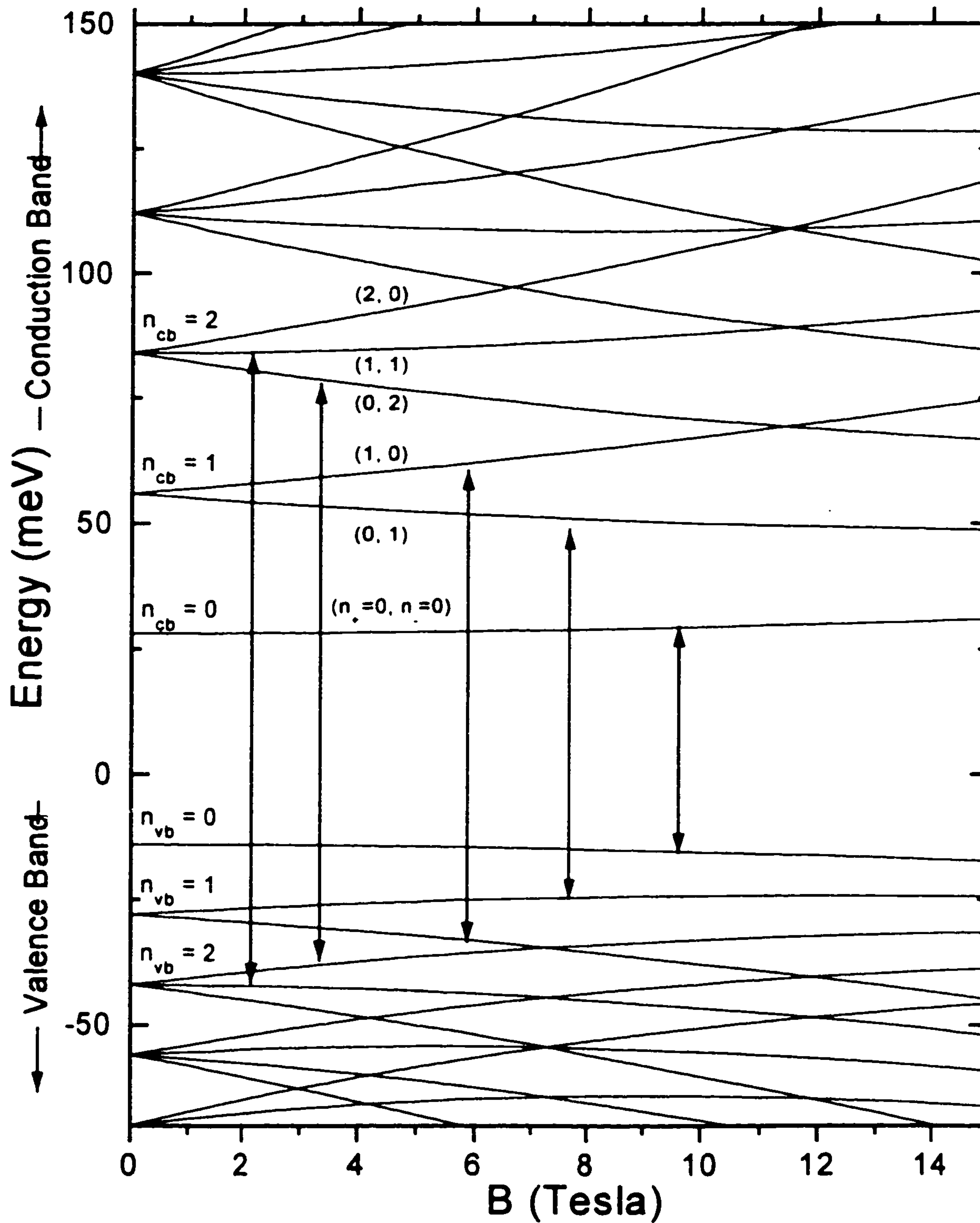

Figure V-16

Evolution of the bound state energies as a function of magnetic field. At 0 Tesla, the states are labeled according to the state index n, while for higher magnetic fields it is more convenient to use the circular polarizarion index n_+ and n_- as shown in parenthesis for the conduction band states. The magnetic field partially lifts the degeneracy of the shell structure, but for specific values of the magnetic field, a partial restoration of the shell degeneracy can be observed. The lowest allowed optical transitions are indicated by arrows.

of quanta in each polarization. The most striking feature of the diagram is that for specific values of the magnetic field, a partial reconstruction of the shell degeneracy can be observed. This effect occurs around values of 11.5 T for the conduction band and 7.2 T for the valence band. This behavior of the shell structure should be reflected in the recombination spectrum, and the arrows indicate the five optically allowed transitions with the lowest energy. To obtain the evolution of the emission lines as a function of magnetic field, equation V-14 can be written in terms of circularly polarized oscillators:

$$E^{rad} = E_{gap} + E_{strain} + E_z^{cb} + E_z^{vb} + n_+\hbar\left(\Omega_+^{cb} + \Omega_+^{vb}\right) + n_-\hbar\left(\Omega_-^{cb} + \Omega_-^{vb}\right) \qquad \text{V-25}$$

where $\Omega_{+,-}^{cb,vb}$ is defined in equation II-30 using the appropriate effective masses and oscillator frequency given in section V-1. Figure V-17 shows the evolution of the emission line for the five lowest radiative transitions as a function of magnetic field. At zero field, only three transitions are observed because of the degeneracy of the lower bound states. For intermediate fields (~4-5 T) there are now five distinct emission peaks coming from five distinct energy levels each having a degeneracy of two due to spin. For strong fields around 10 T, the third and fourth emission line merge into a single emission line so that only four emission lines can be observed. This peak reconstruction effect is typical of emission originating from quantum dots with excited state. Ground state emission originating from different families of quantum dots or ML fluctuations of a quantum well could not produce such a reconstruction since the weaker diamagnetic interaction would produce a uniform shift of the emission towards higher energies for all lines. Stronger Zeeman interaction producing shifts in opposite directions for the emission lines can be observed if states with opposite circular polarization are present.

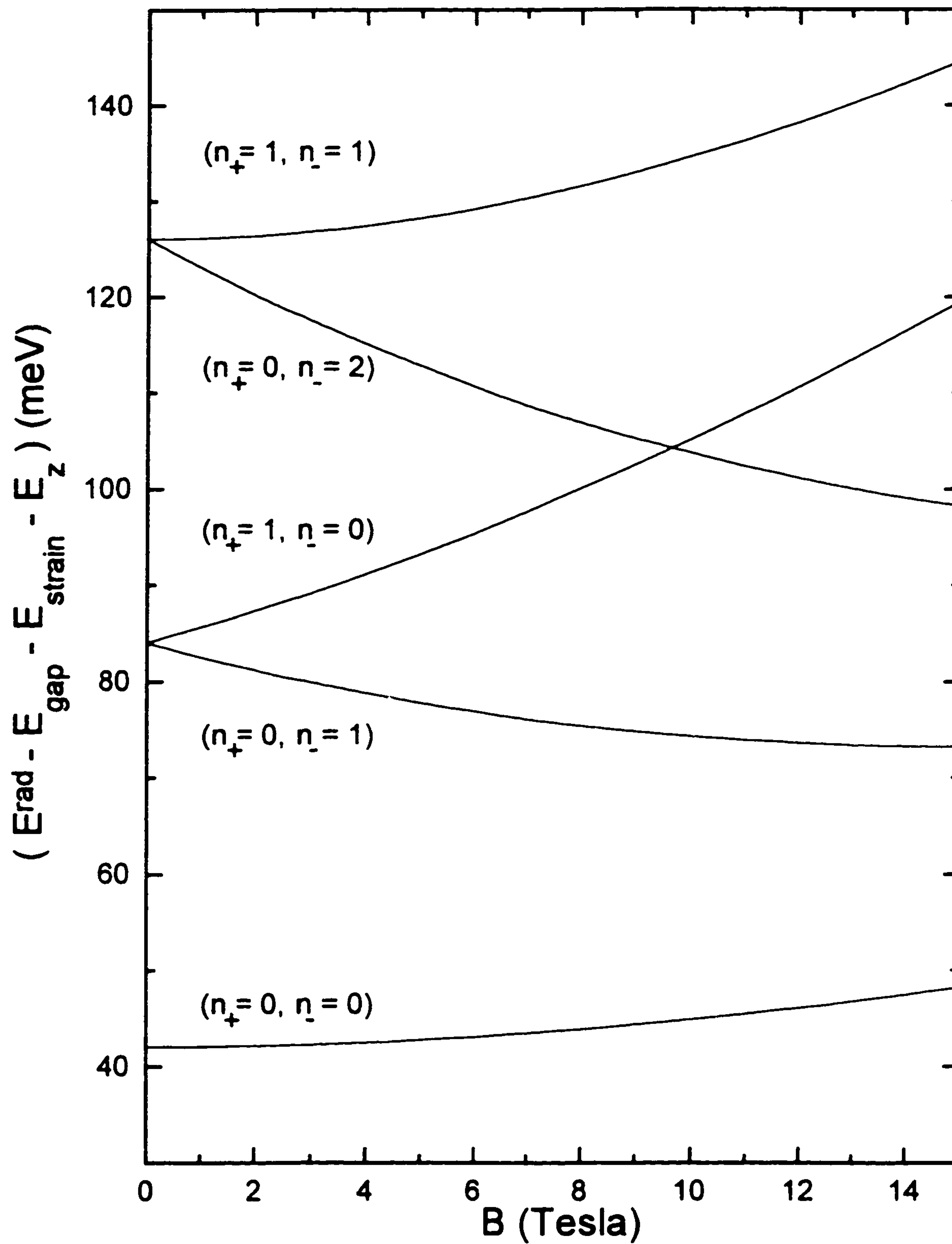

Figure V-17

Evolution of the energy of the lowest radiative transitions as a function of the magnetic field. Those transitions were indicated by arrows in Figure V-16.

Magneto-Photoluminescence spectra of sample IR are obtained using the set-up of Figure V-18. The sample is placed in an 200 series Oxford Instrument dilution refrigerator in between superconducting coil magnets and kept at a temperature of approximately 4 K. The YAG pumped pulsed dye laser is used as an excitation source with a photon energy of 1.968 eV; the laser beam is reflected on the surface of a diode edge filter and coupled to a multimode fiber with a core radius of 100 μm. The other end of the fiber is placed directly above the surface of the sample (~ 0.1 mm distance) in the cryostat. The sample emission is collected through the same fiber, and dispersed by the 0.64m spectrometer. The photons were detected with the cooled Ge detector using a standard synchronous detection scheme. The fiber transmission was measured independently at room temperature in the detection range and the result was used to correct the sample emission spectra obtained.

The resulting spectra, for magnetic fields ranging from 0 to 13 T, are shown in Figure V-19. At zero field, the three lowest transitions are clearly observed with an intensity ratio typical of CW excitation with an average of approximately 8 excitons per dot (comparing with the results of figure V-5 and table V-4). The fact that the spectrum is not typical of pulsed excitation is attributed to the dispersion of the fiber which significantly broaden the laser pulses. Also, because it is not possible to access the sample end of the fiber that sits near the surface of the sample during the experiment it is difficult to evaluate the excitation power density.

For low magnetic fields, the ground state, first excited state and second excited state are populated with an estimate of 2,4 and 2 excitons respectively. This distribution can be separated into 2 excitons each for the following states $|n_+,n_-\rangle = |0,0\rangle,|0,1\rangle,|1,0\rangle,|0,2\rangle$. As

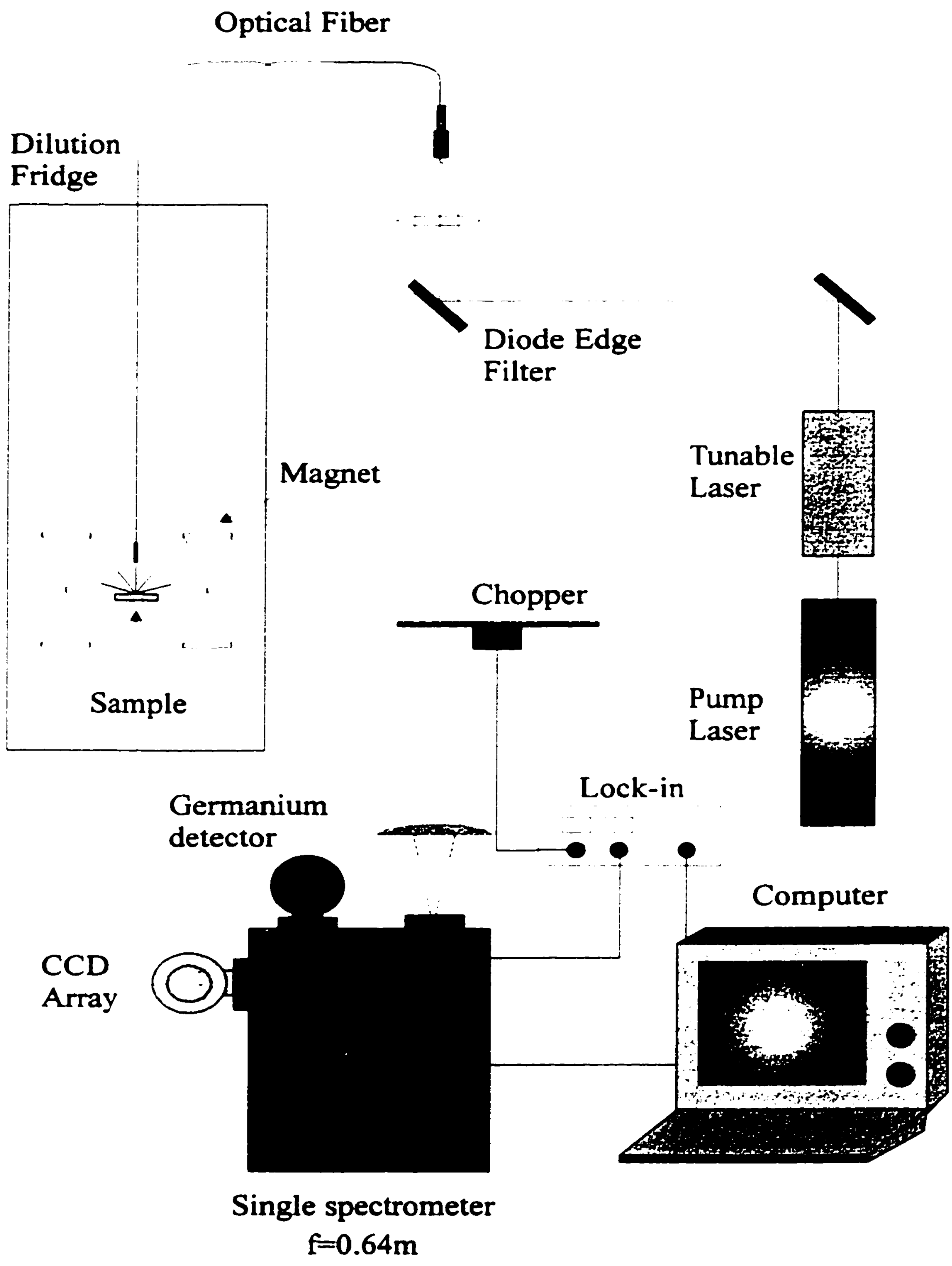

Figure V-18

Set-up used to obtain magneto-PL measurements of sample IR.

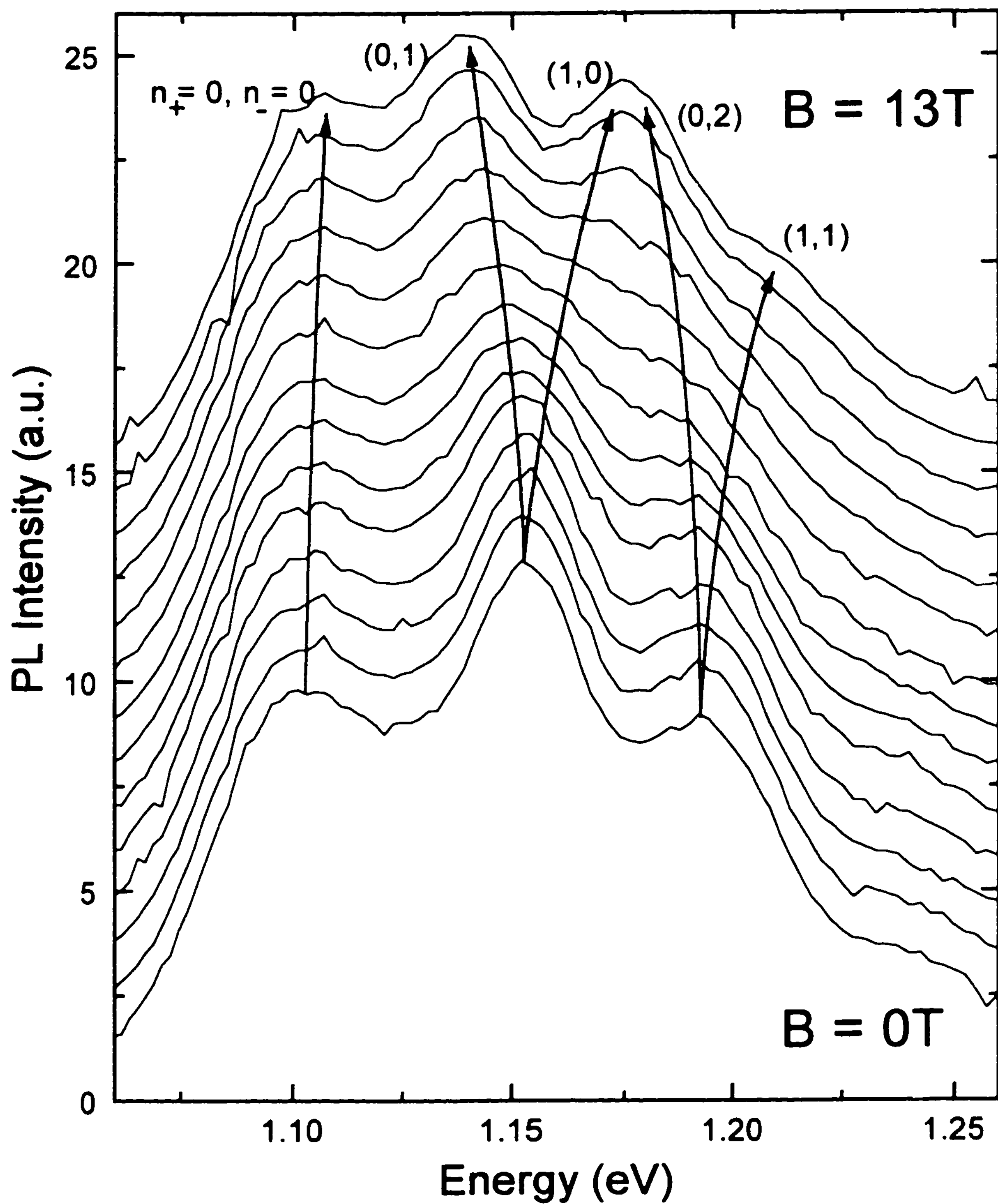

Figure V-19

Low temperature (4 K) emission spectrum of sample IR for magnetic fields ranging from 0 to 13 T. The arrows tentatively indicate the evolution of the transition energies for the five lowest energy states.

the magnetic field is increased, the ground state line shows little variation in intensity or emission energy, except perhaps for a weak shift towards higher energies. On the other hand, the higher energy emission lines progressively rearrange their emission energies as suggested by the arrows. As the field is increased, the $|0,1\rangle$ and $|1,0\rangle$ transition lines are split and "move" in opposite directions, while the $|0,2\rangle$ transition is displaced almost parallel to the $|0,1\rangle$ transition. At intermediate fields of 9 T, these three inhomogeneously broadened emission lines are equally spaced within ~17 meV of each other so that none of them can be resolved and their emission merges in a very broad distribution. For yet higher fields of ~12 T, the $|1,0\rangle$ and $|0,2\rangle$ transition energies become equal and well resolved emission peaks are recovered in a more compact energy range than for zero field. Also, one can see that the first excited state has lost amplitude with respect to the other two emission lines indicating a redistribution of the excitonic population.

The observation of this peak reconstruction at 13 T over a more compact energy range is consistent with the predictions of Figure V-17 if one considers that only the four lowest lines will contribute to the emission spectrum for a population of 8 excitons. This reconstruction was however expected for lower fields (~9.5 T), but this discrepancy can easily be explained by the uncertainty in the valence band modeling, which did not take into account anisotropic effective masses.

V.5 Concluding remarks

In the first section of this chapter, the model of chapter two for lens shaped dots was slightly improved by considering finite potential walls. This improved calculation method was applied to the case of a typical dot of sample IR. The transition energy spacing thus obtained were found to be consistent with the experimental results.

Next, after presenting the PL spectra for different excitation power densities, several explanations were considered to explain the observation: monolayer fluctuations of a quantum well layer, families of islands (segregated inhomogeneous broadening), quantum dots with excited state emission in the phonon bottleneck or state-filling regime. The peak reconstruction observed for the PL spectrum of sample IR under strong magnetic fields unambiguously proved that the higher energy emission lines originate from transitions between quantum dot excited states. The same conclusion was reached by careful analysis of various measurements: excitation intensity dependence, temperature dependence and TEM micrographs.

Finally, the time-resolved measurements, showing a decay cascade from higher levels to lower levels, clearly showed that the dynamics is primarily dominated by state-filling effects. This is confirmed by a careful analysis of the intensity dependence of the emission spectrum under different excitation conditions.

VI Conclusion

In this work, self-assembled semiconductor islands produced by Stranski-Krastanow growth were modeled and characterized. Two different material systems were studied: 1- $Al_{0.45}In_{0.55}As$ islands imbedded in $Al_{0.35}Ga_{0.65}As$ emitting in the visible (sample VI) and 2- $In_{0.5}Ga_{0.5}As$ islands imbedded in GaAs emitting in the infra-red (sample IR). From a cross-section TEM micrograph of sample VI, the self-assembled layer was seen to be composed of a series of "thick" (~5-6 nm) lens-shaped islands connected by a thin (~1.5-2 nm) quantum well layer. The plan view TEM image obtained for both samples revealed a plane of more or less randomly distributed islands, with a base diameter varying by about 10% from island to island. The mean diameter obtained for sample VI was 18 nm, while a value of 36 nm was found for sample IR.

The structural properties of these islands were used to model the electronic bound states in the InGaAs/GaAs system in terms of harmonic in-plane potential combined with a square well potential in the z-direction. The $\Delta n_{x,y}=0$ selection rule for optical transitions was derived from this model, yielding and energy spacing of 42 meV between the transitions, in good agreement with the experimental result of 45±5 meV. One should note that other research groups have obtained small pyramidal shaped islands with a square base (InAs)[92] or with an hexagonal base (InP/InGaP)[93]. In such systems, the selection rules obtained for the optical transitions are different than for the radially symmetric dots, and higher energy lines observed in the emission spectrum have been attributed to

recombinations between ground state electrons and excited state holes. At this point it seems possible that the shape of the islands indeed depend on the composition and the amount of material deposited. More work involving systematic structural characterization is needed to clarify this issue of the different shapes one can obtain in self-assembled systems.

Also, It should be emphasized that the presence of at least five "zero-dimensional" bound states was predicted for sample IR, and experimental results have confirmed this prediction. This is in contrast with the results of sample VI for which no evidence of excited state emission could be observed. This difference can be attributed to the information provided by the TEM, which clearly demonstrated that the islands of sample VI were much smaller than those of sample IR. This structural difference implies much bigger inter-sublevel spacings in sample VI, to the point that even the first excited state is an unbound state.

Following the investigation on the structural properties of the samples, the bound states were probed by means of optical experiments. Our attention was focused on establishing the dimensionality of the island's density of states. To this effect, the emission linewidth of "individual" dots was monitored as a function of temperature and the results conclusively showed that the emission lines did not broaden as a function of temperature, thus providing strong evidence to the zero-dimensional nature of the bound states in the islands. Similar results were obtained independently by another group using cathodoluminescence measurements on InAs/GaAs square pyramidal dots[94], with the same conclusion being reached. The temporal behavior of carriers trapped in individual dots was

also shown to be independent of temperature, providing further evidence of the zero-dimensionality of the bound states. Finally, the zero-dimensional properties of the islands was confirmed through magneto-photoluminescence measurements done on sample IR. Carriers trapped in the excited states with non-zero angular momentum states have shown strong interaction with the magnetic field, as evidenced in the spectrum from the peak reconstruction occurring around 12T. This effect was related to the Zeeman splitting of the in-plane parabolic states, typical to quantum dots but not to structures of other dimensionalities. A similar experiment was performed concomitantly on strained-induced GaAs dots with radial symmetry, and the results have shown the peak splitting typical of non-zero angular momentum states[95]. It would be interesting to compare these results with the case of pyramidal shaped quantum dots, since the different in-plane symmetry should yield different level degeneracy and therefore different magneto-PL results. To the author's knowledge, no such experiments or calculations are reported in the literature at this time. Such magneto-PL experiments coupled with appropriate calculations should in principle provide an additional way of characterizing the shape of the islands.

With the dimensionality of the bound states well established, the emphasis of the study was turned towards carrier dynamics in self-assembled dots. Because of the discrete nature of the bound states in quantum dots, early calculations based on phonon-mediated relaxation predicted a very slow relaxation rate from the higher energy states to the lower energy states (ref. 50). It is important to mention that for both samples the observed emission intensity of the quantum dot ground state was found to be dominant at low excitation intensities, thus indicating efficient carrier relaxation, in contradiction with

theoretical predictions. Nevertheless, the resonant excitation experiments of chapter IV have undoubtedly shown that phonons do play an important role in the dynamics of carriers trapped in self-assembled dots. A strong enhancement of the PL emission at energies corresponding to one LO phonon mode below the excitation energy was observed. In another investigation where pyramidal dot shapes were assumed, other authors have assigned similar phonon resonances in self-assembled dots to Raman scattering and resonant relaxation from higher excited states[96]. However, this conclusion was reached without any time-dependant information. In our case the width of the resonances and the long lifetimes observed are inconsistent with a Raman effect. Also, a faster decay time was observed for resonant excitation, compared with the non-resonant excitation case, and this remains unexplained at the moment. However, abnormally high background emission was observed in temperature and power-dependent micro-PL experiments (see fig. IV-2 and IV-8). Such abnormal background was also observed in micro-PLE[97,98] experiments and at least in one case (ref. 97) the authors pointed out this phenomenon that they could not explain. These unexplained results could be related to the abnormal dynamics observed.

The issue of restricted phonon relaxation was also investigated by means of time-resolved measurements on sample IR. It was found that the decay time of the transition monitored shortens as the level index probed is increased and as the excitation intensity is lowered. This effect was interpreted in terms of state-filling effects, where the relaxation time of an electron-hole pair towards the next lowest level is empty. However, this inter-sublevel relaxation time becomes much longer than the radiative lifetime when the lower

level is filled with carriers. Furthermore, the relative weight of the transition lines observed in power dependent PL experiments showed satisfactory agreement with predictions obtained assuming the state-filling limit for the carrier dynamics. Thus, once again the experimental results are in contradiction with models based on phonon-assisted dynamics. For LA phonon scattering, calculations show that the transfer rate between levels becomes very small when the energy separation exceeds 2meV (ref. 69). On the other hand, sub-nanosecond scattering rates can be obtained by LO phonon emission only if the inter-sublevel spacing is within 10% (~3 meV) of the phonon energy. One can compare these numbers with other experimental results where state-filling dynamics was obtained for strain-induced dots with level separations of 15 meV (ref. 77), and evidence of the phonon-bottleneck was reported for dots with level separation of 75 meV[99]. Certainly in the first case, the level separation is much higher than the acceptable range for efficient acoustic phonon scattering, while too small to match LO phonon energies of any kind. Alternatively, Auger scattering was proposed to explain the efficient relaxation, but in view of the low excitation intensities generally used for the PL experiments this explanation remains doubtful despite recent experimental evidence (ref. 85).

Our time-resolved experiments have also enabled us to establish that the radiative lifetime of electron-hole pairs trapped in the ground state of sample IR is 1.0 ns or shorter. Also, from the low intensity measurements an upper limit of 310 ps was obtained for the scattering time between the n=3 and n=2 level. The precise determination of all the inter-sublevel and all the radiative relaxation rates would have required resonant excitation experiments to be performed. This was not achieved in this work and remains an

interesting challenge for the future.

In Summary, the optical properties of self-assembled quantum dots were investigated in this work. The results of structural characterization (TEM pictures) were used to model the properties of the electronic states of the islands. Optical experiments were performed and successfully compared with theoretical results in a number of cases: temperature independent linewidths, temperature independent lifetimes, excited emission energy spacing and Zeeman effect.

A number of the properties observed remain either unexplained or uninvestigated. For example, the physics underlying the finite linewidth (i.e. not uncertainty limited) of single quantum dot emission lines is not well understood at the present time. Also, the origin of phonon resonances observed in the PL spectra under resonant excitation and the presence of a broad background in some experiments could not be satisfactorily explained. As a last example it should be montioned that a regular in-plane arrangements of the islands is necessary for many applications, as well as a better control of the structural fluctuations in the dot population. These problems, and many others, leave many challenges for further investigations of self-assembled quantum dots.

References

[1] L. Esaki and R. Tsu, IBM J Res. Dev. **14**, 61 (1970).

[2] L. L. Chang, L. Esaki, W. E. Howard, R. Ludeke and G. Schul, J. Vac. Sci. Technol., vol. 10, No. 5, 655 (1973).

[3] For InGaAs/GaAs see Jpn. J. Appl. Phys. **35**, L535 (1996); for AlSb/GaSb and AlSb/InGaSb see Appl. Phys. Lett. **64**, 2127 (1994).

[4] See for example G. H. B. Thompson in "Physics of Semiconductor Laser Devices", chap. 3 p. 132, John Wiley and Sons, New York (1980).

[5] For example, compare the characteristics quoted by G. H. B. Thompson in "Physics of Semiconductor Laser Devices", chap. 3 p. 133 and chap. 3 p. 157, John Wiley and Sons, New York (1980).

[6] Y. Miyamoto, Y. Miyake, M. Asada and Y. Suematsu, IEEE Journal Quant. electron., vol. 25, No 9, pp 2001-2006.

[7] Y. Arakawa and H. Sakaki, Appl. Phys. Lett. **40**, 939 (1982).

[8] M. Kohl, D. Heitman, W. W. Rühle, P. Grambow and K. Ploog, Phys. Rev. B **41**, 12338 (1990); J. N. Patillon, C. Jay, M. Iost, R. Gamonal, J. P. André, B. Soucail, C. Delalande and M. Voos, Superlatt. Microstruct. Vol 8, No 3, p335 (1990); M. Notomi, M. Naganuma, T. Nishida, T. Tamamura, H. Iwamura, S. Nojima and M. Okamoto, Appl. Phys. Lett **58**, 720 (1990).

[9] H. Leier, A. Forchel, B. E. Maile, G. Mayer, J. Hommel, G. Weinmann and W. Schlapp, Appl. Phys. Lett. **56**, 48 (1990).

[10] H. Akiyama, S. Koshiba, T. Someya, K. Wada, H. Noge, Y. Nakamura, T Inoshita, A. Shimizu and H. Sakaki, Phys. Rev. Lett. **72**, 924 (1994).

[11] A. R. Goni, L. N. Pfeiffer, K. W. West, A Pinczuk, H. U. Baranger and H. L. Stormer, Appl. Phys. Lett. **61**, 1956 (1992).

[12] T. J. Thornton, M. Pepper, H. Ahmed, D. Andrews and G. J. Davies, Phys. Rev. Lett. **56**, 1198 (1986); S. H. Wang, D. C. Tsui and M. Shayegan, Phys. Rev. B **49**, 16441 (1994).

[13] M. A. Reed, R. T. Bate, K. Bradshaw, W. M. Duncan, W. R. Frensley, J. W. Lee and H. D. Shih, J. Vac. Sci. Technol. B 4, 358 (1986).

[14] U. Bockelmann, Ph. Roussignol, A. Filoramo, W. Heller, G. Abstreiter, K. Brunner, G. Böhm and G. Weinmann, Phys. Rev. Lett. **76**, 3622 (1996).

[15] O. Klein, C. de C. Chamon, D. Tang, D. M. Abush-Magder, U. Meirav, X.-G. Wen, M. A. Kastner and S. J. Wind, Phys. Rev. Lett. **74**, 785 (1995); R. P. Taylor, A. S. Sachrajda, P. Zawadzki, P. T. Coleridge and J. A. Adams, Phys. Rev. Lett. **69**, 1989 (1992).

[16] V. Klimov, P. Haring Bolivar and H. Kurz, phys. Rev. B **53**, 1463 (1996).

[17] R. Leonelli, C. A. Tran, J. L. Brebner, J. T. Graham, R. Tabti, R. A. Masut and S. Charbonneau, Phys. Rev. B **48**, 11135 (1993).

[18] M. Volmer and A Weber, *Z. Phys. Chem.* **119**, 277 (1926).

[19] I. N. Stranski and Von. L. Krastanow, *Akad. Wiss. Lit. Mainz Math. Naturwiss. Kl.* **146**, 797 (1939).

[20] F.C. Frank and J. H. Van Der Merwe, *Proc. R. Soc. London Ser. A* **198**, 205 (1949).

[21] For more detailed discussion see D. E. Jesson, K. M. Chen, S. J. Pennycook, T. Thundat and R. J. Warmack, proceedings of the 23rd ICPS conference, vol. II, pp. 1253-1260, World Scientific Publishing Co., Singapore, (1996).

[22] S. Chang, T. Chang and S. Lee, J. appl. Phys. **73**, 4916 (1993).

[23] D. J. Eaglesham and M. Cerullo, Phys. Rev. Lett. **64**, 1943 (1990).

[24] P. Chen, Q. Xie, A. Madhukar, Li Chen and A. Khonar, J. Vac. Sci. Technol. B **12**(4), 2568 (1994).

[25] D. Leonard, S. Fafard, K. Pond, Y. H. Zhang, J. L. Merz and P. M. Petroff, J. Vac. Sci. technol. B **12**(4), 2516 (1994).

[26] J. M. Moison, F. Houzay, F. Barthe, L. Leprince, E. André and O. Vatel, Appl. Phys. Lett. **64**, 196 (1994).

[27] R. Leon, P. M. Petroff, D. Leonard and S. Fafard, Science vol. 267, 1966 (1995).

[28] D. Leonard, S. Fafard, K. Pond, Y. H. Zhang, J. L. Merz and P. M. Petroff, J.

Vac. Sci. technol. B **12**(4), 2516 (1994).

[29] D. Leonard, K. Pond, and P. M. Petroff, Phys. Rev. B **50**, 11687 (1994).

[30] G. Bastard in "Wave mechanics applied to semiconductor heterostructures", chap. III p.63, Halsted Press (John Wiley and Sons) New York (1988).

[31] G. Bastard in "Wave mechanics applied to semiconductor heterostructures", chap. II p.42, Halsted Press (John Wiley and Sons) New York (1988).

[32] For a definition see "Mécanique Quatique", C.Cohen-Tannoudji, B. Diu, F. Laloë Vol. 2, p. 1468, Hermann, Paris (1973).

[33] S. J. Lee, N. H. Shin, J. J. Ko, M. J. Park and R. Kümmel, Semicond. Sci. Technol. **7**, 1072 (1992).

[34] L. Esaki in a book published by P. Y. Yu and M. Cardona, *Fundamentals of semiconductors*, p. 563, Spinger-Verlag, Berlin 1996.

[35] A. Wojs, P. Hawrylak, S. Fafard and L. Jacak, Phys. Rev.B **54**, 5604 (1996).

[36] E. Kapon, D. M. Hwang and R. Bhat, Phys. Rev. Lett. **63**, 430 (1989).

[37] C.Cohen-Tannoudji, B. Diu, F. Laloë in "Mécanique Quatique", Vol. 1, chap. 5, p. 479, Hermann, Paris (1973).

[38] H. Matsumoto, K. Saito, M. Hasuo, S. Kono and N. Nagasawa, Solid State Commun. **97**, No 2, 125 (1996).

[39] V. Fock, Z. Phys. **47**, 446 (1928).

[40] C. G. Darwin, Proc. Cambridge Philos. Soc. **27**, 86 (1930).

[41] R.B. Dingle, Proc. Roy. Soc. London A **211**, 500 (1952).

[42] P. A. maksym and T. Chakraborty, Phys. Rev. Lett. **65**, 108 (1990).

[43] A. Wojs and P. Hawrylak, Phys. Rev. B **51**, 10880 (1995).

[44] P. Hawrylak, A. Wojs and J. A. Brum, Phys. Rev. B **54**, 11397 (1996).

[45] Y. Arakawa, H. Sakaki, M. Nishioka, H. Okamoto and N. Miura, Jpn. J. Appl. Phys. **22**, L-804 (1983).

[46] N. Peyghambarian, S. W. Koch and A. Mysyrowicz in "Introduction to

Semiconductor Optics", p. 112 for Bulk and p. 214 for Quantum Well, Prentice-Hall, New-Jersey (1993).

[47] J.J. Sakurai, "Modern Quantum Mechanics", revised version, chap. 5, p. 334, Addison-Wesley Publishing company, (1994).

[48] G. Bastard in "Wave mechanics applied to semiconductor heterostructures", chap. VII p. 239, Halsted Press (John Wiley and Sons) New York (1988).

[49] G. Bastard in "Wave mechanics applied to semiconductor heterostructures", chap. VII p. 242, Halsted Press (John Wiley and Sons) New York (1988).

[50] H. Benisty, C. M. Sotomayor-Torrès and C. Weisbuch, Phys. Rev. B **44**, 10945 (1991).

[51] L. Schultheis, A. Honold, J. Kuhl, K. Kohler and C. W. Tu, Phys. Rev. B **34**, 9027 (1986).

[52] V. Srinivas, J. Hryniewicz, Y. J. Chen and C. E. C. Wood, Phys. Rev. B **46**, 10193 (1992).

[53] For a discussion, see G. Bastard in "Wave mechanics applied to semiconductor heterostructures", chap. III p. 73, Halsted Press (John Wiley and sons) New York (1988).

[54] S. Fafard, E. Fortin and A. P. Roth, Can. J. Phys. **69**, 346 (1991).

[55] See P. W. M. Blom, P. J. van Hall, C. Smit, J. P. Cuypers and J. H. Wolter, Phys. Rev. Lett. **71**, 3878 (1993), and references therein.

[56] S. Fafard, R. Leon, D. Leonard, J.L. Merz and P.M. Petroff, Phys. Rev. B **50**, 8086 (1994).

[57] S. Charbonneau, L.B. Allard, J. F. Young, G. Dyck and B. J. Kyle, Rev. Sci. Instrum. **63** (11) 5315 (1992).

[58] For a more exhaustive description see S. Charbonneau, Ph. D. dissertation, Simon Fraser University (1989).

[59] Jagdeep Shah, IEEE Journal of quant. electron. vol. 24, No 2, 276 (1988).

[60] S. Fafard, R. Leon, D. Leonard, J.L. Merz and P.M. Petroff, Phys. Rev. B **50**, 8086 (1994).

[61] S. Fafard, S. Raymond, G. Wang, R. Leon, D. Leonard, S. Charbonneau, J. L.

Merz, P.M. Petroff and J.E. Bowers, Surface Science 361/362, 778-782 (1996).

[62] J. Christen and D. Bimberg, Phys. Rev. B **42**, 7213 (1990).

[63] T. Takagahara, Phys. Rev. B **47**, 16639 (1993).

[64] S. Fafard, R. Leon, D. Leonard, J.L. Merz and P.M. Petroff, Phys. Rev. B **52**, 5752 (1995).

[65] O. Madelung in "Semiconductor grooup IV elements and III-V compounds" edited by O. Madelung, Springer-Verlag, Berlin, 1991.

[66] D. S. Jiang, X. Q. Zhou, M. Oestreich, W. W. Rhule, R. Notzel and K. Ploog, Phys. Rev. B **49**, 10786 (1994).

[67] A 30% reflection at the sample surface and a 0.5% absorption in the wetting layer were included in the calculation of $\Phi(I_{exc})$

[68] D. S. Citrin, Phys. Rev. Lett. **69**, 3393 (1992).

[69] U. Bockelmann and G. Bastard, Phys, Rev. B **42**, 8947 (1990).

[70] R. Eccleston, R. Strobel, W. W. Rhule, J. Khul, B. F. Feuerbacher and K. Ploog, Phys. Rev. B **44**, 1395 (1991).

[71] T. C. Damen, J. Shah, D. Y. Oberli, D. S. Chemla, J. E. Cunningham and J. M. Kuo, Phys. Rev. B **42**, 7434 (1990).

[72] Manfred Helm, Phys. Rev. B **42**, 1601 (1993).

[73] M. Grundmann, O. Stier and D. Bimberg, Phys. Rev. B, **52**, 1969 (1995).

[74] R. People and S.K. Sputz, Phys. Rev. B **41**, 8431 (1990).

[75] S. H. Pan, H. Shen, Z. Hang, F. H. Pollak, W. Zhuang, Q Xu, A. P. Roth, R. A. Masut, C. Lacelle and D. Morris, Phys. Rev. B **38**, 3375 (1988).

[76] M. V. Marquezini, M. J. S. P. Brasil, J. A. Brum, P. Poole, S. Charbonneau and M. C. Tamargo, Surface Science **361/362**, 810 (1996).

[77] H. Lipsanen, M. Sopanen and J. Ahopelto, Phys. Rev. B **51**, 13868 (1995).

[78] M. Colocci, Superlatt. Microstruct. vol. **22**, No. 1, p.81 (1997).

[79] S. Adachi, J. Appl. Phys. **66** (12), 6030 (1989).

[80] D. Gammon, E. S. Snow and D. S. Katzer, proceedings of the EP2DS-XI conference to be published in Surface Science.

[81] U. Bockelmann and T. Egeler, Phys. Rev. B **46**, 15574 (1992).

[82] T. Inoshita and H. Sakaki, Phys. Rev. B, **46**, 7260 (1992).

[83] For a good discussion of probability distributions see P. R. Bevington and D. K. Robinson in "Data Reduction and Error Analysis for the Physical Sciences", second edition, chap. 2, McGraw-Hill Inc. (1992).

[84] A. L. Efros, V.A. Kharchenko and M. Rosen, solid state commun. **93**, 281 (1995).

[85] B. Ohnesorge, M. Albrecht, J. Oshinowo and A. Forchel, Phys. Rev. B **54**, 11532 (1996).

[86] P. D. Wang, J.L. Merz, S. Fafard, R. Leon, D. Leonard, G. Medeiros-Ribeiro, M Oestreich, P. M. Petroff, K. Uchida, N. Miura, H. Akiyama and H. Sakaki, Phys. Rev. B **53**, 11532 (1996).

[87] A. Imamoglu and Y. Yamamoto, Phys. Rev. Lett. **72**, 210 (1994).

[88] D. Paquet, T. M. Rice and K. Ueda, Phys. Rev. B **32**, 5208 (1985).

[89] A. H. MacDonald and E. H. Rezayi, Phys. Rev. B **42**, 3224 (1990).

[90] Yu. A. Bychkov and E. I. Rashba, Phys. Rev. B **44**, 6212 (1991).

[91] This calculation follows the work of A. Wojs *et al.* in reference 35 where the contribution of the spin is neglected.

[92] S. Ruvimov, P. Werner, K. Scheerschmidt, U. Gosele, J. Heydenreich, U. Richter, N. N. Lendentsov, M. Grundmann, D. Bimberg, V. M. Ustinov, A. Yu Egorov, P. S. Kop'ev and Zh. I. Alferov, Phys. Rev. B **51**, 14766 (1995).

[93] L. Samuelson, S. Anand, N. Carlsson, P. Crastillo, K. Georgsson, D. Hessman, M.-E. Pistol, C. Pryor, W. Seifert, L. R. Wallenberg, A. Carlsson, J-O. Bovin, S. Nomura, Y. Aoyagi, T. Sugano, K. Ushida and N. Miura, proceedings of the 23rd international conference on the physics of semiconductors, pp. 1269-76 (1996).

[94] M. Grundmann, J. Christen, N. N. Lendentsov, J. Bohrer, D. Bimberg, S. S. Rustinov, P. Werner, U. Richter, U. Gosele, J. Heydenreich, V. M. Ustinov, A. Yu Egorov, A. E. Zhukov, P. S. Kop'ev and Zh. I. Alferov, phys. Rev. Lett. **74**, 4043 (1995).

[95] R. Rinaldi, P. V. Giugno, R. Cingonali, H. Lipsanen, M. Sopanen, J. Tulkki and J. Ahopelto, Phys. Rev. Lett. **77**, 342 (1996).

[96] R. Heitz, M. Grundmann, N. N. Lendentsov, L. Eckey, M. Veit, D. Bimberg, V. M. Ustinov, A. Yu Egorov, A. E. Zhukhov, P. S. Kop'ev and Zh. I. Alferov, Appl. Phys. Lett. **69**, 749 (1996).

[97] D. Hessman, P. Crastillo, M.-E. Pistol, C. Pryor and L. Samuelson, Appl. Phys. Lett. **69**, 749 (1996).

[98] M. Notomi, T. Furuta, H. Kamada, J. Temmyo and T. Tamamura, Phys. Rev. B **53**, 15743 (1996).

[99] K. H. Schmidt, G. Meideros-Ribeiro, M. Oestreich, P. M. Petroff and G. H. Dohler, Phys. Rev. B **54**, 11346 (1996).

IMAGE EVALUATION TEST TARGET (QA-3)

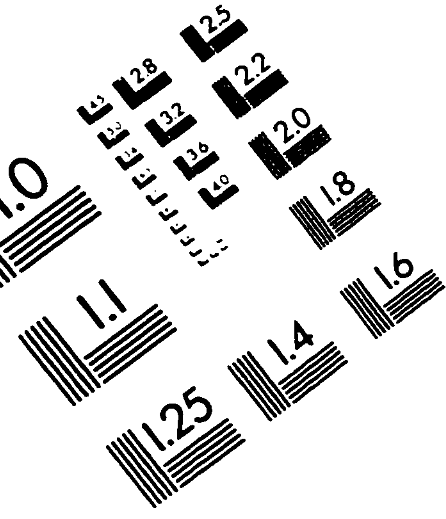

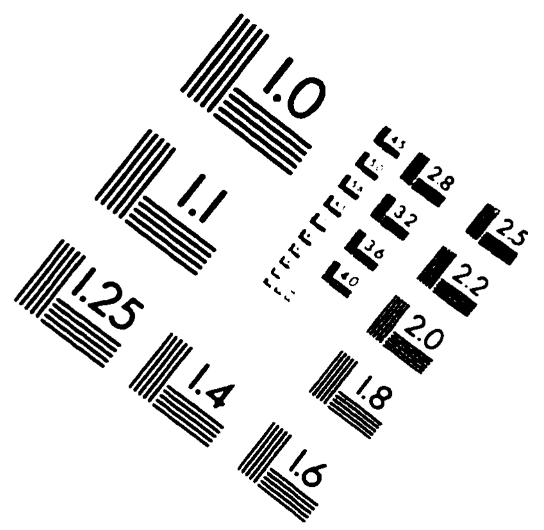

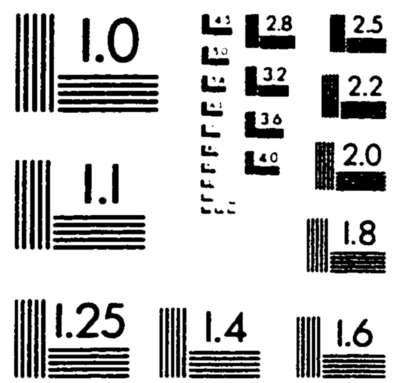

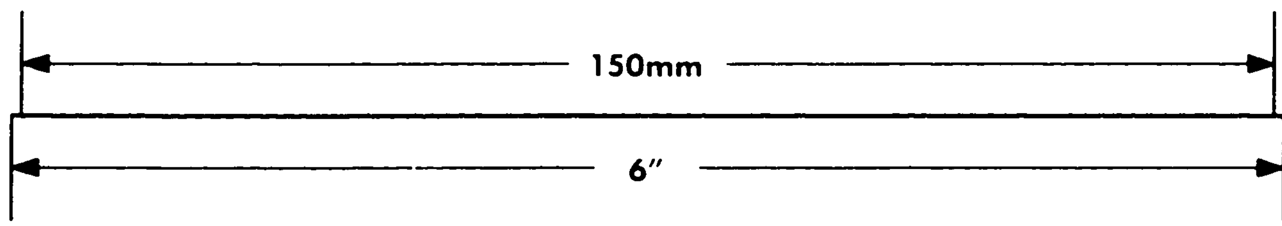

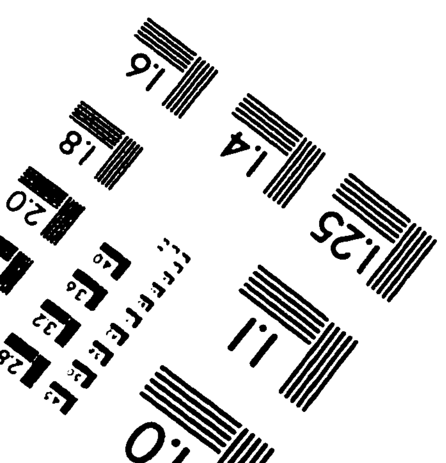

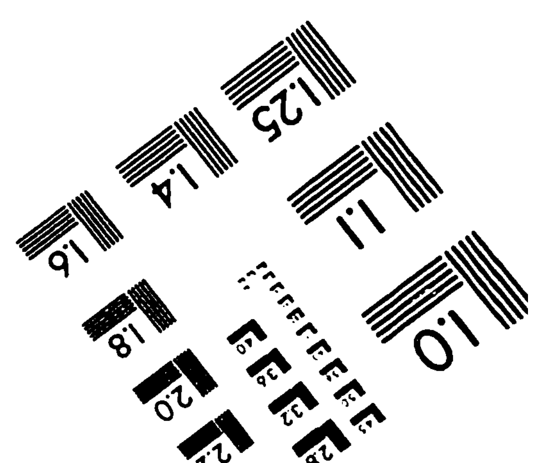

APPLIED IMAGE . Inc
1653 East Main Street
Rochester, NY 14609 USA
Phone: 716/482-0300
Fax: 716/288-5989

© 1993, Applied Image, Inc., All Rights Reserved